

SIZE-CONTROLLED MICROENCAPSULATION OF MESENCHYMAL STEM CELLS  
AND IMAGING AGENTS FOR SITE-SPECIFIC DELIVERY AND TRACKING

By  
Tsang Chung Charles Hu

A dissertation submitted to Johns Hopkins University in conformity with the  
requirements for the degree of Doctor of Philosophy

Baltimore, Maryland  
January 2017

© 2017 Tsang Chung Charles Hu  
All Rights Reserved

## Abstract

Tissue engineering seeks to develop biological substitutes and/or to foster the remodeling of tissue by manipulating cells and their extracellular environment. One of the many exciting subjects under tissue engineering involve the use of mesenchymal stem cells as paracrine factories to stimulate vascular repair via multiple chemical pathways. There has been extensive *in vitro* research on the efficacy of stem cell-assisted therapies. However, hypothesized outcomes become more nebulous when translating into the clinical setting due to the many factors associated with the much more complicated *in vivo* system. Among them are the difficulty in delivering the stem cells to the desired locations, the lack of visual information regarding the transplanted cells, and the inability to ensure that the transplanted cells are viable and can undertake the intended therapeutic mechanisms effectively.

In this thesis, we explore several strategies of microencapsulating stem cells while allowing the transplanted cells to be effectively visualized with conventional clinical scanners noninvasively. First, we developed a platform based on droplet microfluidics to produce small, highly uniform, imaging-visible microcapsules without cells. We studied the capsules' physical, chemical, and imaging properties as well as tissue compatibility in a chronic study involving gastric embolization in pigs. We then modified the platform to accommodate for the co-encapsulation of stem cells and imaging agents. Lastly, we explored a 3-dimensional bioprinting platform using a piezoelectrically actuated inkjet

printer head. The resulting microcapsules were able to achieve more rapid throughput compared to the microfluidic platform and was more amenable to the use of different carrying solutions, including biopolymers intended to enhance the efficacy of the encapsulated stem cells. The smaller microcapsules produced by our platforms also allow for more controlled delivery using conventional catheters when compared to the larger conventional cell encapsulation techniques.

**Readers:**

Hai-Quan Mao, Ph.D. (Advisor)

Dara L. Kraitchman, V.M.D., Ph.D., F.A.C.C. (Co-advisor)

Jeff Tza-Huei Wang, Ph.D. (Co-advisor) (Chair)

**Defense Committee:**

Clifford R. Weiss, M.D.

Peter Searson, Ph.D.

Kalina Hristova, Ph.D.

Warren Grayson, Ph.D.

## Acknowledgements

The process of obtaining the skills, knowledge, and research necessary to obtain a Ph.D. is a daunting undertaking that I would not have been able to achieve without the support of the many people I met along the journey. First and foremost I would like to thank Dr. Hai-Quan Mao, who provided me with many opportunities to explore potential projects, and who was always there to guide me in the inevitable times of failures and uncertainties. He encouraged me to look for alternate solutions to problems that were seemingly impossible to rectify, and inspired me to analyze results from the many perspectives that are not immediately apparent. Moreover, I would like to thank him for being one of the nicest, most supportive person I have ever met.

I am extremely indebted to my co-advisors for providing me with the tools and opportunities to expand my horizons beyond materials science. In particular, I thank Dr. Dara L. Kraitchman for taking me under her wing and introducing me to the world of clinical and preclinical research in interventional radiology and radiological sciences. From operating room surgical procedures to the analysis of tissue biopsies, from the operation of clinical scanners to veterinary care of large animal studies, my experiences have been eye-opening every step of the way. I'd also like to thank Dr. Tza-Huei Wang for giving me the opportunity to immerse in the field of microfabrication using the many state-of-the-art equipments in his lab.

I would also like to thank the mentors in each of my collaborating labs for teaching me the skills and tools of the trade. Specifically, I'd like to thank Dr. Clifford R. Weiss for taking the time to mentor me on the subjects surrounding embolic therapy and interventional radiology. I'd like to thank Dr. Peter Season providing me with an opportunity to participate in the Institute for Nanobiotechnology training program, as well as his mentorship in the bioprinting project. I'd like to thank Dr. Cyrus W. Beh for inheriting me his knowledge of microfabrication and microfluidics, as well as his invaluable advices and ideas regarding the development and implementation of the platforms used in this thesis. I'd especially like to thank Dr. Yingli Fu for sharing her expertise in cell encapsulation with me, for her endless efforts in helping me troubleshoot difficult experiments, and for her support in practically every step of the way.

Next, I'd like to thank my colleagues within the Mao lab, the Kraitchman lab, the Wang lab, and the Searson lab. In particular, I received valuable feedback, suggestions and critiques from Dr. Markus Tammia, Dr. Russ Martin, Dr. Jose Roman, Dr. Kellin Krick, Dr. Xiaowei Li, Dr. Yong Ren, Dr. Helena Zec, Dr. Andrew Wong, Brian Ginn, Sarah Hewes, and Judy Cook. Thank you to the rest of Mao lab for your support and encouragement.

I wish to express my most sincere gratitude to my friends Stephen Farias, Russ and Brittany Martin, Jose and Heather Roman, Jesse and Amanda Placone, Tom and Charli Dawidczyk, Andrew Wong – you have all made my journey at Hopkins exciting, fun, and

memorable, including everything from department softball games, outdoor rock climbing, board game nights, home-brews, crab parties, to the good old fashioned ball games!

My family has been both a support and inspiration for me. My parents gave me the freedom to choose my own path and supported every decision I made along the way. My brother and sister-in-law not only inspired me to be thorough and meticulous in all my undertakings, but also to enjoy the scenery along the way. My adorable niece is also a constant encouragement to push myself past the finish line so that I can visit her more often.

Finally, I would like to thank my fiancé, Lily Chu, for her unending support and patience throughout the lengthy Ph.D. process, especially through the extremely stressful final few months of dissertation-writing. My life has been immeasurably better for the light she has brought the past five years, and I can't wait for the adventures we will embark on next.

# Table of Contents

<b>Abstract</b> .....	ii
<b>Acknowledgements</b> .....	iv
<b>Table of Contents</b> .....	vii
<b>List of Figures</b> .....	xi
<b>Chapter 1 Limitations in Site-Specific Stem Cell Delivery for Cardiac Regenerative Therapy</b> .....	1
1.1 Introduction .....	1
1.2 Stem cells as a therapeutic agent.....	1
1.2.1 Remuscularization-based therapies .....	3
1.2.2 Paracrine-based therapies.....	4
1.3 Challenges in intracardial cell delivery .....	6
1.3.1 Administration.....	6
1.3.2 Distribution.....	7
1.3.3 Survival .....	9
1.4 Recent approaches to enhance stem cell delivery .....	11
1.4.1 Delivery using biomaterial scaffolds.....	11
1.5 Conclusion.....	14
1.6 References .....	17
<b>Chapter 2 Generating Uniform, Imaging-Visible Microcapsules Using Droplet Microfluidics-based Platform</b> .....	32
2.1 Introduction .....	32
2.1.1 X-ray-guided transarterial chemoembolization (TACE).....	32
2.1.2 Advantages of Microfluidic Preparation.....	34
2.2 Materials and Methods .....	35
2.2.1 Microfluidic device fabrication.....	35
2.2.2 Microcapsule preparation.....	36

2.2.3	Contrast agent capsule impregnation .....	37
2.2.4	Microcapsule characterization.....	37
2.2.5	IEB radiopacity .....	38
2.2.6	<i>In vivo</i> studies.....	38
2.2.7	Renal embolization.....	39
2.2.8	Gastric fundus embolization.....	40
2.2.9	Weight, blood collection and hormonal analysis .....	41
2.2.10	Endoscopy .....	42
2.2.11	Image analysis .....	42
2.2.12	Histopathological assessment .....	43
2.3	Results .....	43
2.3.1	Operation of microfluidic device .....	44
2.3.2	Properties of IEBs .....	44
2.3.3	Radiopacity of IEBs .....	46
2.3.4	Renal delivery of IEBs <i>in vivo</i> .....	46
2.3.5	Gastric delivery of IEBs <i>in vivo</i> .....	47
2.4	Discussion .....	48
2.4.1	Rationale for Microfluidic Device Design.....	49
2.4.2	Imaging-visible microcapsules allow better dosing control.....	51
2.4.3	IEBs as embolic agents .....	53
2.5	Conclusion.....	55
2.6	Figures .....	57
2.7	References .....	65

<b>Chapter 3</b>	<b>Microencapsulation of Human Mesenchymal Stem Cells and Perfluorooctyl Bromide Imaging Agent in Uniform Alginate Microcapsules using Droplet Microfluidics.....</b>	<b>72</b>
3.1	Introduction .....	72
3.2	Materials and Methods .....	74
3.2.1	Microfluidic device fabrication.....	74
3.2.2	Microcapsule preparation.....	75
3.2.3	Human mesenchymal stem cell culture and microencapsulation.....	76
3.2.4	Cell viability.....	76



3.2.5	Contrast agent impregnation .....	77
3.2.6	Microbead characterization and sterilization .....	77
3.2.7	Microcapsule radiopacity .....	79
3.2.8	<i>In vivo</i> studies.....	79
3.2.9	Image analysis.....	80
3.2.10	Histopathological assessment.....	80
3.3	Results .....	81
3.3.1	Operation of microfluidic device .....	81
3.3.2	Microcapsule size, shape, and variability (alginate vs. hMSC vs. PFOB) 82	
3.3.3	Microcapsule permeability and stability .....	82
3.3.4	Viability of microencapsulated hMSC and encapsulation efficiency .....	83
3.3.5	<i>In vitro</i> imaging properties.....	84
3.4	Discussion .....	85
3.4.1	Modifications to allow cell encapsulation.....	85
3.4.2	Microcapsule permeability and stability .....	86
3.4.3	Viability of microencapsulated hMSC and encapsulation efficiency .....	86
3.4.4	<i>In vitro</i> imaging properties.....	87
3.5	Conclusion.....	88
3.6	Figures .....	90
3.7	References .....	97

<b>Chapter 4</b>	<b>Piezoelectric Bioprinting of Human Mesenchymal Stem Cells, Induced-Pluripotent Stem Cells, and Ethiodized Oil in Alginate Microcapsules</b> .....	104
4.1	Introduction .....	104
4.1.1	Piezoelectric inkjet bioprinting .....	105
4.2	Materials and Methods .....	106
4.2.1	Cells and culture conditions .....	106
4.2.2	Microcapsule printing mechanism .....	107
4.2.3	Cell viability.....	108
4.2.4	Imaging agent preparation.....	109
4.3	Results .....	109

4.3.1	Physical characterization of bioprinted alginate microcapsules .....	109
4.3.2	Bioprinted stem cell microcapsules.....	110
4.3.3	Co-encapsulation with imaging agents .....	111
4.3.4	Co-encapsulation with biopolymer .....	111
4.4	Conclusion.....	112
4.5	Figures .....	114
4.6	References .....	120
<b>Chapter 5 Summary and Outlook .....</b>		<b>123</b>
<b>Curriculum Vitae .....</b>		<b>126</b>

## List of Figures

Figure 2-1: Overview of functional components of the microfluidic device. ....	57
Figure 2-2: Generated Microcapsules and IEBs. ....	58
Figure 2-3: IEB permeability. ....	59
Figure 2-4: Radiopacity and x-ray sensitivity of IEBs. ....	60
Figure 2-5: <i>In vivo</i> IEB renal delivery. ....	62
Figure 2-6: <i>In vivo</i> IEB gastric delivery. ....	63
Figure 2-7: IEB gastric histopathology. ....	64
Figure 3-1: Physical characterization. ....	90
Figure 3-2: Chemical and mechanical characterization. ....	91
Figure 3-3: Cell encapsulation and viability. ....	93
Figure 3-4: Radiopacity of PFOB microcapsules by cone beam computed tomography. . .....	95
Figure 4-1: Example of an actuating voltage signal to generate a droplet. ....	114
Figure 4-2: Piezoelectric bioprinter setup and schematic. ....	115
Figure 4-3: Bioprinted microcapsule size and stability. ....	116
Figure 4-4: Permeability of bioprinted alginate microcapsules. ....	117
Figure 4-5: Bioprinting of MSC and iPSC. ....	118
Figure 4-6: Co-encapsulation with imaging agents and fibrinogen. ....	119

# **Chapter 1 Limitations in Site-Specific Stem Cell Delivery for Cardiac Regenerative Therapy**

## 1.1 Introduction

Stem cell-based therapies have emerged as a promising strategy to treat many diseases by attempting to provide the body with the building blocks required for the reconstruction of damaged organs [1]. However, due to the complex nature of tissue biology, effective delivery of stem cells to targeted tissues to functionally carry out the intended therapeutic effects is a very complex undertaking. In order to overcome the physiological barriers imposed on cellular therapeutics, researchers from many disciplines, including medicine, biology, chemistry, and materials science, have come together in a highly dynamic interdisciplinary research field to develop strategies to circumvent these challenges. Currently there are two major areas of focus regarding stem cell-based therapies. The first is on improving the acute retention and subsequent survival of stem cells to effectively increase the efficacy of the therapy. The second concerns proper tissue integration to functionally replace lost cells in damaged organs. This thesis will use the heart as an example to highlight the current knowledge of therapeutic stem cell utilization relating to tissue regeneration, the existing pitfalls and limitations, and the approaches that have been developed to overcome them.

## 1.2 Stem cells as a therapeutic agent

Through decades of continued research in stem cell activity and its therapeutic potential, the scientific community have gradually moved from disease management and damage mitigation to the regeneration of tissue and functional restoration. Unlike protein and gene therapy, whose approaches are based on relatively simple macromolecules, a cell is one of the most complex biopharmaceuticals. Proteins have defined structures that induce specific responses when interacting with specific targeted receptors. In gene therapy, an intended sequence of nucleic acids is delivered to the nucleus of target cells, which in turn produces a specific effect encoded by the affected gene. Because the molecular mechanisms behind protein and gene therapy are generally well established, development in this area has been focused on improving the efficiency of its delivery to achieve more pronounced therapeutic effects. As such, protein and gene therapy approaches are generally most effective at targeting a single defect rather than eliciting a complex biological regenerative response, for which stem cells seem to be better suited. However, cells are far more complex to utilize as a therapeutic. On the one hand, cells contain an entire genome worth of genetic information capable of producing thousands of proteins. Merely based on the proteins that they secrete, cells can already be targeting a multitude of receptors. Furthermore, cells are dynamic and are able to react and secrete different proteins depending on the types and concentrations of biochemical cues they encounter. Thus, the secretory profile of a cell can be drastically different when transplanted *in vivo* compared to what is observed *in vitro* under controlled culture conditions. As such, cells can provide unique multi-dimensional therapeutic potentials suitable for tissue regenerative therapies, but at the same time their complexity makes them difficult to study.

In order to better develop strategies optimal for intracardial cell delivery, it is important to understand the mechanisms stem cells use to repair heart tissue, and the challenges recent developments have faced. Stem cells interaction with the heart can be classified into direct cell intervention (remuscularization-based therapy) where stem cells directly integrate with the cardiac muscle, and indirect cell intervention (paracrine-based therapy) where stem cells facilitate cardiac tissue repair by secreted factors.

### 1.2.1 Remuscularization-based therapies

Remuscularization-based therapies seek to repopulate the heart with cells that will help to restore the pump function of the heart after injury. Cardiomyocytes are typically used in this type of repair. Alternatively, cardiac progenitor cells (either somatic or pluripotent stem cells derived) can also be used, but would require environmental cues to drive their differentiation into heart muscle cells *in vivo* after transplantation. Therapies based on remuscularization rely on the functional integration of muscle cells into the diseased heart, where the cells must be electrically and mechanically coupled with the host tissue in order for the organ to function properly. Skeletal myoblast studies serve as a strong reminder of the specific biological requirements needed for proper coupling [2]. This study showed that the lack of expression of gap junctional protein connexin 43, which is critical for electrical propagation between adjacent cardiomyocytes, after grafting possibly led to arrhythmic side effects in clinical trials. Therefore, in order to act as tissue replacement, it is important for a cellularized therapy to adhere to the specific biological requirements of functional heart muscle.

Moreover, structural organization is also important in the cell's integration with the host tissue. In the example of the heart, striated-sarcomeric organization is of fundamental importance for force generation in cardiomyocytes. Consequently, this phenotypic trait needs to be recapitulated in the transplanted cells in order to functionally contribute in the injured organ. Since the myocardium is composed of cardiomyocyte networks, the sarcomeric architecture also needs to be properly aligned with the host myofibrils to allow for a coordinated contraction [2]. Furthermore, the grafted cardiomyocytes will also require the expression of junctional proteins, such as N-cadherin and connexin-43, along the intercalated disks, in order to physiologically integrate them to the host tissue. These intercellular connections enable the passage of ions for electrical propagation, which allow the grafted cells to contract simultaneously with the surrounding tissue. The junctional connections are also vital for force transmission from transplanted graft to the host myocardium, thereby enabling the exogenous cardiomyocytes to contribute to overall contraction of the muscle [3]. As one can see, there exists a multitude of organizational factors that must be well integrated in order to ensure an effective therapy based on direct cellular intervention.

### 1.2.2 Paracrine-based therapies

Stem cells can also facilitate cardiac tissue repair by secreted factors, although the exact targets and mechanisms by which non-cardiac progenitor cells elicit their therapeutic effects remain unknown. It is now well established that new muscle formation is not part of the observed effect, but rather the factors released by the injected cells form the basis

of the therapy. These factors can stimulate endogenous pathways, inducing angiogenesis, reducing apoptosis, or even activating the endogenous repair mechanisms, thereby attenuating the damage brought about by a myocardial infarction [4]. This ability has become known as the paracrine effect of stem cells and covers an array of cytokines and growth factors released by the cells upon their transplantation. The most striking example of paracrine effects is found in studies in which enriched culturing medium, collected after *in vitro* propagation of progenitor cells (also known as conditioned medium), is used as a therapeutic agent. In some studies [5, 6], it was demonstrated that mesenchymal stem cell-conditioned medium alone is sufficient to protect the myocardium and stimulate endogenous regenerative processes. Most notably, the activation of PIK3/Akt [7] and ERK1/2 [8] pathways has been observed after myocardial delivery of various cell types. These pathways are activated by growth factor receptors, such as EGFR and VEGFR, and elicit powerful anti-apoptotic and angiogenic signals to the heart. Some cytokines and growth factors can target remodeling and hypertrophic processes [9], while others can even stimulate the proliferation and migration of resident progenitor cells and thereby initiate endogenous regeneration [10]. Another component of the conditioned medium are nano-sized vesicles released by cells, including exosomes [11], which have also been shown to play a potent role in cardiac healing by delivering cytosolic stem cell cargo containing microRNAs and various other intracellular components [11]. Lastly, stem cells, such as mesenchymal stem cells (MSCs) and cardiac stem cells (CSCs), have immuno-modulatory properties. *In vitro*, MSCs [12] and CSCs [13, 14] have been shown to suppress the proliferation of immune cells, such as T-cells and B-cells, while selectively expanding immunosuppressive regulatory T-cells. Since inflammation after



the injury can lead to adverse remodeling in the myocardium, the ability of stem cells to reduce or modulate the overall inflammatory reaction in the heart can lead to therapeutic benefits.

### 1.3 Challenges in intracardial cell delivery

Compared to standard drug formulations, cellular therapeutics have unique physical properties that require specialized delivery strategies to the injured heart. As such, difficulties in administering the delicate stem cells may lead to poor cellular retention and survival of the cells, significantly dampening its therapeutic efficacy.

#### 1.3.1 Administration

The mode of administration of a drug directly affects its subsequent biodistribution. Although oral administration is preferred for small compounds due to the ease of intake for patients, many biopharmaceuticals [15] and cells are not capable of surviving the harsh acidic environment of the stomach, and even less likely to permeate through the intestine wall into the blood stream. The least invasive manner to inject cells into the heart is directly into the circulation by means of an intravenous injection [15]. Based on the homing potential of hematopoietic stem cells after intravenous bone marrow transplantation in leukemia patients [16], it was hypothesized that cardiac cell therapy could rely on chemo-attractant signals coming from the damaged heart to attract the circulating cells to the site of injury. However, the many obstacles present in systemic circulation proved it inefficient in delivering a therapeutic amount of cells to the damaged

heart. Alternatively, intracoronary injection allows for the administration of stem cells directly into the cardiac coronary circulation. This approach is facilitated by the fact that a large number of cardiac patients will undergo percutaneous coronary intervention (PCI) or angiography, a procedure in which a catheter is placed into the coronary vasculature [17]. The injection can also be tailored by targeting a specific coronary region that was affected by the ischemic event. Nonetheless, in such an approach, the injected cells are faced with high coronary flow and are required to transmigrate through the capillaries to reach the myocardium. Lastly, intramyocardial injection allows the administration of stem cells directly into the myocardial tissue with a minimally invasive thoracoscopic procedure or catheter-based needle injection systems [18]. This administration route is not restricted to coronary anatomy and is therefore the most direct and reliable manner to get the cells into the myocardium. Nonetheless, it can be difficult to inject the cells precisely into a preferred location, sometimes resulting in delivery into a remote region too far from the injury or into an infarcted area deprived of oxygen and nutrients [19].

### 1.3.2 Distribution

The localization and distribution of an injected drug directly affects its effectiveness in carrying out its function. Similarly, the biodistribution of the stem cells after transplantation will subsequently affect its therapeutic potential. Although a few studies have shown cell engraftment in the myocardium after intravenous injection [20, 21], the overall scientific consensus is that it remains a very inefficient process. The inability to trap intravenously injected cells could come from the lack of secreted chemo-attractant from the injury site and/or the reduced cardiac output dedicated to supplying the coronary

arteries. In biodistribution studies [22], only trace amount of radioactively labeled cells are found in the heart with the predominated signal stemming from the lungs, liver, and spleen. Substantiating the benefits of a local administration route, a comparative biodistribution study [23] of radioactively labeled BM-MNC showed a superior engraftment rate in the infarct region after intracoronary delivery compared to intravenous infusion. However, it is important to note that not all cell types will behave similarly and enter the injured areas after administration. Differences in integrin expression or other cell surface proteins could lead to altered adhesion properties, thereby changing their engraftment kinetics. In studies with larger cell types [21] such as MSCs, there is a noticeable accumulation in the lungs after systemic delivery, likely stemming from these cells inability to move beyond a given capillary bed size. In a comparative study from van der Spoel et al. [24], radioactively labeled MSCs were injected intracoronary or intramyocardially and traced for their biodistribution after 4 h. The highest accumulation from both modalities was observed in the lungs (~ 25% of total cells), while also noting off-target accumulation in the liver, spleen, and kidney. Total retention in the heart did not differ between the two techniques, with the myocardium amassing 12% of the entire radioactive tracer pool in the body. Interestingly, local inspection of cell distribution by ex vivo  $\gamma$ -scan and histology revealed a stark distinction between the two techniques. Whereas intramuscular injection tended to accumulate in a site-specific manner (high signal at the mid-papillary level) with clusters of cells in the infarcted region and border zone, intracoronary infusion led to a scattered and diffused distribution throughout the targeted myocardium. Overall, biodistribution studies have

agreed that administration of stem cells, independent of the route, remains an ineffective process.

### 1.3.3 Survival

Once the cells have arrived at the targeted tissue, they must survive a rather toxic microenvironment. After suffering an ischemic event, the damaged myocardium is under oxidative stress as the native cells die and the immune cells infiltrate to start clearing the debris. Therefore, cellular therapeutics arrive in a hostile inflammatory milieu and are thereby susceptible to pro-apoptotic signaling. A study by Zhang et al. [26] showed the profound effect of this ischemic damage on transplanted cardiomyocytes. Although grafted cells remained viable within hours of injection (2% apoptotic cells), TUNNEL-positive cells drastically increased to 30% over the first 24 h. Overall, they calculated that up to 90% of engrafted cells succumbed to these external stimuli over the course of 1 week. Nonetheless, limited apoptotic cells are observed after 1 week; therefore, cardiomyocytes that did survive the initial insult seem to be stably integrated and were able contribute therapeutically. Although cardiomyocytes are highly sensitive to apoptotic signaling, these findings are not exclusively limited to them. In CSC transplantation studies, the survival rate after intramyocardial administration was around 2% of the injected dose after 1 month [27, 28]. These observations have been further supported by numerous studies in which pro-survival strategies have been successfully implemented to make stem cells more resilient against external stimuli. Inhibiting pro-death pathways have shown the ability to increase the number of cells in the myocardium

[29–31], highlighting the indirect environmental burden that stem cells are confronted with upon their transplantation.

Transplanted stem cells are not only susceptible to cytotoxic environments, but to the immune system as well. Within the immune system's defenses is the ability to recognize and remove foreign entities from the body. As has been observed in organ transplantation therapy, HLA complexes on cells present patient-specific glycoproteins to the host immune system, which is able to distinguish “self” from “foreign,” and has made it crucial to match donor and recipient organs before the procedure [32]. For stem cells, there exists a similar threat from this direct involvement of the body immune system, although it is slightly more complex [33]. First, many of the approaches are using the patient's own stem cells for treatment, thereby circumventing the risk. Although this is an option for adult stem cells, such as bone marrow derived or resident progenitor cells, it remains a complication when establishing a therapy with embryonic stem cells. Second, certain stem cells, most notably MSC, express low levels of HLA on their surface and have inherent ability to avoid detection by the immune system. These “immune privileged” cells can even act upon and modulate the immune system [12], consequently reducing inflammation at the site of injury. Nonetheless, the immune system is a crucial aspect to consider for the successful engraftment of the stem cells since a mismatch between donor and recipient will result in complete clearance of the therapeutics from the body.

## 1.4 Recent approaches to enhance stem cell delivery

The direct injection of “naked” stem cells has been shown by many studies to have poor survival and retention rates, with around less than 3% of the injected dose remaining after several months. While there have been some efforts to enhance the retention, survival, and integration of stem cells in the heart (34–37), recent research sought to improve cell-based therapies by modulating the performance of the stem cells, including pre-treatment of the cells, genetic manipulation, and material incorporation. In the former case, cells can be “primed” with physical, biological, or pharmacological treatments to activate signaling cascades in cells to turn on processes that are fundamentally important for their survival and/or subsequent biological activity [38-98]. Similarly, stem cell performance can be enhanced by modifying their underlying genetic blueprint to display extrinsic functional properties that maximize survivability or even therapeutic effects [99-118]. For the purposes of this thesis, we decided to place emphasis on latter strategy that utilize biomaterials to provide support and protection to the stem cells in paracrine-based therapeutic applications.

### 1.4.1 Delivery using biomaterial scaffolds

More recently, the use of biomaterials has emerged as an alternative approach to enhance the delivery of cells after transplantation into the infarcted myocardium. The properties of materials can physically support the cells to improve retention directly after administration and can further provide a protective environment to enhance the survival of the cellular cargo. Materials can also contain beneficial cues to modulate stem cell behavior and optimize the desired cellular response [61–64]. Different types of

biomaterial have been used to transplant stem cells [65–69], either natural derived or synthetic. Among the natural biomaterials, collagen [70–73], fibrin [74, 75], Matrigel [76], alginate [69], hyaluronic acid [77], and tissue-derived ECM [68] hydrogels are the most commonly used. Among the synthetic materials, peptide nanofibers [78] and poly(lactide-co- $\epsilon$ -caprolactone) [79] are the most frequently used for stem cell delivery. There are two main engineering approaches that have been explored with materials: patches and injectables.

Patch-based approaches are usually characterized by the generation of a tissue-like structure *in vitro*, which is then transplanted *in vivo*. The main advantage of this approach is that the cells are cultivated under precise culture conditions and proliferation, differentiation, and tissue structure can be tightly monitored to enhance stem cell survival. One of the main limitations of this approach is nutrient diffusion that usually limits the thickness of the constructs and long-term *in vitro* culture. The use of tissue printing technology may overcome this limitation. Recently, CSCs have been printed in alginate [80] and gelatin/hyaluronic acid scaffolds [77]. The particular porous structure, which can be achieved by tissue printing technology, preserves cell viability up to 4 weeks in culture when compared with a nonporous structure [80]. Similarly to other patch-based approaches, the construct can be transplanted *in vivo* in a myocardial infarction model leading to a significant reduction in adverse remodeling and an increase in cell survival [77]. One potential obstacle to patch-based transplantation is inadequate integration of the graft with the host myocardium. Although in paracrine-based strategies secreted factors

can easily cross this barrier, it might hinder proper coupling of cardiomyocytes with the native myocardium in remuscularization-based therapies.

Injectable approaches are based on the injection of biomaterials and cells directly into the ventricular wall. Cells and matrix are mixed before transplantation and delivered through direct needle injection into the ventricular wall (epicardial injection) or a percutaneous catheter (transendocardial injection). The injectable approach takes advantage of the natural environment of the cardiac tissue to promote stem cell functionality and directly stimulates tissue repair at the site of implantation. The biomaterial should be liquid until the administration and undergo rapidly gelation after transplantation to avoid cell washout. Therefore, pH or temperature responsive materials that gel at physiological conditions (pH 7.4/37 °C) are often utilized to promote cellular encapsulation. Another potentially injectable application is based on the use of microspheres as cell carrier. Stem cells can be encapsulated into or attached to microspheres and delivered into the myocardium [81–83]. The biomaterial can also be functionalized with adhesion peptides [83] or growth factors [82] to enhance stem cell engraftment and survival [25] and [84].

When used in combination with stem cells, either injected or as a patch, all of the biomaterials mentioned above have been proven to be effective in enhancing cell engraftment and survival when compared to cell injection only. However, enhancing stem cell retention may not be enough to improve the beneficial effects of cell therapy alone. Recently biomaterials have also emerged as important support for stem cell



differentiation and influence many biological processes including the endogenous regeneration. Different characteristics of a biomaterial can influence stem cell functionality upon transplantation. Natural biomaterials such as tissue-specific decellularized extracellular matrix contain many desirable pro-regenerative cues, such as sulfated glycosaminoglycans or tissue-specific ECM proteins, and may be advantageous in driving cardiac differentiation [68]. Matrix mechanical properties and stiffness is also known to influence cell phenotype [85–87], so it may be favorable to design a biomaterial with similar stiffness to the healthy tissue, although the ideal mechanical properties are currently unknown. In short, many different design criteria should be considered when selecting a biomaterial for stem cell transplantation such as construct generation strategy and delivery method, gelation kinetics and stem cell engraftment, mechanical and biochemical composition, degradation products, biocompatibility, and electrical properties.

## 1.5 Conclusion

In summary, stem cell-based therapy has garnered a lot of traction in recent years as an effective tool to facilitate repair and regeneration of diseased organs. However, recent advances in site-specific delivery have been met with challenges, especially in intracardial delivery. These challenges include the lack of retention of effective doses of therapeutic cells in regions of pathology, and the inability of the therapeutic components to functionally integrate with the host tissue. This thesis explores several strategies in enhancing the delivery mechanism as well as the therapeutic effectiveness of the delivered stem cells. It contains the following specific aims:

*Specific Aim 1: Generating highly uniform, imaging –visible microcapsules using droplet microfluidics.* By utilizing microfluidics technology, hydrogel microcapsules can be produced with smaller sizes and higher uniformity compared to conventional microcapsules, leading to deeper vascular penetration allowing for more site-specific delivery. The reduced capsule profile eliminates the need to use custom microcatheters with larger diameters, which in turn may minimize side-effects associated with intracardial delivery of larger microcapsules, such as blockages and microembolisms. Furthermore, the co-encapsulation of imaging agents allow for long-term noninvasive tracking of the microcapsules.

*Specific Aim 2: Encapsulation of stem cells and imaging agents using droplet-microfluidics-based platform.* Alginate hydrogel provides microcapsules with a selectively-permeable encapsulation matrix that allows the diffusion of nutrients and the filtration of immunogenic macromolecules. The encapsulated stem cells are protected from many of the toxic elements associated with naked cell delivery to pathological tissues, and are viable for long-term transplantation. The co-delivery of imaging-visible microcapsules also allows for long-term noninvasive tracking.

*Specific Aim 3: Piezoelectric inkjet bioprinting of microcapsules containing stem cells, imaging agents, and biopolymers.* While microfluidics devices places limitations on throughput and surface properties of the aqueous solution used, the piezoelectric bioprinting platform enables microcapsule production with a wider range of materials at higher throughputs. Incorporation of biopolymers into the hydrogel matrix may provide adhesion sites stem cells need for improved metabolism and survival. At the same time, the printing of biopolymer-hydrogel composite microcapsules may enable controlled

degradation of targeted structures, achieving microcapsules with dynamic pore sizes or with pure biopolymer compositions that are otherwise difficult to produce.

## 1.6 References

- [1] D.A.M. Feyen, R. Gaetani, P.A. Doevendans, J.P.G. Sluiter, Stem cell-based therapy: Improving myocardial cell delivery, *Adv. Drug Deliv. Rev.* 106A (2016) 104-115.
- [2] E. Braunwald, *Heart, Annu. Rev. Physiol.* 28 (1966) 227–266.
- [3] F. Sheikh, R.S. Ross, J. Chen, Cell–cell connection to cardiac disease, *Trends Cardiovasc. Med.* 19 (2009) 182–190.
- [4] Y. Qu, Z. Duan, F. Zhao, D. Wei, J. Zhang, B. Tang, J. Li, C. Yang, D. Mu, Telomerase reverse transcriptase upregulation attenuates astrocyte proliferation and promotes neuronal survival in the hypoxic–ischemic rat brain, *Stroke* 42 (2011) 3542–3550.
- [5] R. Madonna, D.A. Taylor, Y.J. Geng, R. De Caterina, H. Shelat, E.C. Perin, J.T. Willerson, Transplantation of mesenchymal cells rejuvenated by the overexpression of telomerase and myocardin promotes revascularization and tissue repair in a murine model of hindlimb ischemia, *Circ. Res.* 113 (2013) 902–914.
- [6] M.E. Carlson, C. Suetta, M.J. Conboy, P. Aagaard, A. Mackey, M. Kjaer, I. Conboy, Molecular aging and rejuvenation of human muscle stem cells, *EMBO Mol. Med.* 1 (2009) 381–391.
- [7] L. Zhao, A.L. Borikova, R. Ben-Yair, B. Guner-Ataman, C.A. MacRae, R.T. Lee, C.G. Burns, C.E. Burns, Notch signaling regulates cardiomyocyte proliferation during zebrafish heart regeneration, *Proc. Natl. Acad. Sci. U. S. A.* 111 (2014) 1403–1408.

- [8] M. Nemir, M. Metrich, I. Plaisance, M. Lepore, S. Cruchet, C. Berthonneche, A. Sarre, F. Radtke, T. Pedrazzini, The notch pathway controls fibrotic and regenerative repair in the adult heart, *Eur. Heart J.* 35 (2014) 2174–2185.
- [9] S. Mohsin, M. Khan, J. Nguyen, M. Alkatib, S. Siddiqi, N. Hariharan, K. Wallach, M. Monsanto, N. Gude, W. Dembitsky, M.A. Sussman, Rejuvenation of human cardiac progenitor cells with Pim-1 kinase, *Circ. Res.* 113 (2013) 1169–1179.
- [10] S. Mohsin, M. Khan, H. Toko, B. Bailey, C.T. Cottage, K. Wallach, D. Nag, A. Lee, S. Siddiqi, F. Lan, K.M. Fischer, N. Gude, P. Quijada, D. Avitabile, S. Truffa, B. Collins, W. Dembitsky, J.C. Wu, M.A. Sussman, Human cardiac progenitor cells engineered with Pim-I kinase enhance myocardial repair, *J. Am. Coll. Cardiol.* 60 (2012) 1278–1287.
- [11] K.M. Fischer, C.T. Cottage, W. Wu, S. Din, N.A. Gude, D. Avitabile, P. Quijada, B.L. Collins, J. Fransioli, M.A. Sussman, Enhancement of myocardial regeneration through genetic engineering of cardiac progenitor cells expressing Pim-1 kinase, *Circulation* 120 (2009) 2077–2087.
- [12] G.A. Borillo, M. Mason, P. Quijada, M. Volkers, C. Cottage, M. McGregor, S. Din, K. Fischer, N. Gude, D. Avitabile, S. Barlow, R. Alvarez, S. Truffa, R. Whittaker, M.S. Glassy, A.B. Gustafsson, S. Miyamoto, C.C. Glembotski, R.A. Gottlieb, J.H. Brown, M.A. Sussman, Pim-1 kinase protects mitochondrial integrity in cardiomyocytes, *Circ. Res.* 106 (2010) 1265–1274.
- [13] S. Hu, M. Huang, P.K. Nguyen, Y. Gong, Z. Li, F. Jia, F. Lan, J. Liu, D. Nag, R.C. Robbins, J.C. Wu, Novel microRNA prosurvival cocktail for improving engraftment

- and function of cardiac progenitor cell transplantation, *Circulation* 124 (2011) S27–S34.
- [14] D. Dakhllallah, J. Zhang, L. Yu, C.B. Marsh, M.G. Angelos, M. Khan, MicroRNA-133a engineered mesenchymal stem cells augment cardiac function and cell survival in the infarct heart, *J. Cardiovasc. Pharmacol.* 65 (2015) 241–251.
- [15] A.J. Boyle, S.P. Schulman, J.M. Hare, P. Oettgen, Is stem cell therapy ready for patients? Stem cell therapy for cardiac repair. Ready for the next step, *Circulation* 114 (2006) 339–352.
- [16] E.D. Thomas, R.B. Epstein, Bone marrow transplantation in acute leukemia, *Cancer Res.* 25 (1965) 1521–1524.
- [17] S.L. Chen, W.W. Fang, F. Ye, Y.H. Liu, J. Qian, S.J. Shan, J.J. Zhang, R.Z. Chunhua, L.M. Liao, S. Lin, J.P. Sun, Effect on left ventricular function of intracoronary transplantation of autologous bone marrow mesenchymal stem cell in patients with acute myocardial infarction, *Am. J. Cardiol.* 94 (2004) 92–95.
- [18] W. Sherman, T.P. Martens, J.F. Viles-Gonzalez, T. Siminiak, Catheter-based delivery of cells to the heart, *nature clinical practice, Cardiovasc. Med.* 3 (Suppl. 1) (2006) S57–S64.
- [19] S. Dimmeler, A.M. Zeiher, M.D. Schneider, Unchain my heart: the scientific foundations of cardiac repair, *J. Clin. Invest.* 115 (2005) 572–583.
- [20] N. Nagaya, T. Fujii, T. Iwase, H. Ohgushi, T. Itoh, M. Uematsu, M. Yamagishi, H. Mori, K. Kangawa, S. Kitamura, Intravenous administration of mesenchymal stem

- cells improves cardiac function in rats with acute myocardial infarction through angiogenesis and myogenesis, *Am. J. Physiol. Heart Circ. Physiol.* 287 (2004) H2670–H2676.
- [21] I.M. Barbash, P. Chouraqui, J. Baron, M.S. Feinberg, S. Etzion, A. Tessone, L. Miller, E. Guetta, D. Zipori, L.H. Kedes, R.A. Kloner, J. Leor, Systemic delivery of bone marrow-derived mesenchymal stem cells to the infarcted myocardium: feasibility, cell migration, and body distribution, *Circulation* 108 (2003) 863–868.
- [22] B.B. Chin, Y. Nakamoto, J.W. Bulte, M.F. Pittenger, R. Wahl, D.L. Kraitchman, 111-Inoxine labelled mesenchymal stem cell SPECT after intravenous administration in myocardial infarction, *Nucl. Med. Commun.* 24 (2003) 1149–1154.
- [23] M. Hofmann, K.C. Wollert, G.P. Meyer, A. Menke, L. Arseniev, B. Hertenstein, A. Ganser, W.H. Knapp, H. Drexler, Monitoring of bone marrow cell homing into the infarcted human myocardium, *Circulation* 111 (2005) 2198–2202.
- [24] T.I. van der Spoel, K.R. Vrijssen, S. Koudstaal, J.P. Sluijter, J.F. Nijssen, H.W. de Jong, I.E. Hoefler, M.J. Cramer, P.A. Doevendans, E. van Belle, S.A. Chamuleau, Transendocardial cell injection is not superior to intracoronary infusion in a porcine model of ischaemic cardiomyopathy: a study on delivery efficiency, *J. Cell. Mol. Med.* 16 (2012) 2768–2776.
- [25] F. van den Akker, D.A. Feyen, P. van den Hoogen, L.W. van Laake, E.C. van Eeuwijk, I. Hoefler, G. Pasterkamp, S.A. Chamuleau, P.F. Grundeman, P.A. Doevendans, J.P. Sluijter, Intramyocardial stem cell injection: go(ne) with the flow, *Eur. Heart J.* (2016) (accepted for publication) [Epub ahead of print].

- [26] M. Zhang, D. Methot, V. Poppa, Y. Fujio, K. Walsh, C.E. Murry, Cardiomyocyte grafting for cardiac repair: graft cell death and anti-death strategies, *J. Mol. Cell. Cardiol.* 33 (2001) 907–921.
- [27] A.M. Smits, L.W. van Laake, K. den Ouden, C. Schreurs, K. Szuhai, C.J. van Echteld, C.L. Mummery, P.A. Doevendans, M.J. Goumans, Human cardiomyocyte progenitor cell transplantation preserves long-term function of the infarcted mouse myocardium, *Cardiovasc. Res.* 83 (2009) 527–535.
- [28] D. Feyen, R. Gaetani, J. Liu, W. Noort, A. Martens, K. den Ouden, P.A. Doevendans, J.P. Sluijter, Increasing short-term cardiomyocyte progenitor cell (CMPC) survival by necrostatin-1 did not further preserve cardiac function, *Cardiovasc. Res.* 99 (2013) 83–91.
- [29] W.A. Noort, D. Feye, F. Van Den Akker, D. Stecher, S.A. Chamuleau, J.P. Sluijter, P.A. Doevendans, Mesenchymal stromal cells to treat cardiovascular disease: strategies to improve survival and therapeutic results, *Panminerva Med.* 52 (2010) 27–40.
- [30] W. Chang, B.W. Song, S. Lim, H. Song, C.Y. Shim, M.J. Cha, D.H. Ahn, Y.G. Jung, D.H. Lee, J.H. Chung, K.D. Choi, S.K. Lee, N. Chung, S.K. Lee, Y. Jang, K.C. Hwang, Mesenchymal stem cells pretreated with delivered Hph-1-Hsp70 protein are protected from hypoxia-mediated cell death and rescue heart functions from myocardial injury, *Stem Cells* 27 (2009) 2283–2292.
- [31] M.A. Laflamme, K.Y. Chen, A.V. Naumova, V. Muskheli, J.A. Fugate, S.K. Dupras, H. Reinecke, C. Xu, M. Hassanipour, S. Police, C. O'Sullivan, L. Collins, Y. Chen, E.



- Minami, E.A. Gill, S. Ueno, C. Yuan, J. Gold, C.E. Murry, Cardiomyocytes derived from human embryonic stem cells in pro-survival factors enhance function of infarcted rat hearts, *Nat. Biotechnol.* 25 (2007) 1015–1024.
- [32] P.I. Terasaki, J.M. Cecka, S. Takemoto, J. Yuge, M.R. Mickey, M.S. Park, Y. Iwaki, J. Cicciarelli, Y. Cho, Clinical transplants 1988. Overview, *Clin. Transpl.*, (1988) 409–434.
- [33] J.A. Bradley, E.M. Bolton, R.A. Pedersen, Stem cell medicine encounters the immune system, *nature reviews, Immunology* 2 (2002) 859–871.
- [34] J.J. Chong, X. Yang, C.W. Don, E. Minami, Y.W. Liu, J.J. Weyers, W.M. Mahoney, B. Van Biber, S.M. Cook, N.J. Palpant, J.A. Gantz, J.A. Fugate, V. Muskheli, G.M. Gough, K.W. Vogel, C.A. Astley, C.E. Hotchkiss, A. Baldessari, L. Pabon, H. Reinecke, E.A. Gill, V. Nelson, H.P. Kiem, M.A. Laflamme, C.E. Murry, Human embryonic-stem-cell-derived cardiomyocytes regenerate non-human primate hearts, *Nature* 510 (2014) 273–277.
- [35] Y. Shiba, S. Fernandes, W.Z. Zhu, D. Filice, V. Muskheli, J. Kim, N.J. Palpant, J. Gantz, K.W. Moyes, H. Reinecke, B. Van Biber, T. Dardas, J.L. Mignone, A. Izawa, R. Hanna, M. Viswanathan, J.D. Gold, M.I. Kotlikoff, N. Sarvazyan, M.W. Kay, C.E. Murry, M.A. Laflamme, Human ES-cell-derived cardiomyocytes electrically couple and suppress arrhythmias in injured hearts, *Nature* 489 (2012) 322–325.
- [36] W.Z. Zhu, D. Filice, N.J. Palpant, M.A. Laflamme, Methods for assessing the electromechanical integration of human pluripotent stem cell-derived cardiomyocyte grafts, *Methods Mol. Biol.* 1181 (2014) 229–247.

- [37] H. Reinecke, M. Zhang, T. Bartosek, C.E. Murry, Survival, integration, and differentiation of cardiomyocyte grafts: a study in normal and injured rat hearts, *Circulation* 100 (1999) 193–202.
- [38] R. Das, H. Jahr, G.J. van Osch, E. Farrell, The role of hypoxia in bone marrow-derived mesenchymal stem cells: considerations for regenerative medicine approaches, *Tissue Eng. B Rev.* 16 (2010) 159–168.
- [39] I. Rosova, M. Dao, B. Capoccia, D. Link, J.A. Nolte, Hypoxic preconditioning results in increased motility and improved therapeutic potential of human mesenchymal stem cells, *Stem Cells* 26 (2008) 2173–2182.
- [40] X. Hu, S.P. Yu, J.L. Fraser, Z. Lu, M.E. Ogle, J.A. Wang, L. Wei, Transplantation of hypoxia-preconditioned mesenchymal stem cells improves infarcted heart function via enhanced survival of implanted cells and angiogenesis, *J. Thorac. Cardiovasc. Surg.* 135 (2008) 799–808.
- [41] Y.L. Tang, W. Zhu, M. Cheng, L. Chen, J. Zhang, T. Sun, R. Kishore, M.I. Phillips, D.W. Losordo, G. Qin, Hypoxic preconditioning enhances the benefit of cardiac progenitor cell therapy for treatment of myocardial infarction by inducing CXCR4 expression, *Circ. Res.* 104 (2009) 1209–1216.
- [42] A.S. Sreedhar, P. Csermely, Heat shock proteins in the regulation of apoptosis: new strategies in tumor therapy: a comprehensive review, *Pharmacol. Ther.* 101 (2004) 227–257.

- [43] K. Suzuki, R.T. Smolenski, J. Jayakumar, B. Murtuza, N.J. Brand, M.H. Yacoub, Heat shock treatment enhances graft cell survival in skeletal myoblast transplantation to the heart, *Circulation* 102 (2000) III216–III221.
- [44] M.A. Laflamme, J. Gold, C. Xu, M. Hassanipour, E. Rosler, S. Police, V. Muskheli, C.E. Murry, Formation of human myocardium in the rat heart from human embryonic stem cells, *Am. J. Pathol.* 167 (2005) 663–671.
- [45] Y.J. Yang, H.Y. Qian, J. Huang, J.J. Li, R.L. Gao, K.F. Dou, G.S. Yang, J.T. Willerson, Y.J. Geng, Combined therapy with simvastatin and bone marrow-derived mesenchymal stem cells increases benefits in infarcted swine hearts, *Arterioscler. Thromb. Vasc. Biol.* 29 (2009) 2076–2082.
- [46] Y.J. Yang, H.Y. Qian, J. Huang, Y.J. Geng, R.L. Gao, K.F. Dou, G.S. Yang, J.J. Li, R. Shen, Z.X. He, M.J. Lu, S.H. Zhao, Atorvastatin treatment improves survival and effects of implanted mesenchymal stem cells in post-infarct swine hearts, *Eur. Heart J.* 29 (2008) 1578–1590.
- [47] S. Wisel, M. Khan, M.L. Kuppusamy, I.K. Mohan, S.M. Chacko, B.K. Rivera, B.C. Sun, K. Hideg, P. Kuppusamy, Pharmacological preconditioning of mesenchymal stem cells with trimetazidine (1-[2,3,4-trimethoxybenzyl]piperazine) protects hypoxic cells against oxidative stress and enhances recovery of myocardial function in infarcted heart through Bcl-2 expression, *J. Pharmacol. Exp. Ther.* 329 (2009) 543–550.

- [48] J. Pons, Y. Huang, J. Arakawa-Hoyt, D. Washko, J. Takagawa, J. Ye, W. Grossman, H. Su, VEGF improves survival of mesenchymal stem cells in infarcted hearts, *Biochem. Biophys. Res. Commun.* 376 (2008) 419–422.
- [49] N. Kanemitsu, K. Tambara, G.U. Premaratne, Y. Kimura, S. Tomita, T. Kawamura, K. Hasegawa, Y. Tabata, M. Komeda, Insulin-like growth factor-1 enhances the efficacy of myoblast transplantation with its multiple functions in the chronic myocardial infarction rat model, *J. Heart Lung Transplant.* 25 (2006) 1253–1262.
- [50] M.E. Davis, P.C. Hsieh, T. Takahashi, Q. Song, S. Zhang, R.D. Kamm, A.J. Grodzinsky, P. Anversa, R.T. Lee, Local myocardial insulin-like growth factor 1 (IGF-1) delivery with biotinylated peptide nanofibers improves cell therapy for myocardial infarction, *Proc. Natl. Acad. Sci. U. S. A.* 103 (2006) 8155–8160.
- [51] R. Madonna, L. Rinaldi, C. Rossi, Y.J. Geng, R. De Caterina, Prostacyclin improves transcoronary myocardial delivery of adipose tissue-derived stromal cells, *Eur. Heart J.* 27 (2006) 2054–2061.
- [52] Y.L. Tang, Y. Tang, Y.C. Zhang, K. Qian, L. Shen, M.I. Phillips, Improved graft mesenchymal stem cell survival in ischemic heart with a hypoxia-regulated heme oxygenase-1 vector, *J. Am. Coll. Cardiol.* 46 (2005) 1339–1350.
- [53] A.A. Mangi, N. Noiseux, D. Kong, H. He, M. Rezvani, J.S. Ingwall, V.J. Dzau, Mesenchymal stem cells modified with Akt prevent remodeling and restore performance of infarcted hearts, *Nat. Med.* 9 (2003) 1195–1201.
- [54] M. Gneocchi, H. He, N. Noiseux, O.D. Liang, L. Zhang, F. Morello, H. Mu, L.G. Melo, R.E. Pratt, J.S. Ingwall, V.J. Dzau, Evidence supporting paracrine hypothesis

- for Aktmodified mesenchymal stem cell-mediated cardiac protection and functional improvement, *FASEB J.* 20 (2006) 661–669.
- [55] J. Huang, Z. Zhang, J. Guo, A. Ni, A. Deb, L. Zhang, M. Mirosou, R.E. Pratt, V.J. Dzau, Genetic modification of mesenchymal stem cells overexpressing CCR1 increases cell viability, migration, engraftment, and capillary density in the injured myocardium, *Circ. Res.* 106 (2010) 1753–1762.
- [56] Z. Cheng, L. Ou, X. Zhou, F. Li, X. Jia, Y. Zhang, X. Liu, Y. Li, C.A. Ward, L.G. Melo, D. Kong, Targeted migration of mesenchymal stem cells modified with CXCR4 gene to infarcted myocardium improves cardiac performance, *Mol. Ther.* 16 (2008) 571–579.
- [57] A.G. Bodnar, M. Ouellette, M. Frolkis, S.E. Holt, C.P. Chiu, G.B. Morin, C.B. Harley, J.W. Shay, S. Lichtsteiner, W.E. Wright, Extension of life-span by introduction of telomerase into normal human cells, *Science* 279 (1998) 349–352.
- [58] H.M. Jan, M.F. Wei, C.L. Peng, S.J. Lin, P.S. Lai, M.J. Shieh, The use of polyethylenimine–DNA to topically deliver hTERT to promote hair growth, *Gene Ther.* 19 (2012) 86–93.
- [59] J.P. Sluijter, A. van Mil, P. van Vliet, C.H. Metz, J. Liu, P.A. Doevendans, M.J. Goumans, MicroRNA-1 and –499 regulate differentiation and proliferation in humanderived cardiomyocyte progenitor cells, *Arterioscler. Thromb. Vasc. Biol.* 30 (2010) 859–868.
- [60] T. Hosoda, H. Zheng, M. Cabral-da-Silva, F. Sanada, N. Ide-Iwata, B. Ogorek, J. Ferreira-Martins, C. Arranto, D. D'Amario, F. del Monte, K. Urbanek, D.A.

- D'Alessandro, R.E. Michler, P. Anversa, M. Rota, J. Kajstura, A. Leri, Human cardiac stem cell differentiation is regulated by a mircrine mechanism, *Circulation* 123 (2011) 1287–1296.
- [61] M. Radisic, K.L. Christman, Materials science and tissue engineering: repairing the heart, *Mayo Clin. Proc.* 88 (2013) 884–898.
- [62] J.W. Buikema, P. Van Der Meer, J.P. Sluijter, I.J. Domian, Concise review: engineering myocardial tissue: the convergence of stem cells biology and tissue engineering technology, *Stem Cells* 31 (2013) 2587–2598.
- [63] K.Y. Ye, L.D. Black III, Strategies for tissue engineering cardiac constructs to affect functional repair following myocardial infarction, *J. Cardiovasc. Transl. Res.* 4 (2011) 575–591.
- [64] R. Gaetani, G. Rizzitelli, I. Chimenti, L. Barile, E. Forte, V. Ionta, F. Angelini, J.P. Sluijter, A. Barbeta, E. Messina, G. Frati, Cardiospheres and tissue engineering for myocardial regeneration: potential for clinical application, *J. Cell. Mol. Med.* 14 (2010) 1071–1077.
- [65] H.D. Guo, H.J. Wang, Y.Z. Tan, J.H. Wu, Transplantation of marrow-derived cardiac stem cells carried in fibrin improves cardiac function after myocardial infarction, *Tissue Eng. A* 17 (2011) 45–58.
- [66] M.E. Danoviz, J.S. Nakamuta, F.L. Marques, L. dos Santos, E.C. Alvarenga, A.A. dos Santos, E.L. Antonio, I.T. Schettert, P.J. Tucci, J.E. Krieger, Rat adipose tissue-derived stem cells transplantation attenuates cardiac dysfunction post infarction and biopolymers enhance cell retention, *PLoS One* 5 (2010), e12077.

- [67] J. Wang, W. Cui, J. Ye, S. Ji, X. Zhao, L. Zhan, J. Feng, Z. Zhang, Y. Zhao, A cellular delivery system fabricated with autologous BMSCs and collagen scaffold enhances angiogenesis and perfusion in ischemic hind limb, *J. Biomed. Mater. Res. A* 100 (2012) 1438–1447.
- [68] R. Gaetani, C. Yin, N. Srikumar, R. Braden, P.A. Doevendans, J.P. Sluijter, K.L. Christman, Cardiac derived extracellular matrix enhances cardiogenic properties of human cardiac progenitor cells, *Cell Transplant.* (2015).
- [69] E.T. Roche, C.L. Hastings, S.A. Lewin, D.E. Shvartsman, Y. Brudno, N.V. Vasilyev, F.J. O'Brien, C.J. Walsh, G.P. Duffy, D.J. Mooney, Comparison of biomaterial delivery vehicles for improving acute retention of stem cells in the infarcted heart, *Biomaterials* 35 (2014) 6850–6858.
- [70] W. Dai, S.L. Hale, G.L. Kay, A.J. Jyrala, R.A. Kloner, Delivering stem cells to the heart in a collagen matrix reduces relocation of cells to other organs as assessed by nanoparticle technology, *Regen. Med.* 4 (2009) 387–395.
- [71] J.R. Frederick, J.R. Fitzpatrick, R.C. McCormick, D.A. Harris, A.-Y. Kim, J.R. Muenzer, N. Marotta, M.J. Smith, J.E. Cohen, W. Hiesinger, P. Atluri, Y.J. Woo, Stromal cell derived factor-1 $\alpha$  activation of tissue-engineered endothelial progenitor cell matrix enhances ventricular function after myocardial infarction by inducing Neovasculogenesis, *Circulation* 122 (2010) S107–S117.
- [72] D. Simpson, H. Liu, T.H. Fan, R. Nerem, S.C. Dudley Jr., A tissue engineering approach to progenitor cell delivery results in significant cell engraftment and improved myocardial remodeling, *Stem Cells* 25 (2007) 2350–2357.

- [73] N.L. Tulloch, V. Muskheli, M.V. Razumova, F.S. Korte, M. Regnier, K.D. Hauch, L. Pabon, H. Reinecke, C.E. Murry, Growth of engineered human myocardium with mechanical loading and vascular coculture, *Circ. Res.* 109 (2011) 47–59.
- [74] K.L. Christman, A.J. Vardanian, Q. Fang, R.E. Sievers, H.H. Fok, R.J. Lee, Injectable fibrin scaffold improves cell transplant survival, reduces infarct expansion, and induces neovasculature formation in ischemic myocardium, *J. Am. Coll. Cardiol.* 44 (2004) 654–660.
- [75] J. Liu, Q. Hu, Z. Wang, C. Xu, X. Wang, G. Gong, A. Mansoor, J. Lee, M. Hou, L. Zeng, J.R. Zhang, M. Jerosch-Herold, T. Guo, R.J. Bache, J. Zhang, Autologous stem cell transplantation for myocardial repair, *Am. J. Physiol. Heart Circ. Physiol.* 287 (2004) H501–H511.
- [76] T. Kofidis, D.R. Lebl, E.C. Martinez, G. Hoyt, M. Tanaka, R.C. Robbins, Novel injectable bioartificial tissue facilitates targeted, less invasive, large-scale tissue restoration on the beating heart after myocardial injury, *Circulation* 112 (2005) I173–I177.
- [77] R. Gaetani, D.A. Feyen, V. Verhage, R. Slaats, E. Messina, K.L. Christman, A. Giacomello, P.A. Doevendans, J.P. Sluijter, Epicardial application of cardiac progenitor cells in a 3D-printed gelatin/hyaluronic acid patch preserves cardiac function after myocardial infarction, *Biomaterials* 61 (2015) 339–348.
- [78] Y.D. Lin, M.L. Yeh, Y.J. Yang, D.C. Tsai, T.Y. Chu, Y.Y. Shih, M.Y. Chang, Y.W. Liu, A.C. Tang, T.Y. Chen, C.Y. Luo, K.C. Chang, J.H. Chen, H.L. Wu, T.K. Hung, P.C. Hsieh, Intramyocardial peptide nanofiber injection improves postinfarction



- ventricular remodeling and efficacy of bone marrow cell therapy in pigs, *Circulation* 122 (2010) S132–S141.
- [79] J. Jin, S.I. Jeong, Y.M. Shin, K.S. Lim, H. Shin, Y.M. Lee, H.C. Koh, K.S. Kim, Transplantation of mesenchymal stem cells within a poly(lactide-co-epsilon-caprolactone) scaffold improves cardiac function in a rat myocardial infarction model, *Eur. J. Heart Fail.* 11 (2009) 147–153.
- [80] R. Gaetani, P.A. Doevendans, C.H. Metz, J. Alblas, E. Messina, A. Giacomello, J.P. Sluijter, Cardiac tissue engineering using tissue printing technology and human cardiac progenitor cells, *Biomaterials* 33 (2012) 1782–1790.
- [81] R.G. Gomez-Mauricio, A. Acarregui, F.M. Sanchez-Margallo, V. Crisostomo, I. Gallo, R.M. Hernandez, J.L. Pedraz, G. Orive, M.F. Martin-Cancho, A preliminary approach to the repair of myocardial infarction using adipose tissue-derived stem cells encapsulated in magnetic resonance-labelled alginate microspheres in a porcine model, *Eur. J. Pharm. Biopharm.* 84 (2013) 29–39.
- [82] R. Madonna, L. Petrov, M.A. Teberino, L. Manzoli, J.P. Karam, F.V. Renna, P. Ferdinandy, C.N. Montero-Menei, S. Yla-Herttuala, R. De Caterina, Transplantation of adipose tissue mesenchymal cells conjugated with VEGF-releasing microcarriers promotes repair in murine myocardial infarction, *Cardiovasc. Res.* 108 (2015) 39–49.
- [83] J. Yu, K.T. Du, Q. Fang, Y. Gu, S.S. Mihardja, R.E. Sievers, J.C. Wu, R.J. Lee, The use of human mesenchymal stem cells encapsulated in RGD modified alginate microspheres in the repair of myocardial infarction in the rat, *Biomaterials* 31 (2010) 7012–7020.

- [84] D. Feyen, R. Gaetani, J. Deddens, D. van Keulen, C. van Opbergen, M. Poldervaart, J. Alblas, S. Chamuleau, L. van Laake, P. Doevendans, J. Sluijter, Gelatin microspheres as vehicle for cardiac progenitor cells delivery to the myocardium, *Adv. Healthc. Mater.* (2016) (in press), <http://dx.doi.org/10.1002/adhm.201500861>.
- [85] A.J. Engler, S. Sen, H.L. Sweeney, D.E. Discher, Matrix elasticity directs stem cell lineage specification, *Cell* 126 (2006) 677–689.
- [86] J.R. Gershlak, J.I. Resnikoff, K.E. Sullivan, C. Williams, R.M. Wang, L.D. Black 3rd, Mesenchymal stem cells ability to generate traction stress in response to substrate stiffness is modulated by the changing extracellular matrix composition of the heart during development, *Biochem. Biophys. Res. Commun.* 439 (2013) 161–166.
- [87] Y. Qiu, A.F. Bayomy, M.V. Gomez, M. Bauer, P. Du, Y. Yang, X. Zhang, R. Liao, A role for matrix stiffness in the regulation of cardiac side population cell function, *Am. J. Physiol. Heart Circ. Physiol.* 308 (2015) H990–H997.

## Chapter 2 Generating Uniform, Imaging-Visible Microcapsules Using Droplet Microfluidics-based Platform

### 2.1 Introduction

Successful cellular microencapsulation relies heavily on the physical and chemical properties of the artificial matrix in which the encapsulated stem cells reside. Before we attempt cellular encapsulation, we aimed at developing a platform capable of producing small, robust, spherical hydrogel microcapsules that can withstand the delivery procedure and hostile microenvironments present at the pathological tissues. Furthermore, we sought to embed sensitive imaging agents within the microcapsules to allow for persistent noninvasive monitoring of the transplanted microcapsules. As proof of concept, we demonstrated *in vivo* delivery of custom made imaging-visible microcapsules in a preclinical study involving X-ray-guided transarterial chemoembolization (TACE) in pigs.

#### 2.1.1 X-ray-guided transarterial chemoembolization (TACE)

TACE involves the delivery of embolic capsules along with chemotherapeutic agents into targeted blood vessels to occlude arteries that feed tumors. The technique provides a minimally invasive method to starve tumors of oxygen and nutrients. It also allows high doses of chemotherapeutics to be administered in a localized region without resulting in systemic toxicities (1). However, current clinical formulations of embolic capsules are

not readily visible directly conventional imaging techniques such as X-ray. Thus, the location of the embolic capsules can only be inferred from repeated delivery of contrast solutions to the region of interest followed by qualitative assessments of the extent of the occlusion. After delivery, the contrast soon washes out, leaving only radiolucent embolics behind. As a result, the risk of embolic agents being delivered to the wrong portion of the organ or leaking out into healthy organs is a concern. To minimize the risk of non-target embolization (NTE), physicians tend to deliver an insufficient numbers of embolic capsules, often leading to sub-optimal treatment. Because NTE or reflux may occur in 90% of TACE procedures (2), embolic capsule therapy has been primarily restricted to the treatment of tumors. While embolization is a well-accepted treatment for hepatocellular carcinoma, non-resectable metastatic disease, and renal tumors, the expansion of embolization therapy to non-oncological applications has been severely thwarted due to the consequences of NTE. For instance, in uterine fibroid embolization (UFE), which is typically performed in young women to treat leiomyomas – a benign tumoral disease affecting fertility, undertreatment, to avoid NTE, often results in the need for reintervention (3). If the risk of NTE could be mitigated, repeat UFE procedures could potentially be reduced or eliminated. Therefore, the development of imaging-visible embolic agents could expand the repertoire of image-guided, minimally invasive applications that could be performed in otherwise healthy individuals.

Commercially available preparations of embolic capsules are typically made of polyvinyl alcohol or tris-acryl gelatin (4), tend to have large polydispersity in diameter, and are difficult to label with contrast agents. For example, two of the smallest FDA-approved capsules range in size from 40 – 120  $\mu\text{m}$  to 45 – 145  $\mu\text{m}$ , or a standard deviation of

around 50% (5,6). While larger capsules have narrower distributions, the absolute size range is still around 200 – 300  $\mu\text{m}$ , making selective and consistent embolization of small vessels difficult. Microfluidic capsule preparations involving crosslinking of alginate hydrogels are able to achieve particles on the order of tens of microns, while maintaining a narrow size distribution, thereby permitting highly selective embolization. However, typical microfluidic production methods have extremely low throughput and, thus, are not commercially practical. Furthermore, instability in the microfluidic flow can also result in gelation at the device nozzles, resulting in frequent device failure (7). To address these issues, we have developed a new method of alginate microcapsule production utilizing a novel, pseudo-check valve microfluidic device, which partitions the crosslinker-containing oil and alginate streams, thus limiting the chances of inadvertent gelation at the nozzles. This enables highly scalable, robust parallel generation of the microcapsules. Furthermore, by impregnating the alginate with contrast agents, imaging-visible embolic beads (IEBs) can be prepared. The potential of this new X-ray-visible embolic agent to expand the use of particle embolics is demonstrated in otherwise healthy animals to prevent weight gain as an innovative and safe method with which to treat obesity.

### 2.1.2 Advantages of Microfluidic Preparation

A major advantage of microfluidic preparations is that the generated microcapsules are spherical, small, and uniform. While opinions differ on the importance of embolic capsule uniformity (15,26,27), spherical capsules are less likely than non-spherical particles, like PVA, to aggregate and occlude either the delivery catheter or proximal

portions of vessels (15,28). Small embolic capsules have the potential to embolize the vasculature at more distal branches (11,26,27,29), thereby making repeat embolization of the same capillary bed possible by preserving access through neighboring arterial branches or better mimicking liquid sclerosis agents, but with more precise placement. However, there have also been reports of unexpected side effects, such as non-target pulmonary embolization in some patients (5,6). In current clinical practice, reflux and NTE is prevented by erring on the side of underdosing, and can lead to incomplete treatment of malignancies and uterine fibroids. Thus, the ability to visualize the capsules directly is not only convenient, but also has the potential to enable delivery of precise quantities of embolic capsules to achieve effective vessel occlusion with minimal NTE. In particular, we have demonstrated a potential new application of IEBs—embolic therapy as a treatment for obesity—using standard clinical imaging equipment and devices where NTE would be unacceptable in an otherwise healthy individual. The stability and biocompatibility of the microcapsules was high without evidence of IEB destruction or foreign body reaction in both the stomach and kidney at three to four weeks post-administration. In addition, the persistent appearance of IEBs on cone-beam CT provides a means by which to determine the durability of the treatment in a particular individual without the need for repeated arteriograms.

## 2.2 Materials and Methods

### 2.2.1 Microfluidic device fabrication

A two-layer polydimethylsiloxane (PDMS) microfluidic device was fabricated as previously described (38). Briefly, a 30- $\mu\text{m}$  positive photoresist layer (SPR 220-7,

Microchem Corp) was spin-coated onto a silicon wafer treated with hexamethyldisilazane. Valve pads were formed by exposing the resist at 5,000 mJ/cm<sup>2</sup> through a patterned photomask. After development, an SU-8 3050 negative photoresist layer was spin-coated, exposed at 350 mJ/cm<sup>2</sup>, and developed to provide 80- $\mu$ m-tall main fluidic channels. The valve control mold was fabricated on a separate wafer using SU-8 3050 photoresist under the same conditions.

A thin PDMS layer (Sylgard 184, Ellsworth Elastomers, 15:1 base-to-curing agent wt/wt ratio) was spun onto the fluidic mold, while a thicker layer (7:1 base-to-curing agent) was cast onto the valve control mold, and baked for seven and 12 minutes at 80 °C, respectively. The two layers were aligned and bonded before sealing with a glass coverslip using an oxygen plasma treatment.

### 2.2.2 Microcapsule preparation

The pseudo-check valve between the alginate and oleic acid channels was initially pressurized at 10 psi with deionized water for closure. Calcified oleic acid was prepared by dissolving calcium chloride (2 g) in ethanol (10 mL), and then, mixed with oleic acid (10 mL, Sigma-Aldrich). After 48 hours, phase separation occurred, and the ethanol-rich top phase was removed and calcified oleic acid was diluted 10-fold with oleic acid to give the final working calcified oil, which was introduced into the device at 20 psi. Next, alginate (1 wt%, Pronoval UP LVG, FMC Biopolymer) was prepared in natural saline (0.9% sodium chloride) and delivered into the device at 25 psi. Last, the crosslinking solution was prepared by mixing IPA with a 20 wt% aqueous calcium chloride solution (2:1 v/v), and introduced near the outlet at 5 psi. The generated microcapsules were

collected from the chip by pipetting the mixture from the outlet of the device and stored at 4 °C. Microcapsules were rinsed with natural saline before use.

### 2.2.3 Contrast agent capsule impregnation

Barium sulfate (Sigma-Aldrich) suspended in PBS was sonicated for 15 minutes (Microson Cell Disruptor XL) to disrupt clumps of crystals to minimize device nozzle clogging. The suspension was mixed with alginate to yield a 10 wt% barium sulfate solution in 1 wt% alginate. This barium sulfate-alginate solution was then introduced into one channel of the microfluidic device, ultimately resulting in the formation of IEBs.

### 2.2.4 Microcapsule characterization

Environmental scanning electron microscopy (FEI Quanta ESEM 200 microscope) of capsules was performed at 5 °C and 800 Pa. Microcapsule stability at 37 °C in PBS, 100% serum, or 10% serum was determined based on measured microscopic diameter using an optical microscope (ImageJ, n=150 capsules) after 0, 7, 14, 21 and 28 days. Microcapsules stored in IPA/calcium buffer at 4 °C were evaluated at 18 months for changes in size. The permeability of the microcapsules was analyzed by incubating microcapsules with fluorescently labeled lectins of different sizes (36, 75, 120, and 150 kD) for 72 hours. After 72 hours, the microcapsules are rinsed with PBS, allowed to settle for 15 minutes, and then repeated the rinse for three times before imaging (37). IEBs used in animal studies were prepared under aseptic conditions using ethylene oxide-sterilized microdevices and filtered solutions. The sterility of the IEBs for *in vivo* studies were determined using the Endosafe®-PTS Reader and integrated software system



(Charles River Laboratories) using 005 EU/ml Endosafe®-PTS cartridges. IEB aliquots were tested for contamination.

#### 2.2.5 IEB radiopacity

The sensitivity of IEB detection was determined *in vitro*. Microcentrifuge tubes loaded with saline, oil, different volumes of IEBs, and different concentrations of iodinated contrast agent (iohexol, GE Healthcare) were imaged on a clinical fluoroscopy system (Axiom Artis, Siemens). Digital radiographs (48 cm intensifier size, 72 kV, and 62 mA) and a cone beam computed tomography (CBCT, 20s DR-Head DynaCT, Siemens Axiom Artis, 20 s rotation, 0.4° increments, 217° rotation, and 543 projections) were acquired to determine IEB visibility relative to iodinated contrast agents. A second phantom was created using a 96-well plate with serial iohexol dilutions in PBS (n = 5), serial IEB dilutions suspended in agarose (Type VII, Sigma Aldrich, n = 5), and serial unlabeled capsule dilutions suspended in agarose (n = 5). One well contained normal saline, and one well contained mineral oil. The phantom was imaged on a clinical, dual-energy computed tomography system (SONMATOM Definition Flash, Siemens, 0.5 mm slice thickness, 17.7 cm<sup>2</sup> field-of-view, 512 × 512 image matrix, 80 keV/211 mAs and 140 keV/109 mAs energy levels).

#### 2.2.6 *In vivo* studies

All protocols were approved by the Institutional Animal Care and Use Committee at the Johns Hopkins University School of Medicine. Female Yorkshire pigs (25 – 30 kgs) were fasted overnight prior to any anesthetic induction. Animals were sedated with an

intramuscular injection of tiletamine/zolazepam (100 mg/ml telazol), ketamine (100 mg/ml), and xylazine (100 mg/ml) at a dose of 1 ml/50 lbs body weight, induced with intravenous propofol, intubated, and placed on general inhalational anesthesia (isoflurane). Under ultrasound guidance, a 5 Fr introducer was placed in the femoral artery. Blood was then obtained for serum chemistries and a complete blood count.

### 2.2.7 Renal embolization

To optimize the handling characteristics and visibility of IEBs relative to conventional embolic capsules, six pigs (n = 4 acute study; n = 2 chronic study) were subjected to selective renal artery embolization under X-ray fluoroscopy and general anesthesia. A cone beam computed tomography (CBCT, DynaCT, Siemens Axiom Artis or Artis Zee, 8 s digital subtraction angiogram [DSA], 48 cm field size, 0.5 degrees/step, 210 degree rotation, 94 kV, and 475 mA) was obtained during renal artery injection of iodinated contrast (5 cc/s for 12 s of iohexol, Omnipaque, GE Healthcare). Then, a 5 Fr high-flow angiographic catheter (SOS Omni Selective Catheter, Angiodynamics) was used to select either the left or right kidney. A DSA (63 kV, 320 mA, 3 frames/s, 32 cm field size, and manual iohexol injection) was then acquired of the selected kidney. A microcatheter (Renegade Hi-Flo, Boston Scientific Corp.) was then advanced over a 0.016-inch steerable wire (Fathom, Boston Scientific Corp.) into either the inferior or superior pole of the kidney using the DSA roadmap. A DSA was then obtained of the selected kidney pole. IEBs (0.1 ml) were then injected (without iodinated contrast) into the microcatheter during direct fluoroscopic visualization (e.g., DSA). Persistence of the IEBs was evaluated on radiographs and CBCT without contrast. In acute studies, after flushing the

microcatheter outside the body, it was repositioned in the contralateral kidney. A DSA was acquired and the microcatheter was advanced into the selected kidney pole and conventional embolic capsules (Embozene, 300 – 500  $\mu\text{m}$ , Merit Medical), mixed with iohexol were injected under direct fluoroscopic visualization until stasis was achieved. The catheters were then removed, and, using a pigtail catheter in the aorta at the level of the renal arteries, a DSA CBCT was obtained of both kidneys.

For chronic studies, only IEBs were administered, followed by a CBCT without contrast, and a DSA. The introducer was removed, and the animal was allowed to recover. Repeat CBCTs without iodinated contrast injections were obtained at approximately weekly intervals in the animals under general anesthesia for three weeks post-embolization. Routine blood work was also repeated at each imaging session. At the final imaging study, an aortic DSA and DSA-CBCT were obtained. The animal was then humanely euthanized and the kidneys and highly perfused organs were harvested for gross and histopathological examination.

#### 2.2.8 Gastric fundus embolization

As a novel treatment for obesity where NTE would be unacceptable (11), BAE was performed in anesthetized normal Yorkshire pigs (n = 3 acute; n = 4 chronic) using sterile technique. Under X-ray fluoroscopic guidance, a 5 Fr angiographic guide catheter (Mickelson, Angiodynamics) was advanced over a guide wire into the abdominal aorta to select the celiac axis and obtain a pre-embolization DSA to identify the vessels feeding the gastric fundus (Fig. 2-6A). A microcatheter (Renegade Hi-Flo, Boston Scientific Corp or Surefire™ Infusion System, SureFire Inc.) was advanced over a 0.016-inch wire

(Fathom, Boston Scientific Corp.) into the fundal branches of the gastric artery. A DSA of each of the selected vessels was then obtained, followed by a CBCT during a 25% iohexol injection using parameters similar to those of renal CBCT. If, at the appropriate location, IEB embolization (0.05 – 0.1 ml) was performed during direct fluoroscopic visualization, a post-embolization CBCT without contrast was obtained. The microcatheter was then removed and flushed outside the body and repositioned to perform IEB embolization in one to two additional fundal arterial branches. Three of seven animals were humanely euthanized acutely after the BAE procedure; four animals survived for four weeks. In the chronic studies, proton pump inhibitors (40 mg omeprazole PO) were administered starting 72 hours prior to embolization. Upper gastrointestinal endoscopy was performed at one-week post-embolization in anesthetized animals. At four weeks post-embolization, a non-contrast CBCT was obtained followed by a contrast-enhanced CBCT. The animal was then humanely euthanized and the stomach, spleen, pancreas, kidney, and liver were assessed by gross and histopathology. Paraffin-embedded tissue blocks were scanned with CBCT to determine the distribution of IEBs prior to sectioning in the chronic animals.

#### 2.2.9 Weight, blood collection and hormonal analysis

Following the procedure, animals were housed in individual units and resumed their normal swine pellet diet 2.3 kcal/gram (Teklad Miniswine Diet 8753, Harlan Laboratories) given twice a day. At baseline and weekly intervals for four weeks following the procedure, pigs were sedated using the aforementioned protocol and body weight of each animal was measured. At the same time points, 5mL whole blood was

collected from a peripheral ear vein into EDTA-coated vacutainer tubes and 3mL was transferred into a separate tube containing 30 µl DPP-IV inhibitor (10 µl/mL blood, Millipore DPP4-010) and 58 µl Aprotinin (500KIU, Sigma A3428). Samples were maintained on ice until centrifuged at 3500 rpm for 10 min at 4°C and supernatant serum was stored at -80°C until processed using standard immunoassay kits. Total ghrelin was measured using radioimmunoassay with iodine 125–labeled bioactive ghrelin as the tracer and a rabbit polyclonal antibody (Phoenix Pharmaceuticals). GLP-1 was measured using ELISA (Phoenix Pharmaceutical).

#### 2.2.10 Endoscopy

One week post-procedure, animals were sedated and upper endoscopy was performed by a senior gastroenterology fellow. Two days prior to endoscopy pigs are fed Ensure (4 × 8 fl oz bottles, 220 cal/bottle) twice a day. An adult upper endoscope (Olympus America Inc, Center Valley, Pa or Pentax Medical, Montvale, N.J.) was advanced into the esophagus and the stomach for examination. Any obvious lesions were documented and biopsied using biopsy forceps (Boston Scientific Corp, Natick, Mass). All animals underwent protocol biopsies using the biopsy forceps, targeting each segment of the stomach separately. Normal saline solution was given IV to replace fluid loss during the procedure. At the conclusion of the endoscopic examination, the pigs were extubated and recovered from general anesthesia within 2 to 4 hours. The pigs were evaluated daily, and oral feedings with standard chow were resumed on postoperative day 1.

#### 2.2.11 Image analysis

For *in vitro* studies of IEB sensitivity, the mean Hounsfield units were determined in manually drawn regions of interest of equal area on dual-energy CT image reconstructions (Syngo Multimodality workstation, Siemens). Linear regression analyses were performed of the Hounsfield units vs. serial iodinated contrast agent or IEBs concentrations to determine the radiopacity of the IEBs. For *in vivo* studies, DSA images were reviewed on a Syngo multimodality workstation to determine the IEB visibility during injection and the evidence of reflux that resulted in NTE by two observers. Post-embolization DSAs were reviewed for the degree of truncation of the selected vessel. CBCTs were reviewed for the presence or absence of radiopacity indicative of IEBs.

#### 2.2.12 Histopathological assessment

Hematoxylin and eosin (H&E) staining was performed on the embolized organs and adjacent structures, which may have received NTE, to detect the presence, location, and integrity of IEBs and/or conventional embolic capsules, as well as to determine whether inflammation was present. Trichrome staining was performed on sections adjacent to the H&E staining to determine the degree of fibrosis of the embolized organs.

Immunohistochemical staining (mouse anti-human myeloid/histiocyte antigen, MAC387, Dako) was performed to determine whether macrophages were present to gauge the degree of foreign body reaction to the IEBs. In the chronic BAE study, immunohistochemical staining for ghrelin (clone 1ML-1D7, MAB10404, Millipore) was performed on the stomach fundus.

### 2.3 Results

### 2.3.1 Operation of microfluidic device

There are five functionally distinct regions in our microfluidic device. Pseudo-check valves are actuated at 10 psi, followed by the introduction of the calcified oil (20 psi) and alginate (25 psi) through the continuous phase channel and discrete phase channels, respectively (Fig. 2-1A). The actuated polydimethylsiloxane (PDMS) membrane deforms and seals the valve pad region, preventing the crosslinker-containing oil from entering the alginate channels and causing undesired crosslinking, while permitting forward flow of the higher-pressure alginate stream (Fig. 2-1B). The two phases interact at the nozzle, in the droplet generation region, where the extruding alginate stream is side-sheared into droplets by the oil. The calcium diffuses across the oil/water interface, partially crosslinking and stabilizing the nascent microcapsules. At the crosslinking region, the microspheres are introduced into an excess of calcium, with the isopropyl alcohol (IPA) acting as the phase-transfer agent (Fig. 2-1C). Capsules are then collected at the outlet and stored in the alcohol-rich crosslinking solution, which also acts as a sterilizer. Using 40 parallel nozzles in a single device, with each nozzle operating at 20 – 30 Hz (for a total of around 1 kHz, movie S1), more than  $3 \times 10^6$ , or approximately 0.2 mL/hr/chip of 50  $\mu\text{m}$  capsules can be generated. Representative devices were continuously operated for two to four hours and generated about  $2 - 8 \times 10^6$  capsules or 0.1 – 0.4 mL of IEBS, depending on the capsule diameter. While the current design employs 40 parallel nozzles, further scaling-up, including the use of parallel chips, could be performed with few problems.

### 2.3.2 Properties of IEBS

By varying channel dimensions, microcapsules with diameters in the target range of 20 up to 70  $\mu\text{m}$  were synthesized consistently. Microcapsules prepared on a microfluidic device with channel dimensions of 100  $\mu\text{m}$   $\times$  100  $\mu\text{m}$ , and a nozzle cross-section of 30  $\mu\text{m}$   $\times$  30  $\mu\text{m}$  were highly uniform ( $41.5 \pm 3.5$   $\mu\text{m}$  diameter, Fig. 2-1D and Fig. 2-2A). In the case of barium sulfate-impregnated IEBs, the pinch-off process could be disturbed by barium sulfate crystals, which was added to impart radiopacity to the capsules, resulting in slightly larger and more variable capsule diameters under the same conditions ( $48.8 \pm 4.9$   $\mu\text{m}$  diameter, Fig. 2-2B). The average diameter of the microcapsules was most significantly affected by microchannel geometry, which was moderately dependent on the relative velocities and viscosities of the calcified oil and alginate solution, and weakly dependent on the absolute flow rates of the two phases. This mirrored our computational models and experimental results and expectations from previously reported findings (8-10). This lack of dependence on the flow makes it convenient to control the speed of capsule generation by adjusting the pressures of the input solutions without significantly affecting the capsule diameter.

The IEB density was significantly higher than water due to the addition of barium sulfate, which allows the capsules to be washed without centrifugation. The environmental scanning electron microscopy (ESEM) images confirmed that the barium sulfate crystals were completely contained within the gel matrix, thereby maintaining the spherical microsphere shape (Fig. 2-1E). IEBs stability was demonstrated at 37°C in serum, IPA, and PBS for 10 days (Fig. 2-2C) and for at least 18 months when stored at 4°C in the crosslinking solution with minimal clumping ( $52.3 \pm 8.6$   $\mu\text{m}$ ,  $n = 125$ ). IEBs were



permeable to lectins with molecular weights up to 75 kD, but impermeable to lectins with molecular weights of 120 kD or higher (Fig. 2-3).

### 2.3.3 Radiopacity of IEBs

IEBs were readily visualized on conventional X-ray digital subtraction angiography, cone beam computed tomography (CBCT), and multi-detector CT (MDCT). A linear relationship between radiopacity and barium-impregnated IEB concentration was demonstrated on MDCT (Fig. 2-4A). Unlabeled capsules had a radiopacity similar to agarose and water ( $13 \pm 33$  HU unlabeled capsules vs.  $11 \pm 17$  HU agarose hydrogel). CBCT was able to detect aliquots of 5  $\mu$ L of IEBs with radiopacity exceeding 10% dilutions of iohexol (Fig. 2-4B) and CT numbers approaching those of bone ( $2809 \pm 1208$  HU), whereas the appearance on X-ray fluoroscopic images of IEBs was similar to 10% dilutions of a iohexal (Fig. 2-4C-D).

### 2.3.4 Renal delivery of IEBs *in vivo*

Endotoxin assays of IEBs were negative ( $< 2.5$  EU) in all studies. Smaller IEBs, e.g.,  $\sim 30$   $\mu$ m, containing barium sulfate administered in the first two renal embolization studies, were readily visualized in one animal, but poorly visualized in another. Subsequent renal and bariatric arterial embolization (BAE) studies used 50  $\mu$ m IEBs. Real-time direct fluoroscopic visualization of IEBs was successful in all renal embolizations (Fig. 2-5A). IEB reflux occurred in one out of five animals, resulting in non-target embolization to the superior kidney pole. This demonstrates the advantage of real-time feedback of embolic capsule delivery. In the two chronic renal embolization studies, the IEBs were visualized

during delivery with fluoroscopic imaging (Fig. 2-5A) and up to three weeks post-administration on CBCT (Fig. 2-5B, yellow arrow). For comparison, commercially available non-imaging-visible Embospheres (100 – 300  $\mu\text{m}$ ) were delivered to the superior pole of the opposite kidney (Fig. 2-5B, blue arrow). CBCT scan fused with DSA (Fig. 2-5B) also shows that IEBs were able to traverse and embolize further downstream of the vasculature when compared to the commercially available Embospheres, despite being released from an equivalent location. On gross examination of the kidneys (Fig. 2-5C) and histopathology (Fig. 2-5D), the capsules were intact at three weeks post-administration with no evidence of fibrosis or inflammatory infiltrate. Renal infarction consistent with IEB embolization occurred as expected in the two chronic studies. All studies demonstrated IEBs lodged in the distal aspects of the arterial tree toward the kidney cortex (Fig. 2-5C-D).

### 2.3.5 Gastric delivery of IEBs *in vivo*

Successful embolization of one to three arteries supplying the gastric fundus was achieved using  $0.7 - 1.5 \times 10^6$  of 50  $\mu\text{m}$  IEBs with fluoroscopic visualization of the IEBs without iodinated contrast administration (Fig. 2-6A). Superficial gastric ulceration was observed in three of six BAE animals upon post-embolization endoscopic examination. In one animal, where all three fundal vessels were embolized, significant gastric ulceration occurred, resulting in diminished food intake for the first week post-embolization. All BAE pigs had retained residual chyme visible in the stomach at 1-week associated with impaired gastric emptying. There was no ulceration identified at the gastric fundus. Normal gastric mucosa without evidence of any ulceration was present in all sham

animals. All other dissected organs appeared grossly normal upon examination without evidence of injury in both BAE and sham animals.

IEBs were visible (week 1:  $655.8 \pm 568.0$  HU; week 4:  $750.2 \pm 685.8$  HU) over the course of the 4-week study (Fig. 2-6B-D), had signal intensities comparable to that of cancellous bone (center of vertebrae, week 1:  $605.6 \pm 106.2$  HU; week 4:  $507.0 \pm 98.1$  HU), and were clearly distinguishable from bulk tissue (antrum, week 1:  $87.8 \pm 58.4$  HU; week 4:  $64.4 \pm 19.7$  HU). Weight declined (Fig. 2-6E) in BAE animals at one week compared to a net gain in sham animals (BAE:  $-0.9 \pm 2.3$  lbs; sham:  $2.9 \pm 1.9$  lbs) and weight gain remained significantly impaired at 4 weeks ( $8.3 \pm 3$  lbs vs.  $13.6 \pm 2$  lbs,  $P < 0.01$ ). Relative to baseline, at 4 weeks post-administration, BAE animals had an average weight gain of  $14 \pm 7\%$  while sham animals had an average of  $21 \pm 2\%$  weight gain. Failure of BAE pigs to gain weight was moderated by decreased serum ghrelin (Fig. 2-6F,  $1226 \pm 523$  pg/ml vs.  $1706 \pm 143$  pg/ml,  $P < 0.001$ ) and increased GLP-1 (Fig. 2-6G,  $9.8 \pm 10$  pM vs.  $5.9 \pm 2$  pM,  $P < 0.001$ ) compared to sham animals. Although the IEBs were not visible grossly in the stomach, they were detected on CBCT in post-mortem sections, as well as by histopathological examination (Fig. 2-7A-C). In addition, there was no evidence of IEBs on CBCT nor was there pathology suggestive of non-target embolization to the pancreas, spleen, liver, or distal esophagus. However, ghrelin production was suppressed in the embolized fundus, based on immunohistochemistry assessment (Fig. 2-7D-I).

## 2.4 Discussion

#### 2.4.1 Rationale for Microfluidic Device Design

Droplet microfluidics focused on biomarker detection, drug screening, etc. (12) have been an active area of research for the past decade. By performing on-chip crosslinking, the technology has been extended to the generation of small therapeutic microspheres (e.g.,  $\sim 50 \mu\text{m}$ ). For alginate microcapsules, crosslinking can be achieved in a number of ways. The simplest method is to rapidly crosslink the droplets by introducing them into a calcium or barium bath as they exit the microfluidic device (13,14), which tends to yield inhomogeneous and tear-drop shaped capsules that are not ideal for embolization (14-16). At excessively high generation frequencies, these capsules may also form clumps while crossing the oil-water interface. Alternatively, crosslinking can be achieved by fusing the droplets with separately-prepared crosslinker droplets (17), direct mixing of alginate and crosslinker streams prior to droplet formation (18), or by infusing the continuous phase with gelation inducers (e.g., slowly-diffusing crosslinkers or compounds that activate crosslinker precursors) (19,20). Droplet fusion methods typically require fine-tuning of timing to ensure synchronization and are consequently fairly slow and sensitive to flow velocity fluctuations, while direct mixing is difficult to control without rapid gelation and nozzle clogging. Thus, we adopted an approach using calcified oil to induce gelation (20). Since gelation at the nozzle is essentially a competition between diffusion of calcium into the alginate, and convective flow of the alginate out of the nozzle, the slow diffusion of the calcium across the oil/water interface minimizes nozzle failure, while simultaneously ensuring microcapsule sphericity and matrix homogeneity (16,20).

Despite the various alternative approaches listed above, the preparation of significant quantities of embolic generating microdevices that are suitable for medical use has not been previously shown. From our experience, this is, in part, because the devices are prone to fail as a result of accidental gelation in the channels and at the nozzles. In conventional droplet microdevices, the droplet generation channels must be primed with the continuous phase (i.e., oil) to achieve stable droplet generation (21,22). However, residual crosslinker molecules introduced into matrix channels during priming inevitably causes gelation and clogging of said channels. In addition, the two phases must be loaded with a slow and tedious ramp-up of the pressure aided by visual feedback to reduce backflow (22). In our device, the alginate channels are isolated from the oil stream with our pseudo-check valves to allow device priming without risking alginate channel contamination. Furthermore, the solutions can be directly loaded at the desired final pressure without any ramp-up, significantly simplifying microcapsule production. The valves also protect the process from exogenous pressure shock, such as moving the device on a microscope stage for inspection, thereby improving the robustness and prolonging the duration of device operation.

In previously described conventional devices, the rate of capsule generation is typically slow (14,18-20). Because droplet generation is an inherently unstable process, involving transient undulations of the flow velocities and even backflow of the continuous phase into the discrete phase channel (7,23,24), parallelization gives rise to complex behavior that results in poor control over size distribution, and is, hence, non-trivial (25). For microcapsule matrices that involve on-chip crosslinking, this resultant errant flow pattern

also contributes to compromised device longevity. However, our valves impart high fluidic resistance that ameliorates the effects of the complex flow patterns, which is particularly pronounced when nozzles are in close proximity. This partly accounts for the relatively narrow size distribution in our preparations. The combination of straightforward sample loading, device robustness and longevity, high-throughput, and scalability make our method a practical device for microcapsule manufacturing for embolic applications.

#### 2.4.2 Imaging-visible microcapsules allow better dosing control

Although embolics are frequently used to prevent gastric bleeding, the concept of bariatric arterial embolization (BAE) as a means to treat obesity is a relatively new concept (11,30-32). While, theoretically, one might expect BAE would lead to gastric perforation due to necrosis, the high turnover rate of the gastrointestinal lining and the stomach's rich blood supply are relatively forgiving. Since organs, such as the spleen, pancreas, liver, and esophagus, share a common vascular supply with the stomach, NTE could result in significant morbidity. In fact, in a canine BAE study, Bawudun et al. found significant NTE to the liver with the use of a sclerosing agent for BAE (31). In a swine BAE model, Paxton et al. were able to prevent weight gain in swine using conventional embolic capsules, but 40 % of animals developed gastric ulceration away from the embolized area suggesting NTE occurred (11,32). Because of the lack of X-ray visibility of conventional embolic agents, none of these prior studies could directly assess the full extent of NTE except by post-mortem evaluation. Imaging-visible embolic capsules have been created by co-incubation of conventional embolic capsules with

lipiodol, an iodinated oil (33,34). However, the radiopacity was insufficient for capsule tracking on real-time fluoroscopy during delivery. In addition, lipiodol eluted from the capsules preventing long-term serial imaging of the capsule location. Thus, the radiopacity of the IEBs in our studies was sufficient for visualization during delivery, but did not cause significant artifacts on CBCT. The capsule visibility on CBCT was retained for at least one month post-administration. Nonetheless, additional studies will be required to determine longer term capsule stability *in vivo* before moving to clinical trials.

An alternate approach to prevent NTE is to utilize catheters that have anti-reflux mechanisms that prevent retrograde flow of the embolic (35,36). However, the problem of embolic agent localization would still remain unresolved, and aggressive injection of large quantities of embolic material could inadvertently send embolic material into anastomotic vessels, which are prevalent in the stomach. Thus, the combination of anti-reflux catheters and our X-ray-visible embolic agents may provide the best solution for preventing non-target embolization and under or overdosing of embolic agents. In our hands, gastric ulceration and NTE during BAE could be prevented by a variety of mechanisms: (1) An anti-reflux catheter prevented retrograde flow of the IEBs; (2) The extent of vessel occlusion could be monitored in real-time using the radiopacity of the IEBs on X-ray fluoroscopy and CBCT; and (3) Bariatric arterial embolization was limited to two of three vessels supplying the gastric fundus. Due to the remarkable flexibility of this microcapsule generation method, multiple payloads, such as other contrast agents, drugs, radiolabels, or cells, could be envisioned by premixing the material with the alginate before introduction into the microfluidic device. In case of encapsulation of

active payloads, the high viscosity of the alginate maintains a homogeneous suspension without sedimentation during the synthesis process. It is worth noting that the permeability and stability characteristics of our 50  $\mu\text{m}$  IEBs is similar to 300 – 500  $\mu\text{m}$  unlabeled alginate capsules and contrast agent-impregnated alginate microcapsules made by the traditional droplet generation method (37). However, due to the small size of the microfluidic device and high throughput production, one could envision the encapsulation of drugs or cells could be performed just prior to delivery in the X-ray angiographic suite.

#### 2.4.3 IEBs as embolic agents

Our study results demonstrate with histologic and endoscopic evidence that by embolizing the left gastric artery with an injection of contrast-infused IEBs, the flow of blood to the gastric fundus is occluded, thereby suppressing the secretion of the appetite inducing hormone ghrelin. Weight steadily declined in animals that received BAE, and at 4 weeks post-administration, BAE animals experienced markedly lesser weight gain than those who had received sham embolization. Moreover, this decrease correlated to an additional, substantial decrease in serum ghrelin levels as well as an increase in GLP-1. These results confirm the results of earlier studies, notably Arepally et. al (47) and Paxton et. Al (48), but our study differentiates itself from these authors' work in a few notable respects.

While Arepally et. al's work demonstrated the effectiveness of gastric arterial embolization, their study also encountered difficulties. Arepally et. al used morrhuate



sodium solution as a sclerosing agent, which while effective, nonetheless caused ulceration in the subjects because of its corrosiveness. Moreover, the imaging techniques used (ultra-sonography and Digital Subtraction Angiography [DSA]) provided a great level of detail, but were inadequate to precisely image the vascular anatomy to the fundus because they lacked the dimensional perspective offered by CT (47). This difficulty carried with it the attendant complication of non-target embolization and thereby additional ulceration in these embolized areas.

Paxton et. al's study was revelatory of the further possibilities offered by bariatric embolization, but was also hampered by some methodological difficulties. Although Paxton et. al's testing demonstrated the efficacy of using microbeads to embolize they nonetheless had difficulties imaging the course of treatment, likely because of their beads and the contrast being injected separately as well as their reliance on DSA to view their progress (48). As a result there was still non-target embolization, and thus, ulceration in these additional areas. Furthermore, the authors noted that they were unable to confirm their endoscopic findings because they had not also performed a histological analysis (48). Nonetheless, Paxton et. al importantly found that beads were in fact more efficacious than morrhuate sodium, showing both fewer adverse effects and a more substantial decrease in ghrelin while still confirming Arepally et. al's results.

Our study both confirmed and improved on the above authors' work by innovating a different approach to imaging the procedure. By using IEBs and imaging the target areas pre-procedure with a combination of DSA and CBCT, the target vascular anatomy was

embolized with maximum precision. Moreover, additional CBCT was performed both immediately post-procedure and on a weekly basis thereafter to confirm the accuracy of the procedure and persistence of the IEBs. Thus the treated swine were embolized safely and with exacting precision. Additionally, by performing histological analysis in addition to endoscopy, we were able to correlate our findings, confirming the marked ghrelin decrease noted above in the results.

However, the study demands more data to further substantiate our results, and therein lay the limitations of the study. Data from a larger number of subjects over a longer testing period (4-6 months) will be much more revelatory of BAE's potential as a treatment option for obesity and its adverse effects. In particular, the measurement of ghrelin, PYY and GLP-1 levels over a longer duration will elaborate on BAE's efficacy, and a longer study will conclusively demonstrate the correlation between the embolization and adverse effects, including ulceration. Nonetheless our study demonstrated BAE's efficacy and readiness for early clinical trials.

## 2.5 Conclusion

We have developed a platform based on droplet microfluidics to generate highly uniform, small microcapsules with X-ray visibility at high throughputs. These microcapsules are compatible with conventional minimally invasive imaging and delivery techniques, and are tissue compatible. We have demonstrated that IEBs are effective as embolic agents and can provide visual feedback to the physician to minimize NTE, while offering enhanced control over site-specific delivery with more distal vascular penetration.

Compared to conventional microcapsules, IEBs offer reduced microcapsule profile, superior uniformity and traceability, and better proximity to the targeted tissue. These properties are integral to the platform's translation to intracardial delivery of stem cells, which will be discussed in the next chapter.

## 2.6 Figures

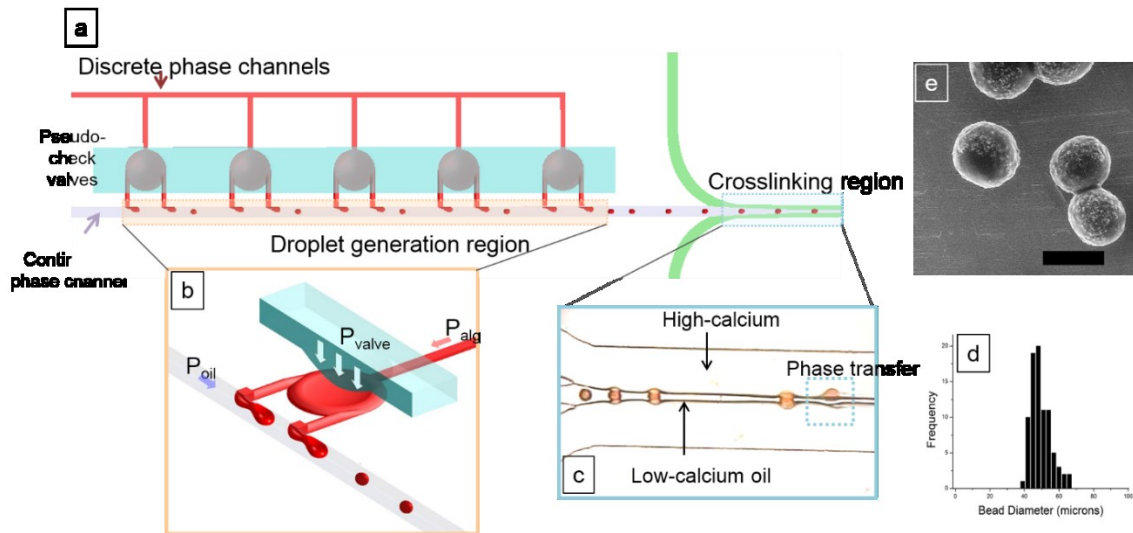


Figure 2-1: Overview of functional components of the microfluidic device.

(A) The pseudo-check valve is actuated before the continuous phase (oleic acid), discrete phase (alginate), and crosslinking solutions are loaded in that order into the device. (B) By setting alginate pressure ( $P_{alg}$ ) > valve pressure ( $P_{valve}$ ) > oil pressure ( $P_{oil}$ ), actuation deforms the PDMS membranes above the valves, which remain sealed until the alginate forces them open. The extruding alginate is side-sheared into droplets by the oncoming calcified oil stream. (C) Isopropyl alcohol (IPA) facilitates the phase transfer of nascent droplets from the middle, low-calcium oil stream to the lateral high-calcium IPA/aqueous mixture, to complete the crosslinking. (D) Histogram demonstrating that the average IEB diameter, as determined from environmental SEM (ESEM) images, is highly uniform ( $48.8 \pm 4.9 \mu\text{m}$ ,  $n = 84$ ). (E) ESEM image of imaging-visible embolic capsules (IEBs) shows that the barium sulfate crystals are fully encapsulated within the gel matrix. Bar =  $50 \mu\text{m}$ .

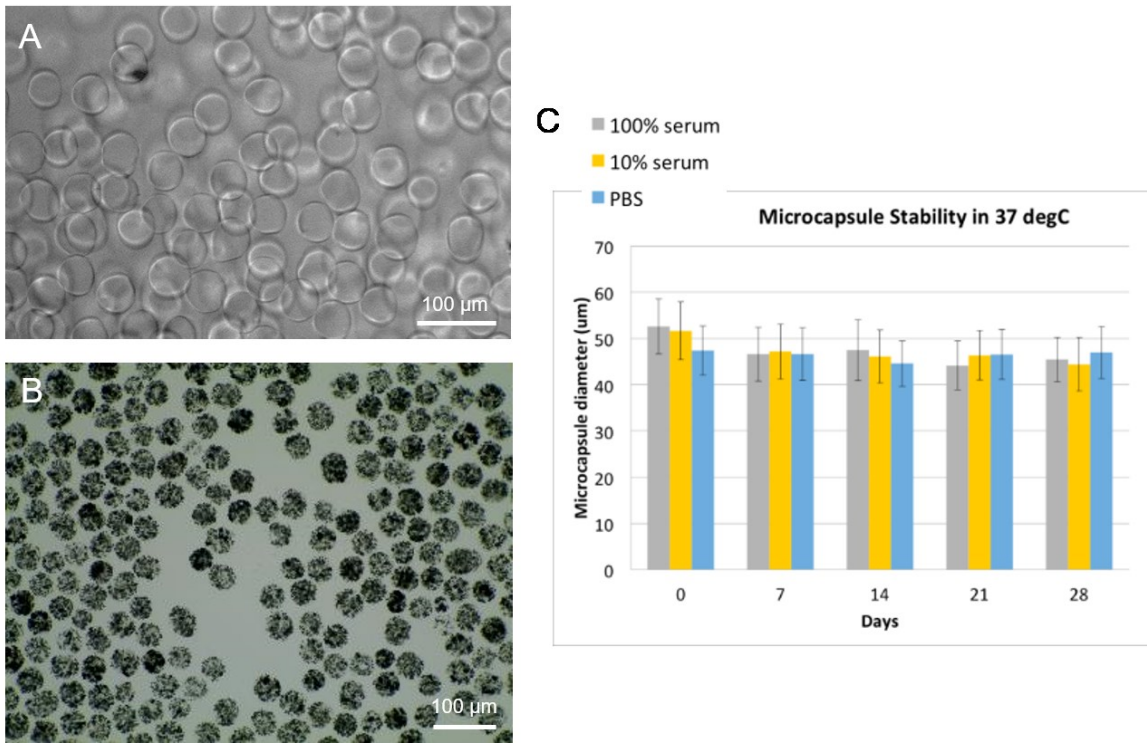


Figure 2-2: Generated Microcapsules and IEBs.

Representative phase contrast images of (A) plain alginate microcapsules and (B) IEBs showing high uniformity. (C) Alginate microcapsules incubated in physiologically-relevant conditions show no significant physical deformations.

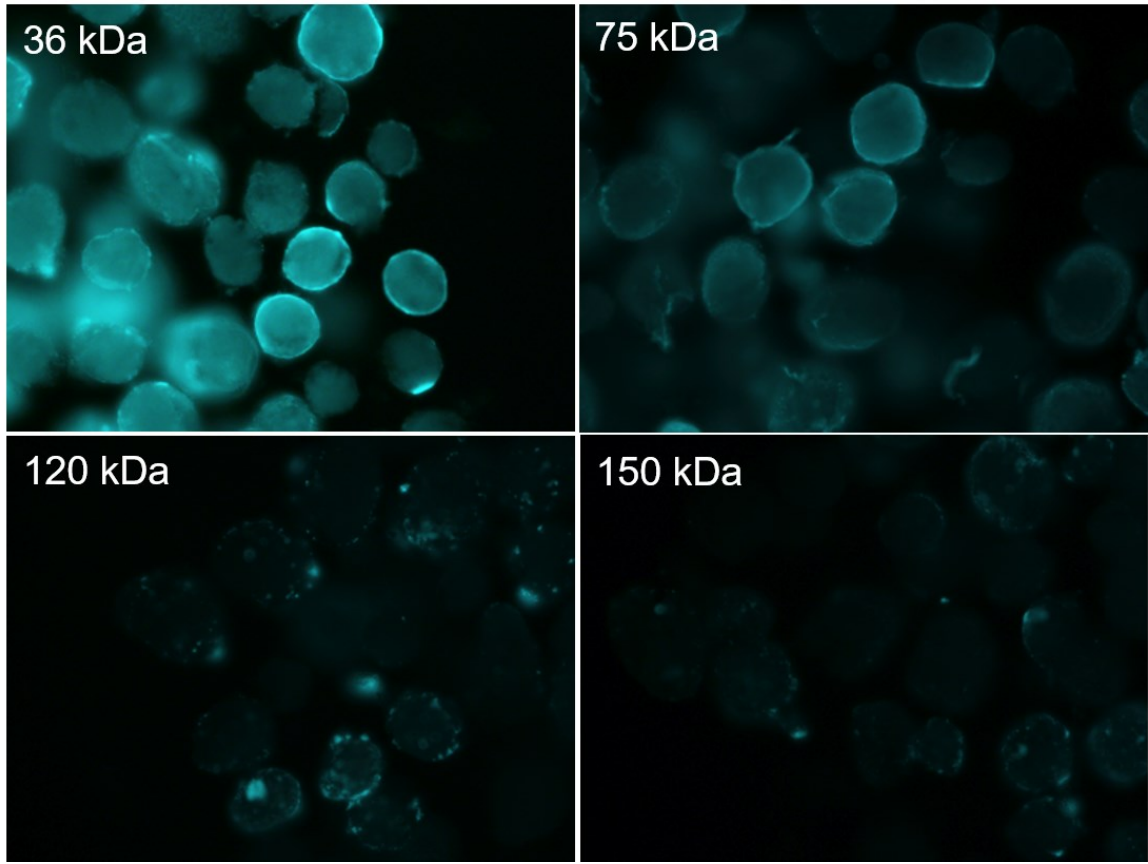


Figure 2-3: IEB permeability.

IEBs were permeable to 36 and 75 kDa (a and b, respectively), as shown by uptake of fluorescent lectins, but impermeable to 120 and 150 kDa lectins (c and d, respectively), which remain on the surface of the IEB.

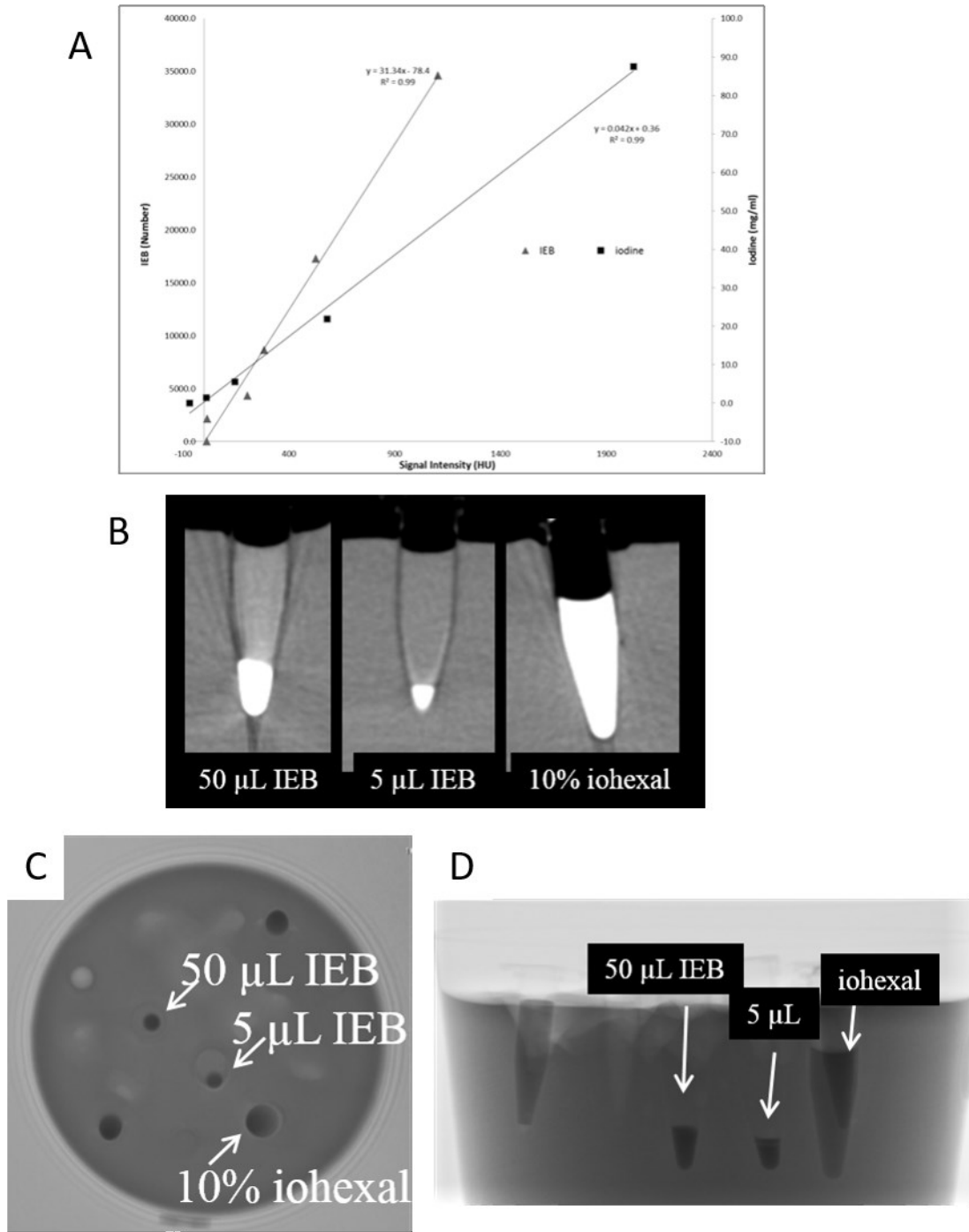


Figure 2-4: Radiopacity and x-ray sensitivity of IEBs.

(A) Graph of signal intensity (in Hounsfield units) calculated from multidetector computed tomography (MDCT) of different concentrations of iohexol or IEBs embedded in agarose with a linear regression fit. (B) Multiplanar reformat of cone beam CT (CBCT)

of aliquots of IEBs and iohexol, showing a similar radiopacity of IEBs to 10 % iohexol dilution. (C) Anterior-posterior radiograph obtained on flat-panel angiography system demonstrating the radiopacity of IEBs relative to iohexol. (D) Lateral radiograph of the same phantom shown in C.



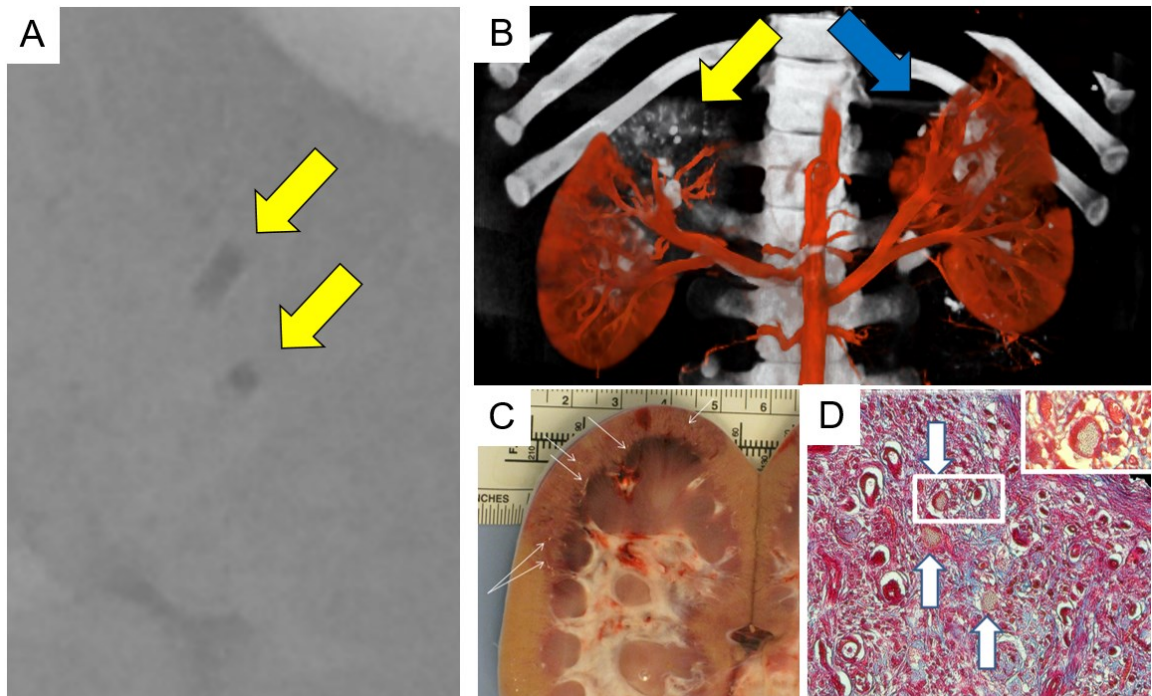


Figure 2-5: *In vivo* IEB renal delivery.

(A) Single frame from digital subtraction angiogram (DSA) during selective renal artery injection of IEBs (without iodinated contrast agent) demonstrating the ability to visualize IEB injections (arrows) in a conventional microcatheter. (B) CBCT image (white) fused with DSA of kidneys (red) to show delivered IEBs (yellow arrow) versus non-visible embospheres (blue arrow). DSA also shows deeper perfusion on the side of IEB injection (left) compared to embospheres (right). (C) IEBs were visible grossly on postmortem examination in the renal cortex (arrows). (D) Trichrome staining at three weeks post-IEB administration demonstrates the intact IEBs (arrows) with fibrosis (blue) and loss of glomeruli structure consistent with renal infarction. Little inflammatory infiltrate is observed.

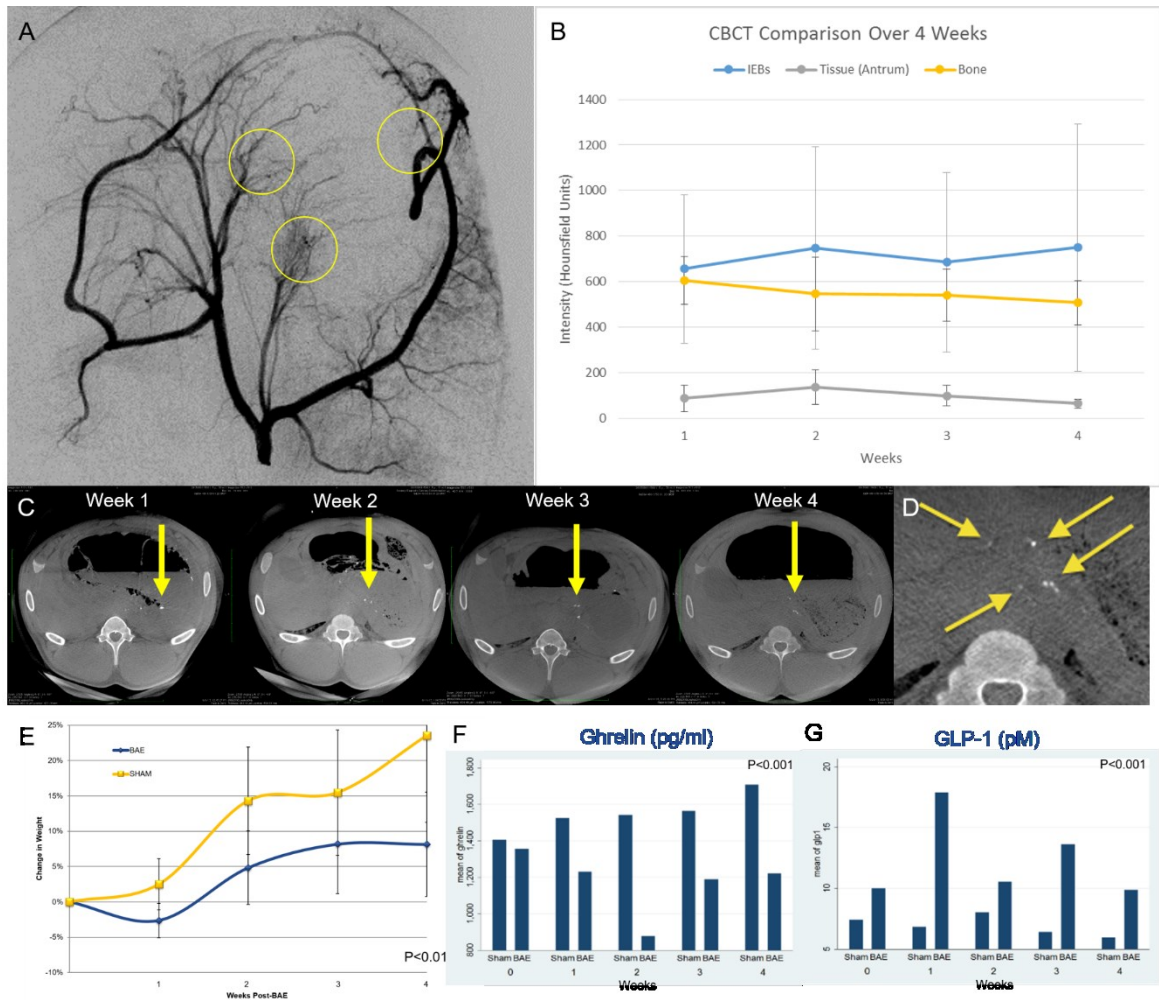


Figure 2-6: *In vivo* IEB gastric delivery.

(A) Digital subtraction angiograms (DSA) of celiac artery, showing sites of embolization (circles, from left to right: right gastric artery, left gastric artery, fundal artery). (B) Radiopacity of IEBs as compared to antrum tissue and bone (cancellous portion of vertebrae). (C) Representative CBCT axial cross sectional images showing IEB hyperintensities (arrows) over 4 weeks. (D) Enlarged CBCT axial cross section showing continued IEB visualization (arrows) at 4 weeks post-administration. (E) Average weight gain of pigs after IEB or sham treatment over 4 weeks. (F-G) Serum concentrations of (F) ghrelin and (G) GLP-1 over 4 weeks.

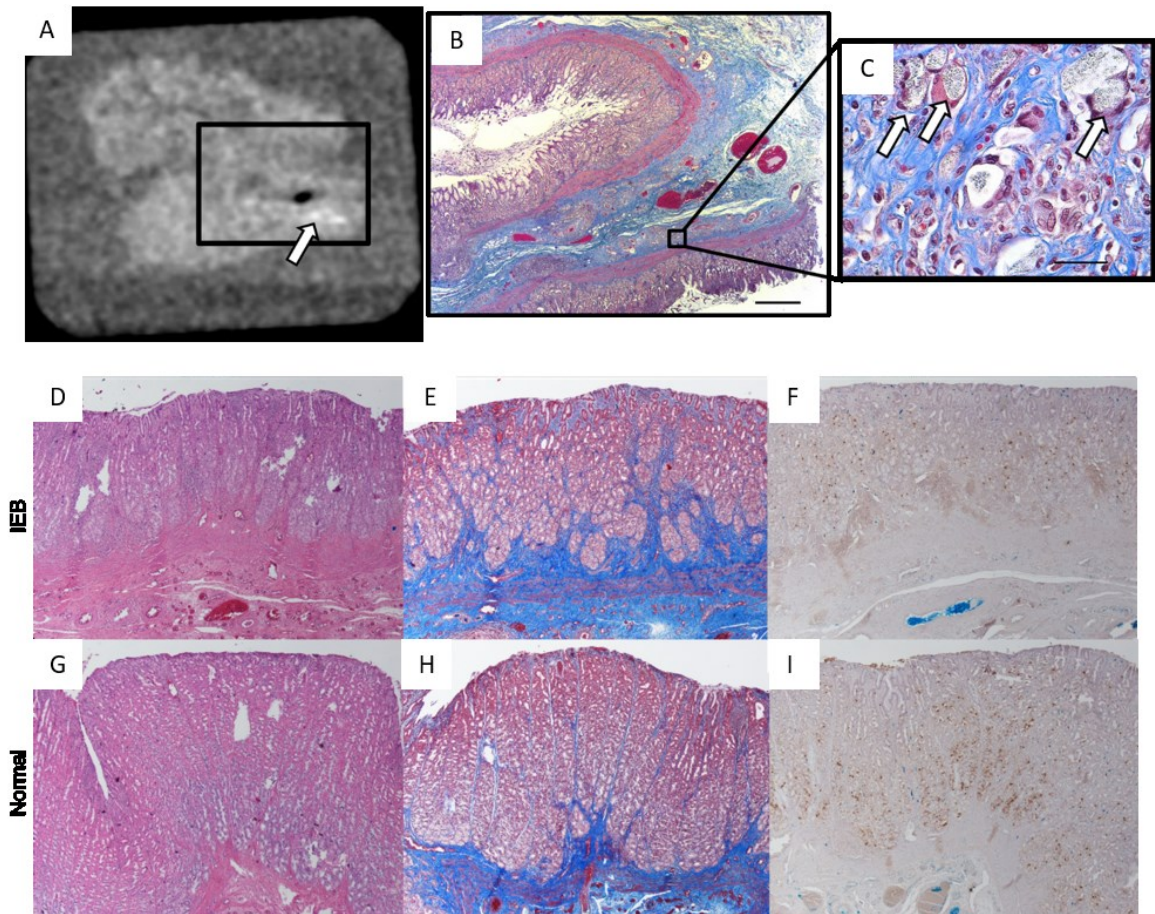


Figure 2-7: IEB gastric histopathology.

(A) Representative axial reconstruction from CBCT of paraffin-embedded fundal tissue at four weeks post-embolization with IEBs (arrow). (B) Trichrome staining demonstrating that the radiopacities (open arrow) in CBCT seen in A (yellow box) represent IEBs within vessels in the submucosal region of the tissue. (C) Magnified view (black box in B) showing IEBs remain intact. (D-I) Hematoxylin and eosin (D,G), trichrome (E,H), and anti-ghrelin (F,I) staining of fundal regions in a pig, four weeks after IEB administration, showing increased fibrosis (blue, E) and decreased ghrelin-positive cells (F) in areas containing IEBs relative to areas that were not embolized (F and I, respectively) without evidence of gastric ulceration.

## 2.7 References

1. B. Solomon, M.C. Soulen, R.A. Baum, Z.J. Haskal, R.D. Shlanksy Goldberg, C. Cope, Chemoembolization of hepatocellular carcinoma with cisplatin, doxorubicin, mitomycin-C, ethiodol, and polyvinyl alcohol: prospective evaluation of response and survival in a U.S. population. *J Vasc Interv Radiol* **10**, 793-798 (1999).
2. R. Lopez-Benitez, G.M. Richter, H. Kauczor, S. Stampfl, J. Kladeck, B.A. Radeleff, M. Neukamm, P.J. Hallsscheidt, Analysis of nontarget embolization mechanisms during embolization and chemoembolization procedures. *Cardiovasc Intervent Radiol* **32**, 615-622 (2009).
3. J. Martin, K. Bhanot, S. Athreya, Complications and Reinterventions in Uterine Artery Embolization for Symptomatic Uterine Fibroids: A Literature Review and Meta Analysis. *Cardiovasc Intervent Radiol* **36**, 395-402 (2012).
4. A. Laurent, M. Wassef, J. Namur, H. Ghegediban, J.P. Pelage. Arterial Distribution of Calibrated Tris-Acryl Gelatin and Polyvinyl Alcohol Embolization Microspheres in Sheep Uterus. *CardioVascular and Interventional Radiology* **33**, 995-1000 (2010).
5. K.T. Brown, Fatal Pulmonary Complications after Arterial Embolization with 40–120- $\mu\text{m}$  Tris-acryl Gelatin Microspheres. *J Vasc Interv Radiol* **15**, 197-200 (2004).
6. J.D. Villalta, M.D. Sorensen, J.C. Durack, R.K. Kerlan, M.L. Stoller, Selective Arterial Embolization of Angiomyolipomas: A Comparison of Smaller and Larger Embolic Agents. *The Journal of Urology* **186**, 921-927 (2011).

7. X. Li, F. Li, J. Yang, H. Kinoshita, M. Oishi, M. Oshima, Study on the mechanism of droplet formation in T-junction microchannel. *Chemical Engineering Science* **69**, 340-351 (2012).
8. J.D. Tice, H. Song, A.D. Lyon, R.F. Ismagilov, Formation of droplets and mixing in multiphase microfluidics at low values of the reynolds and the capillary numbers. *Langmuir* **19**, 9127-9133 (2003).
9. J. Wegrzyn, A. Samborski, L. Reissig, P.M. Korczyk, S. Blonski, P. Garstecki, Microfluidic architectures for efficient generation of chemistry gradations in droplets. *Microfluidics and Nanofluidics* **14**, 235-245 (2012).
10. E. Livak-Dahl, I. Sinn, M. Burns, Microfluidic Chemical Analysis Systems. *Annual Review of Chemical and Biomolecular Engineering* **2**, 325-353 (2011).
11. B.E. Paxton, C.Y. Kim, C.L. Alley, J.H.Crow, B. Balmadrid, C.G. Keith, R.J. Kankotia, S. Stinnett, A. Arepally, Bariatric embolization for suppression of the hunger hormone ghrelin in a porcine model. *Radiology* **266**, 471-479 (2013).
12. S. Teh, R. Lin, L. Hung, A.P. Lee, Droplet microfluidics. *Lab on a Chip* **8**, 198-220 (2008).
13. K. Huang, T. Lai, Y. Lin, Manipulating the generation of Ca-alginate microspheres using microfluidic channels as a carrier of gold nanoparticles. *Lab on a Chip* **6**, 954-957 (2006).
14. L. Capretto, S. Mazzitelli, C. Balestra, A. Tosi, C. Nastruzzi, Effect of the gelation process on the production of alginate microcapsules by microfluidic chip technology. *Lab on a Chip* **8**, 617-621 (2008).



15. A. Laurent, Microspheres and Nonspherical Particles for Embolization. *Techniques in Vascular and Interventional Radiology* **10**, 248-256 (2007).
16. C.K. Kuo, P.X. Ma, Ionically crosslinked alginate hydrogels as scaffolds for tissue engineering: Part 1. Structure, gelation rate and mechanical properties. *Biomaterials* **22**, 511-521 (2001).
17. L.B. Zhao, L. Pan, K. Zhang, S.S. Guo, W. Liu, Y. Wang, Y. Chen, X.Z. Zhao, H.L.W. Chan, Generation of Janus alginate hydrogel particles with magnetic anisotropy for cell encapsulation. *Lab on a Chip* **9**, 2981-2986 (2009).
18. C. Choi, J. Jung, Y.W. Rhee, D. Kim, S. Shim, C. Lee, Generation of monodisperse alginate microcapsules and *in situ* encapsulation of cell in microfluidic device. *Biomedical Microdevices* **9**, 855-862 (2007).
19. W.H. Tan, S. Takeuchi, Monodisperse Alginate Hydrogel Microcapsules for Cell Encapsulation. *Advanced Materials* **19**, 2696-2701 (2007).
20. C. Kim, K.S. Lee, Y.E. Kim, K. Lee, S.H. Lee, T.S. Kim, J.Y. Kang, Rapid exchange of oil-phase in microencapsulation chip to enhance cell viability. *Lab on a Chip* **9**, 1294-1297 (2009).
21. G.F. Christopher, S.L. Anna, Microfluidic methods for generating continuous droplet streams. *Journal of Physics D: Applied Physics* **40**, R319 (2007).
22. R. Lin, S. Teh, A.P. Lee, *Methods in Bioengineering: Biomicrofabrication and Biomicrofluidics* (ed J.D. Zahn) Ch. 10, (Artech House, Incorporated, 2009).

23. Y. Tan, V. Cristini, A.P. Lee, Monodispersed microfluidic droplet generation by shear focusing microfluidic device. *Sensors and Actuators B: Chemical* **114**, 350-356 (2006).
24. E. Amici, G. Tetradis-Meris, C.P. de Torres, F. Jousse, Alginate gelation in microfluidic channels. *Food Hydrocolloids* **22**, 97-104 (2008).
25. V. Barbier, H. Willaime, P. Tabeling, F. Jousse, Producing droplets in parallel microfluidic systems. *Physical Review E* **74**, 046306 (2006).
26. D. Carugo, L. Capretto, S. Willis, A.L. Lewis, D. Grey, M. Hill, X. Zhang, A microfluidic device for the characterisation of embolisation with polyvinyl alcohol capsules through biomimetic bifurcations. *Biomedical Microdevices* **14**, 153-163 (2012).
27. A. Laurent, E. Velzenberger, M. Wassef, J.P. Pelage, A.L. Lewis, Do Microspheres with Narrow or Standard Size Distributions Localize Differently in Vasculature? An Experimental Study in Sheep Kidney and Uterus. *J Vasc Interv Radiol* **19**, 1733-1739 (2008).
28. I. Repa, G.P. Moradian, L.P. Dehner, S.M. Tadavarthi, D.W. Hunter, W.R. Castaneda-Zuniga, G.B. Wright, H. Katkov, P. Johnson, B. Chrenka, Mortalities associated with use of a commercial suspension of polyvinyl alcohol. *Radiology* **170**, 395-399 (1989).
29. V. Verret, S.H. Ghegediban, M. Wassef, J.P. Pelage, J. Golzarian, A. Laurent, The Arterial Distribution of Embozene and Embosphere Microspheres in Sheep Kidney and Uterus Embolization Models. *J Vasc Interv Radiol* **22**, 220-228 (2011).

30. A. Arepally, B.P. Barnett, T.T. Patel, V. Howland, R.C. Boston, D.L. Kraitchman, A.A. Malayeri, Catheter-directed gastric artery chemical embolization suppresses systemic ghrelin levels in porcine model. *Radiology* **249**, 127-133 (2008).
31. D. Bawudun, Y. Xing, W. Liu, Y. Huang, W. Ren, M. Ma, X. Xu, G. Teng, Ghrelin suppression and fat loss after left gastric artery embolization in canine model. *Cardiovasc Intervent Radiol* **35**, 1460-1466 (2012).
32. B.E. Paxton, C.L. Alley, J.H. Crow, J. Burchette, C.R. Weiss, D.L. Kraitchman, A. Arepally, C.Y. Kim, Histopathologic and Immunohistochemical Sequelae of Bariatric Embolization in a Porcine Model. *J Vasc Interv Radiol* **25**, 455-461 (2014).
33. M.R. Dreher, K.V. Sharma, D.L. Woods, G. Reddy, Y. Tang, W.F. Pritchard, O.A. Chiesa, J.W. Karanian, J.A. Esparza, D. Donahue, E.B. Levy, S.L. Willis, A.L. Lewis, B.J. Wood, Radiopaque drug-eluting capsules for transcatheter embolotherapy: experimental study of drug penetration and coverage in swine. *J Vasc Interv Radiol* **23**, 257-264.e4 (2012).
34. K.V. Sharma, M.R. Drehner, Y. Tand, W. Pritchard, O.A. Chiesa, J. Karanian, J. Peregoy, B. Orandi, D. Woods, D. Donahue, J. Esparza, G. Jones, S.L. Willis, A.L. Lewis, B.J. Wood, Development of "imageable" capsules for transcatheter embolotherapy. *J Vasc Interv Radiol* **21**, 865-876 (2010).
35. S.C. Rose, S.G. Kikolski, J.E. Chomas, Downstream Hepatic Arterial Blood Pressure Changes Caused by Deployment of the Surefire AntiReflux Expandable Tip. *Cardiovasc Intervent Radiol* **36**, 1262-1269 (2012).



36. A. Arepally, J. Chomas, D. Kraitchman, K. Hong, Quantification and reduction of reflux during embolotherapy using an antireflux catheter and tantalum microspheres: ex vivo analysis. *J Vasc Interv Radiol* **24**, 575-580 (2013).
37. B.P. Barnett, A. Arepally, P.V. Karmarkar, D. Qian, W.D. Gilson, P. Walczak, V. Howland, L. Lawler, C. Lauzon, M. Stuber, D.L. Kraitchman, J.W.M. Bulte, Magnetic resonance-guided, real-time targeted delivery and imaging of magnetocapsules immunoprotecting pancreatic islet cells. *Nat Med* **13**, 986-991 (2007).
38. M.A. Unger, H. Chou, T. Thorsen, A. Scherer, S.R. Quake, Monolithic Microfabricated Valves and Pumps by Multilayer Soft Lithography. *Science* **288**, 113-116 (2000).
39. C.A. Steginsky, J.M. Beale, H.G. Floss, R.M. Mayer, Structural determination of alginic acid and the effects of calcium binding as determined by high-field n.m.r. *Carbohydrate Research* **225**, 11-26 (1992).
40. H. Gu, M.H.G. Duits, F. Mugele, Droplets formation and merging in two-phase flow microfluidics. *International Journal of Molecular Sciences* **12**, 2572-2597 (2011).
41. J.D. Tice, A.D. Lyon, R.F. Ismagilov, Effects of viscosity on droplet formation and mixing in microfluidic channels. *Analytica Chimica Acta* **507**, 73-77 (2004).
42. J.D. Tice, H. Song, A.D. Lyon, R.F. Ismagilov, Formation of droplets and mixing in multiphase microfluidics at low values of the reynolds and the capillary numbers. *Langmuir* **19**, 9127-9133 (2003).

43. P. Garstecki, M.J. Fuerstman, H.A. Stone, G.M. Whitesides, Formation of droplets and bubbles in a microfluidic T-junction-scaling and mechanism of break-up. *Lab on a Chip* **6**, 437-446 (2006).
44. M. De Menech, P. Garstecki, F. Jousse, H.A. Stone, Transition from squeezing to dripping in a microfluidic T-shaped junction. *Journal of Fluid Mechanics* **595**, 141-161 (2008).
45. H. Liu, Y. Zhang, Droplet formation in a T-shaped microfluidic junction. *Journal of Applied Physics* **106**, 034906-034908 (2009).
46. G.F. Christopher, S.L. Anna, Microfluidic methods for generating continuous droplet streams. *Journal of Physics D: Applied Physics* **40**, R319 (2007).
47. A. Arepally, B.P. Barnett, E. Montgomery, T.H. Patel, Catheter-directed Gastric Artery Chemical Embolization for Modulation of Systemic Ghrelin Levels in a Porcine Model: Initial Experience. *Radiology* **244**:1, 138-143 (2007).
48. B.E. Paxton, C.Y. Kim, C.L. Alley, J.H. Crow, B. Balmadrid, C.G. Keith, R.J. Kankotia, S. Stinnett, A. Arepally, Bariatric Embolization for Suppression of the Hunger Hormone Ghrelin in a Porcine Model. *Radiology* **266**:2, 471-479 (2013).

## **Chapter 3 Microencapsulation of Human Mesenchymal Stem Cells and Perfluorooctyl Bromide Imaging Agent in Uniform Alginate Microcapsules using Droplet Microfluidics**

### 3.1 Introduction

Stem cells have emerged as a key element of regenerative medicine therapies due to their inherent ability to differentiate into a variety of cell phenotypes, thereby providing numerous potential cell therapies to treat an array of degenerative diseases and traumatic injuries (1). A recent paradigm shift has emerged suggesting that the beneficial effects of stem cells may not be restricted to cell restoration alone, but also due to their transient paracrine actions. Stem cells can secrete potent combinations of trophic factors that modulate the molecular composition of the environment to evoke responses from resident cells. Based on this insight, current research directions include efforts to elucidate, augment and harness stem cell paracrine mechanisms for tissue regeneration.

Despite many studies having demonstrated ways to controllably induce desired paracrine secretion *in vitro*, direct transplantation of stem cells into diseased tissues has met with many challenges (2). Among them are significantly lower survival rates, ineffective therapeutic activity, and difficulty in visualizing transplanted cells. In 1964, T.M.S. Chang (3) proposed the idea of using ultrathin polymer membrane microcapsules for the immunoprotection of transplanted cells and introduced the term 'artificial cells' to define the concept of bioencapsulation, which was successfully implemented 20 years later to immobilize xenograft islet cells. When implanted into rats, the microencapsulated islets

corrected the diabetic state for several weeks. Since then, there has been considerable progress toward understanding the biological and technological requirements for successful transplantation of encapsulated cells in experimental animal models, including rodents and non-human primates. Bioencapsulation has provided a range of promising therapeutic treatments for diabetes, hemophilia, cancer and renal failure, among many studies. Additionally, the functional applicability of cell encapsulation in humans has also been reported in many clinical trials.

In the case of treatment of myocardial ischemia and the promotion of cardiovascular tissue repair, the delivery of relatively large and non-uniform capsules (~100–300  $\mu\text{m}$ ) fabricated by conventional methods has met many challenges. Among them are the inability to visualize and monitor transplanted cells, the larger needle or catheter required for administration (conventional catheters typically have an inner diameter of 200  $\mu\text{m}$ ), the increased risk of disrupting myocardial electrical conduction, and the potential for microvascular embolization. In order to circumvent these issues, we have employed an approach based on droplet microfluidics to control capsule geometry and reduce the risk of undesired complications.

Droplet microfluidics focused on biomarker detection, drug screening, etc. (4-12) have been an active area of research for the past decade. By performing on-chip crosslinking, the technology has been extended to the generation of small therapeutic microspheres (e.g., ~50  $\mu\text{m}$ ). For alginate microcapsules, crosslinking can be achieved in a number of ways. The simplest method is to rapidly crosslink the droplets by introducing them into a calcium or barium bath as they exit the microfluidic device (13,14), which tends to yield inhomogeneous and tear-drop shaped beads that are not ideal for vascular delivery (14-

16). At excessively high generation frequencies, these beads may also form clumps while crossing the oil-water interface. Alternatively, crosslinking can be achieved by fusing the droplets with separately-prepared crosslinker droplets (17), direct mixing of alginate and crosslinker streams prior to droplet formation (18), or by infusing the continuous phase with gelation inducers (e.g., slowly-diffusing crosslinkers or compounds that activate crosslinker precursors) (19,20). Droplet fusion methods typically require fine-tuning of timing to ensure synchronization and are consequently fairly slow and sensitive to flow velocity fluctuations, while direct mixing is difficult to control without rapid gelation and nozzle clogging. Thus, we adopted an approach using calcified oil to induce gelation (20). Since gelation at the nozzle is essentially a competition between diffusion of calcium into the alginate, and convective flow of the alginate out of the nozzle, the slow diffusion of the calcium across the oil/water interface minimizes nozzle failure, while simultaneously ensuring microcapsule sphericity and matrix homogeneity (16,20). We have previously demonstrated that highly uniform microcapsules produced by a similar microfluidics-based platform can be used as embolic agents in embolic therapy, and is currently investigated in a preclinical study as a treatment for obesity. Here we report a modified microfluidics platform for the encapsulation of human mesenchymal stem cells (hMSCs) and perfluorocarbon-based imaging contrast agents, resulting in smaller, more uniform microcapsules that allow for safer, less invasive and more precise cell delivery, and are traceable using conventional clinical scanners.

## 3.2 Materials and Methods

### 3.2.1 Microfluidic device fabrication

A two-layer polydimethylsiloxane (PDMS) microfluidic device was fabricated as previously described (38). Briefly, in the fluidic layer mold, a positive 30  $\mu\text{m}$  photoresist layer (SPR 220-7, Microchem Corp) was spin-coated onto a hexamethyldisilazane-treated silicon wafer. Valve pads were formed by exposing the resist at 5,000  $\text{mJ}/\text{cm}^2$ . After development, an SU-8 3050 layer was spin-coated, exposed at 350  $\text{mJ}/\text{cm}^2$ , and developed to provide 80- $\mu\text{m}$ -tall main fluidic channels. The valve control mold was fabricated on a separate wafer using SU-8 3050 photoresist under the same conditions.

A thin PDMS layer (Sylgard 184, Ellsworth Elastomers, 15:1 base-to-curing agent wt/wt ratio) was spun onto the fluidic mold, while a thicker layer (7:1 base-to-curing agent) was cast onto the valve control mold, and baked for seven and 12 minutes at 80  $^{\circ}\text{C}$ , respectively. The two layers were aligned and bonded before sealing with a glass coverslip using an oxygen plasma treatment.

### 3.2.2 Microcapsule preparation

The pseudo-check valve between the alginate and oleic acid channels was initially pressurized at 10 psi with deionized water for closure. Calcified oleic acid was prepared by dissolving calcium chloride (2 g) in ethanol (10 mL), and then, mixed with oleic acid (10 mL, Sigma-Aldrich). After 48 hours, phase separation occurred, and the ethanol-rich top phase was removed and calcified oleic acid was diluted 10-fold with oleic acid to give the final working calcified oil, which was introduced into the device at 20 psi. Next, alginate (1 wt%, Pronoval UP LVG, FMC Biopolymer) was prepared in normal saline (0.9% NaCl) and delivered into the device at 25 psi. Last, the crosslinking solution was prepared by mixing IPA with a 20 wt% aqueous calcium chloride solution (2:1 v/v), and

introduced near the outlet at 5 psi. The generated microcapsules were collected from the chip by pipetting the mixture from the outlet of the device and stored at 4 °C. Microbeads were rinsed with PBS before use.

Microcapsules were prepared under aseptic conditions using ethylene oxide-sterilized microdevices and filtered solutions. The sterility of the microcapsules were determined using the Endosafe®-PTS Reader and integrated software system (Charles River Laboratories) using 005 EU/ml Endosafe®-PTS cartridges (data not shown).

### 3.2.3 Human mesenchymal stem cell culture and microencapsulation

Human mesenchymal stem cells was cultured using Mesenchymal Stem Cell Growth Medium BulletKit (Lonza) using manufacturer protocols in T75 Corning Falcon tissue culture treated flasks. Cells for microencapsulation were extracted at 80% confluency and mixed gently with alginate to a final concentration of roughly  $4 \times 10^6$  cells/mL. The mixture is fed through the custom microfluidic device to produce uniform microcapsules, centrifuged to remove waste and excess calcium solution, then transferred to 24-well plate with media for culture in incubator. Media is replaced twice a week for up to 4 weeks.

### 3.2.4 Cell viability

Cell viability is determined by Live/Dead staining or by AlamarBlue cell viability assay (Thermo Fisher Scientific, DAL1025). Microcapsules are incubated with 2  $\mu$ M Calcein AM (Sigma Aldrich) for 20 minutes and with 5  $\mu$ M propidium iodide (Sigma Aldrich)

for 5 minutes and imaged immediately. AlamarBlue assay was conducted according to manufacturer suggested protocols.

### 3.2.5 Contrast agent impregnation

PFOB emulsions were made ultrasonically a mixture of equal parts lecithin (Sigma Aldrich) and 1-Bromoheptadecafluorooctane while sitting on ice, as described previously. The resulting PFOB emulsion is added to ProNova ultrapure LVG alginate (Novamatrix) to a final composition of 12% PFOB emulsions and 1.5% alginate.

### 3.2.6 Microbead characterization and sterilization

To characterize the diffusion of calcium across the oil-water interface into the alginate gel, a fluorescent calcium dye (10  $\mu$ M Fluo-4, Invitrogen) was incorporated into the 1 wt% alginate solution. Fluorescent readings were then obtained as the beads traversed the microfluidic device. To calculate the concentration of free calcium, we use the formula

$$Ca_{\text{free}} = K_d \frac{F - F_{\text{min}}}{F_{\text{max}} - F}$$

Where  $K_d = 345$  nM for Fluo-4, and  $F_{\text{min}}$  and  $F_{\text{max}}$  are the fluorescence intensity measured for 10  $\mu$ M Fluo-4 in PBS with no calcium and 1 mM calcium chloride, respectively. By monitoring the fluorescence intensity, we were able to estimate the concentration of free calcium in the gel matrix. The dissociation constant of calcium-alginate depends on the composition of the calcium. The dissociation constant reported for the alginic acid L-guluronan component (poly-GluA) and D-mannuronan (poly-ManA) is  $2 \times 10^{-4}$  M and  $1 \times 10^{-3}$  M, respectively (39). For the alginate used in our microfluidic device (NovaMatrix



PRONOVA UP LVG, high-GluA), we estimated the dissociation constant to be closer to the lower end of this range at  $4 \times 10^{-4}$  M.

Fluorescence images were acquired during the bead-generation process (QImaging Intensified Retiga mounted on Olympus IX-71 Inverted Microscope, FITC fluorescence cube; Settings for the camera on QCapture software were as follow: exposure = 11.4 ms; intensifier gain = 3365; CCD gain = 10.5; and offset = 477) and processed with ImageJ (NIH, Bethesda, MD). Results of calcium uptake are described in the Supplementary Note.

To examine the dependence of bead diameter on alginate flow rate, a computational model of the droplet generation process was created using COMSOL. A two-phase flow level set model was used to investigate the relationship between droplet size and alginate flow rate in a T-junction side-shearing droplet generator. In addition, simulations were performed to determine the effect of cross channel and nozzle width on bead diameter. The simulations were compared to experiments performed in a single-nozzle microfluidic device with nozzle dimension of  $50 \times 25 \mu\text{m}$ , and an  $80 \times 80 \mu\text{m}$  cross channel while varying the alginate pressure (4-15 psi). High-speed videos (Casio Exilim EX-F1 camera) of the bead generation were analyzed (ImageJ) to determine the bead diameters, generation frequency, and flow rates of both the alginate and oleic acid.

Environmental scanning electron microscopy (FEI Quanta ESEM 200 microscope) of beads was performed at 5 °C and 800 Pa. Microbead stability at 37 °C in PBS, 100 % serum, 10 % serum, or natural saline was determined based on measured microscopic diameter using an optical microscope and shape changes (ImageJ, n=150 beads) after 0, 1, 3, 7 and 10 days. Microbeads stored in IPA/calcium buffer at 4 °C were evaluated at

18 months for changes in size. The permeability of the microcapsules was analyzed using fluorescently labeled lectins (36, 75, 120, and 150 kD) as previously described (37).

Microcapsules used in animal studies were prepared under aseptic conditions using ethylene oxide-sterilized microdevices and filtered solutions. The sterility of the microcapsules for *in vivo* studies were determined using the Endosafe®-PTS Reader and integrated software system (Charles River Laboratories) using 005 EU/ml Endosafe®-PTS cartridges. microcapsule aliquots were tested for contamination.

### 3.2.7 Microcapsule radiopacity

The sensitivity of microcapsule detection was determined *in vitro*. Microcentrifuge tubes loaded with saline, oil, different volumes of microcapsules, and different concentrations of iodinated contrast agent (iohexol, GE Healthcare) were imaged on a clinical fluoroscopy system (Axiom Artis, Siemens). Digital radiographs (48 cm intensifier size, 72 kV, and 62 mA) and a cone beam computed tomography (CBCT, 20s DR-Head DynaCT, Siemens Axiom Artis, 20 s rotation, 0.4° increments, 217° rotation, and 543 projections) were acquired to determine microcapsule visibility relative to iodinated contrast agents. A second phantom was created using a 24-well plate with serial microcapsule dilutions suspended in agarose (Type VII, Sigma Aldrich, n = 5). The phantom was imaged on a clinical, dual-energy computed tomography system (SONMATOM Definition Flash, Siemens, 0.5 mm slice thickness, 17.7 cm<sup>2</sup> field-of-view, 512 × 512 image matrix, 80 keV/211 mAs and 140 keV/109 mAs energy levels).

### 3.2.8 *In vivo* studies

All animal studies were approved by the Institutional Animal Care and Use Committee at the Johns Hopkins University School of Medicine. Female Yorkshire pigs (25 – 30 kgs) were fasted overnight prior to any anesthetic induction. Animals were sedated with an intramuscular injection of tiletamine/zolazepam (100 mg/ml telazol), ketamine (100 mg/ml), and xylazine (100 mg/ml) at a dose of 1 ml/50 lbs body weight, induced with intravenous propofol, intubated, and placed on general inhalational anesthesia (isoflurane). Blood was then obtained for serum chemistries and a complete blood count. Alginate capsules and PFOB-impregnated microcapsules are injected to the leg muscle and imaged by cone beam computed tomography (CBCT, DynaCT, Siemens Axiom Artis or Artis Zee, 8 s digital subtraction angiogram [DSA], 48 cm field size, 0.5 degrees/step, 210 degree rotation, 94 kV, and 475 mA).

### 3.2.9 Image analysis

For *in vitro* studies of microcapsule sensitivity, the mean Hounsfield units were determined in manually drawn regions of interest of equal area on dual-energy CT image reconstructions (Syngo Multimodality workstation, Siemens). Linear regression analyses were performed of the Hounsfield units vs. serial iodinated contrast agent or microcapsules concentrations to determine the radiopacity of the microcapsules. For *in vivo* studies, CBCTs were reviewed for the presence or absence of radiopacities indicative of microcapsules.

### 3.2.10 Histopathological assessment

Hematoxylin and eosin (H&E) staining was performed to detect the presence, location, and integrity of microcapsules and/or conventional embolic beads, as well as to determine whether inflammation was present. Trichrome staining was performed on sections adjacent to the H&E staining to determine the degree of fibrosis of the tissue. Immunohistochemical staining (mouse anti-human myeloid/histiocyte antigen, MAC387, Dako) was performed to determine whether macrophages were present to gauge the degree of foreign body reaction to the microcapsules.

### 3.3 Results

#### 3.3.1 Operation of microfluidic device

There are five functionally distinct regions in our microfluidic device. Pseudo-check valves are actuated at 10 psi, followed by the introduction of the calcified oil (20 psi) and alginate (25 psi) through the continuous phase channel and discrete phase channels, respectively (Fig. 3-1A). The actuated Polydimethylsiloxane (PDMS) membrane deforms and seals the valve pad region, preventing the crosslinker-containing oil from entering the alginate channels and causing undesired crosslinking, while permitting forward flow of the higher-pressure alginate stream. The two phases interact at the nozzle, in the droplet generation region, where the extruding alginate stream is side-sheared into droplets by the oil. The calcium diffuses across the oil/water interface, partially crosslinking and stabilizing the nascent microbeads. At the crosslinking region, the microspheres are introduced into an excess of calcium. Beads are then collected at the outlet and stored in the calcium-rich crosslinking solution (Fig. 3-1E-F). Using 10 parallel nozzles in a single device, with each nozzle operating at 20 – 30 Hz, more than  $1 \times 10^6$  caps/hr/chip, or

approximately 65  $\mu\text{L/hr/chip}$ , of  $\sim 50\text{-}\mu\text{m}$  microcapsules can be generated. While the current design employs 10 parallel nozzles, we have shown that designs with 40 parallel nozzles that ran for 2 – 4 hours were able to generate approximately 0.5 – 1 mL of microcapsules in one instance. Thus, we expect that further scaling-up, including the use of parallel chips, could be performed with few problems.

### 3.3.2 Microcapsule size, shape, and variability (alginate vs. hMSC vs. PFOB)

Microfluidic channel dimensions, flow velocities, and the surface tension of the primary solution are three major factors that govern capsule size, shape, and variability. Alginate microcapsules are produced at  $49.346 \pm 2.46 \mu\text{m}$ , while PFOB microcapsules are produced at  $47.32 \pm 3.98 \mu\text{m}$ , and alginate microcapsules containing hMSCs are produced at  $48.03 \pm 5.76 \mu\text{m}$  (Fig. 3-1G). The average aspect ratio of the microcapsules are  $0.91 \pm 0.07$  (alginate),  $0.92 \pm 0.07$  (PFOB), and  $0.90 \pm 0.13$  (hMSC) (Fig. 3-1H).

Due to minute differences in each custom microfluidic device, each batch of microcapsules produced have slightly different average sizes. With a target size of 50  $\mu\text{m}$ , three batches of alginate microcapsules were produced using three different microfluidic devices. Their respective average sizes were  $52.99 \pm 4.54 \mu\text{m}$ ,  $45.44 \pm 5.42 \mu\text{m}$ , and  $49.35 \pm 2.46 \mu\text{m}$  (Fig. 3-1I), and they are statistically insignificant.

### 3.3.3 Microcapsule permeability and stability

The microcapsules were incubated with fluorescently labeled lectins (36, 70, 120 and 150 kDa) to assess their permeability to molecules of corresponding sizes. Figure 3-2B shows that after a 72-hour incubation period, both plain alginate microcapsules and

PFOB-impregnated alginate microcapsules are relatively permeable to molecules  $\leq 75$  kDa, while molecules  $\geq 120$  kDa are mostly excluded. Representative images (Fig. 3-2A) shows that 36 kDa and 70 kDa lectins are uniformly distributed inside the capsules after 72 hours, whereas 120 kDa and 150 kDa lectins are only visible on the surface of the microcapsules and have almost no penetration.

To assess microcapsules stability in various conditions, microcapsules with and without PFOB were incubated in normal saline, phosphate buffered saline, 10% fetal bovine serum, and 100% fetal bovine serum and media for 2 weeks (Fig. 3-2D). No significant change in microcapsule size and morphology was observed in any of the conditions.

Additionally, high pressure flow tests indicated that alginate microcapsules were able to withstand the shear stress without significant deformation (before:  $52.99 \pm 4.54 \mu\text{m}$ ; after:  $54.00 \pm 8.10 \mu\text{m}$ ) (Fig. 3-2E).

#### 3.3.4 Viability of microencapsulated hMSC and encapsulation efficiency

Representative images showing encapsulated hMSCs in alginate microcapsules are shown in Figure 3-3A. Viability staining indicates that the encapsulated hMSCs are  $74.75 \pm 15.46 \%$  viable immediately post-encapsulation, and maintains a steady viability throughout the 10 days of the experiment, with  $74.38 \pm 12.59 \%$  viable at 10-days post-encapsulation (Fig. 3-3C). Viability was measured by calcein AM and propidium iodide staining at day-0 (immediately post-encapsulation), day-1, day-2, day-3, day-7, and day-10. There were 1.52 cells per microcapsules on day-0, and 1.55 cells per microcapsule on day-10. Some hMSC-containing microcapsules were taken after 2 days of encapsulation and liquefied with sodium citrate. The extracted hMSCs were replated in a

cell culture flask, incubated for 12 hours and stained for viability. The replated hMSCs were 100% viable and demonstrated healthy focal adhesion, cell morphology, and proliferative activity (Fig. 3-3B). When co-encapsulated with 12% PFOB, hMSCs were  $27.65 \pm 8.57$  % viable at day-0, and  $20.70 \pm 29.27$  % viable at day-10 (Fig. 3-3C).

To assess whether the cytotoxicity of the PFOB emulsions can be mitigated by delivering encapsulated cells and encapsulated imaging agents separately, PFOB emulsions and PFOB microcapsules were co-cultured with hASCs over 7 days (Fig. 3-3D). At a cell-to-microcapsule ratio of 1:2, hASCs were  $98.88 \pm 2.91$  % viable with encapsulated PFOB on day-1, compared to  $81.49 \pm 8.60$  % viable with free unencapsulated PFOB emulsions. At a ratio of 1:10, they were  $88.00 \pm 7.36$  % and  $80.31 \pm 5.26$  %, respectively. At a ratio of 1:20, they were  $82.86 \pm 4.91$  % and  $76.00 \pm 2.12$  %, respectively. At 24% PFOB emulsions, which were equivalent to the concentration cells experience when co-encapsulated with PFOB, they were  $64.76 \pm 1.25$  % viable.

### 3.3.5 *In vitro* imaging properties

PFOB microcapsules produced using the electrospraying (large microcapsules) and microfluidics methods were visualized and compared by conventional cone beam computed tomography (CBCT). PFOB-containing microcapsules were arranged in 10- $\mu$ L, 20- $\mu$ L, and 50- $\mu$ L dots (small microcapsules) and 20- $\mu$ L, 30- $\mu$ L, and 50- $\mu$ L dots (large microcapsules) and embedded in 3% agarose (Fig. 3-4A-B). The microfluidics-made (small) microcapsules demonstrated higher radiopacity (10- $\mu$ L:  $2804 \pm 154$  Hounsfield Units (HU), 20- $\mu$ L:  $2211 \pm 154$  HU, 50- $\mu$ L:  $2711 \pm 82$  HU) than electrosprayed (large) microcapsules (20- $\mu$ L:  $1469 \pm 52$  Hounsfield Units (HU), 30- $\mu$ L:

1543 ± 122 HU, 50-μL: 714 ± 66 HU). This also demonstrated that a conventional CT scanner was sensitive to as little as 10 μL or  $9.55 \times 10^4$  of our microfluidics-made PFOB microcapsules. A larger quantity of microcapsules was used to compare against natural saline (0.9% NaCl), and the oleic acid used in the microfluidic device (Fig. 3-4C-D, Air: -1023 ± 2 HU, Saline: 33 ± 38 HU, Large PFOB microcapsules: 809 ± 43 HU, Small PFOB microcapsules: 1305 ± 71 HU, oleic acid: 7 ± 24 HU). A serial dilution of small PFOB microcapsules embedded in 3% agarose between 0 - 50% was visualized to determine the relationship between capsule radiopacity and quantity (Fig. 3-4E and Fig. 3-4F, 0%: 111 ± 104 HU, 10%: 130 ± 112 HU, 20%: 139 ± 128 HU, 30%: 336 ± 145 HU, 40%: 507 ± 192 HU, 50%: 747 ± 193 HU). A linear relationship was observed at concentration greater than 20%. The radiopacity of small and large PFOB microcapsules from Fig. 3-4C was also included to show linear correlation with the serial dilution, assuming a packing density of ~74% after centrifugation.

## 3.4 Discussion

### 3.4.1 Modifications to allow cell encapsulation

In the previous chapter, we have demonstrated the ability to generate highly uniform alginate microcapsules with and without barium sulfate. The process was facilitated by the removal of the oily carrying phase solution (oleic acid) by introducing a fast flowing stream of organic solvent (isopropanol) to “pinch” the partially gelled microcapsules out of its water-in-oil emulsion and into aqueous solution. However, in the case of cell encapsulation, a high concentration organic solvent could not be used. In order to minimize the stem cells’ exposure to oleic acid and the high calcium environment, a



heparinized calcium chloride solution was used to collect the microcapsules frequently. The microcapsules then underwent a series of centrifugations and sodium chloride rinses to effectively remove the oleic acid from the solution and promptly transferred to media for culture. Empirically, this procedure improved the cells' overall viability, allowing the cells to start at a higher initial viability rate and remain high for the duration of the study.

### 3.4.2 Microcapsule permeability and stability

Semi-permeability is one of the most important property and rationale for encapsulating stem cells. We demonstrated that the microcapsules produced by this platform are relatively permeable to proteins less than 75 kDa, while molecules larger than 120 kDa are effectively excluded. This ensures the permeation of nutrients and waste, as well as important secreted therapeutic factors such as vascular endothelial growth factor (VEGF, ~34-43 kDa), interleukin-6 (IL-6, ~22-27 kDa), Angiogenin (~14.4 kDa), which are important cytokines that regulate inflammation and promote vascular repair. Critical antibodies, immunogenic proteins, and complement system activating proteins are upwards of 150kD and are filtered by the semipermeable capsule matrix. We also showed that the capsule crosslink integrity is maintained even in a non-calcified environments and in solutions containing concentrated serum proteins. Furthermore, we showed that the microcapsules are unaffected when subjected to high pressure injection through a conventional microcatheter. This ensures that the transplanted hMSCs are adequately protected by the microcapsules.

### 3.4.3 Viability of microencapsulated hMSC and encapsulation efficiency

Figure 3-3 shows that hMSCs can be encapsulated in small uniform microcapsules with consistent viability, with average viability between 71-77 % over 10 days. We believe that the viability can be improved by including cell adhesion factors and cell-friendly biomaterials such as collagen and fibrin into the microcapsule matrix. To assess whether the encapsulation process impacts the metabolic activity of the cells, we extracted the hMSCs after 2 days of encapsulation by liquefying the alginate capsule matrix. As shown in Fig. 3-3C, the replated hMSCs demonstrated growth behavior indicative of normal development, including adequate filopodia extension as well as cell division.

On the other hand, when cells are co-encapsulated with PFOB, we found that hMSC viability was consistently lower than those encapsulated in plain alginate. This may be due to the surfactants used in formulating the encapsulated PFOB emulsions having a cytotoxic effect. Thus, we have determined that co-encapsulation of stem cells with PFOB emulsions was not effaceable, and instead recommend the co-delivery of microcapsules containing hMSCs with microcapsules containing PFOB emulsions to achieve the combination effect of cell therapy and clinical visualization.

#### 3.4.4 *In vitro* imaging properties

Fig. 3-4 demonstrates that the small PFOB microcapsules produced by the microfluidics platform may offer enhanced radiopacity as well as sensitivity over the large PFOB microcapsules, possibly due to a more efficient packing volume. In Fig. 3-4A, the 10- $\mu$ L aggregation of PFOB microcapsules is clearly distinguishable over the agarose phantom, whose radiopacity is similar to that of bulk muscular tissue, in the CBCT cross section. However, the respective markers for large and small PFOB microcapsules did not follow

a linear relationship, likely due to the varied thickness and width of the markers. Figure 3-4E-F shows the radiopacity of serially diluted PFOB microcapsules in the same 3% agarose phantom. While the radiopacity of the 10% dilution falls too close to the background intensity of the agarose phantom, the intensities of the 20-50% dilutions do follow a linear relationship. From that we can extrapolate a linear regression line that correlates signal intensity with microcapsule concentration or quantity. If we assume that the small PFOB microcapsules from Fig. 3-3C have a packing density of 0.740 after being centrifuged, its radiopacity lays within reasonable range of the linear regression line extrapolated in Fig. 3-4F. These results suggest that our PFOB microcapsules will be easily visualized when transplanted *in vivo*. Furthermore, we will be able to determine the amount of microcapsules transplanted, and also be able to serially track these microcapsules noninvasively, as we have previously shown with microcapsules containing barium sulfate imaging agent. When combined with the delivery of encapsulated hMSCs, we can achieve effective paracrine-based cell therapy, while at the same time being able to visualize and trace the delivery of these microcapsules over long periods.

### 3.5 Conclusion

Our microfluidic platform enables hMSC encapsulation into highly uniform hydrogel microcapsules. The reduced microcapsule size compared to conventional encapsulation methods is amenable to delivery with commercial microcatheters, which should enable more site-specific administration into most organs for regenerative therapy. The microcapsules protects the encapsulated cells from the harmful or immunogenic large

molecules or cells, and allows adequate passage for nutrients and waste to ensure long-term survival and the release of soluble therapeutic small molecules. Furthermore, encapsulation with perfluorocarbon imaging agents allow for sensitive visualization using conventional clinical CT scanners, which will allow for more precise cell delivery with the ability of serial visualization and tracking. Consequently, this provides for a more efficient way to deliver stem cells and sustained imaging agent with decreased risk of side effects, which can potentially lead to new therapeutic strategies.

### 3.6 Figures

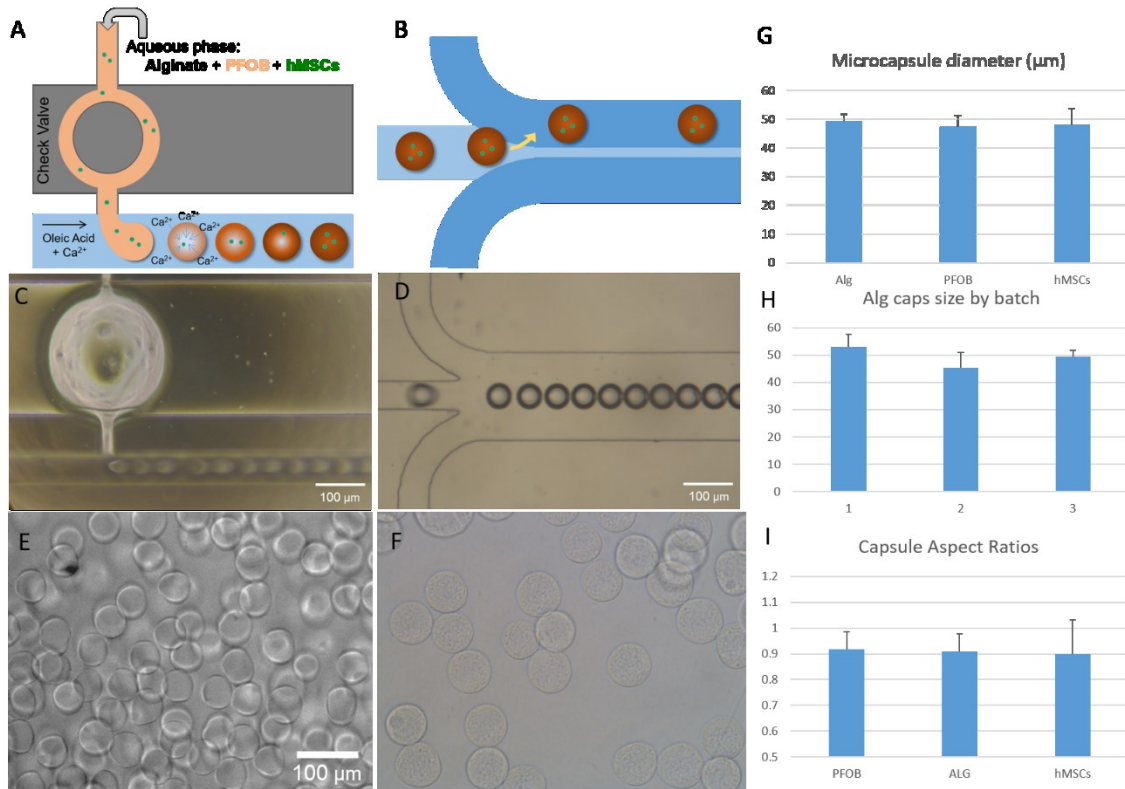


Figure 3-1: Physical characterization.

Schematic of microfluidic device at the (A) droplet formation junction and (B) device outlet showing the phase transfer of capsules into aqueous solution. Phase contrast images showing (C) the droplet formation junction and (D) device outlet without phase transferring solution to demonstrate the uniformity of the capsules. Phase contrast images of (E) alginate capsules (1.5% w/w) and (F) embedded with perfluoro-octyl bromide (PFOB, 12% w/w). (G) Typical size distribution of a single batch of alginate and PFOB-embedded microcapsules, and (H) between multiple batches. (I) Circularity of alginate and PFOB capsules. Scale bar is 100  $\mu\text{m}$ .

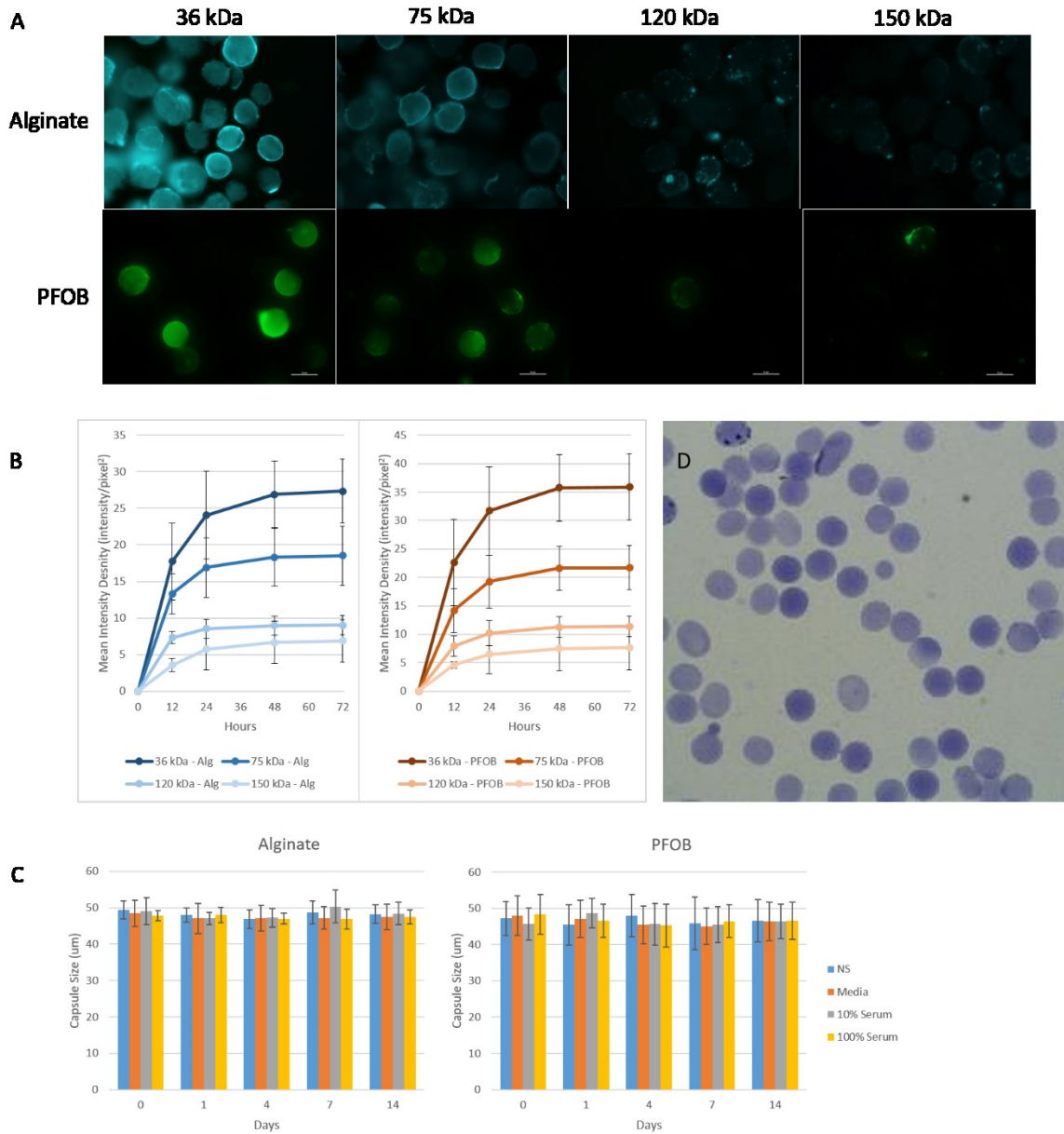


Figure 3-2: Chemical and mechanical characterization.

Fluorescence of (A) alginate microcapsules and PFOB-embedded alginate microcapsules incubated with fluorescently tagged lectin molecules of various sizes (36 kDa, 75 kDa, 120 kDa, 150 kDa) after 24 hours. (B) Mean relative fluorescence intensity quantified over 72 hours. (C) Microcapsule size stability in calcified normal saline, PBS, 10% fetal bovine serum (FBS), 100% FBS, over 14 days. (D) Representative phase contrast images

of alginate microcapsules (embedded with a blue dye) subjected to rapid injection through a 200- $\mu\text{m}$  inner-diameter microcatheter.

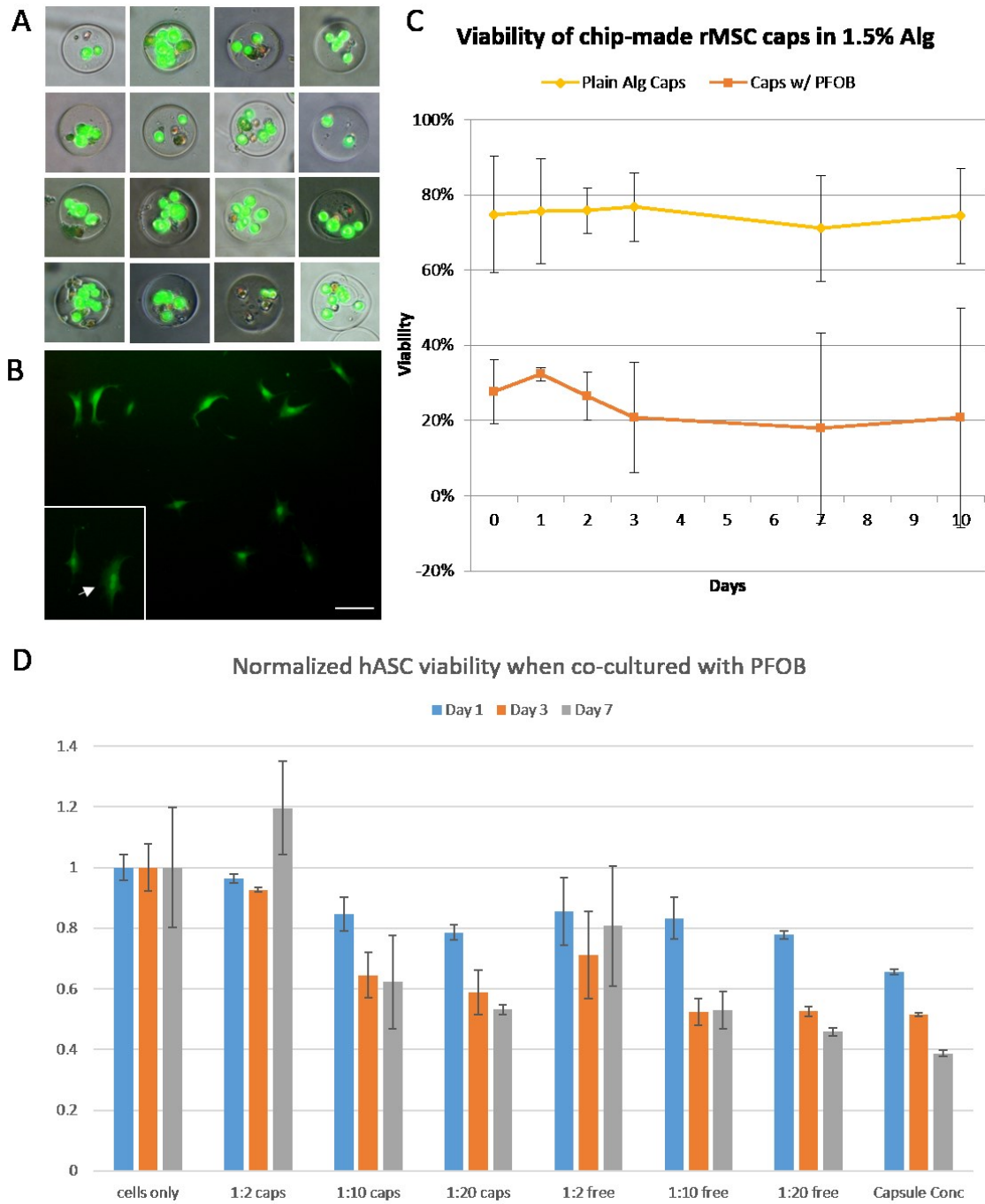


Figure 3-3: Cell encapsulation and viability.

Representative images showing (A) hMSCs in alginate microcapsules and (B) hMSCs extracted after 2 days of encapsulation and re-cultured for 12 hours. White arrows indicate cell division. Green: calcein AM. Red: propidium iodide. (C) Viability of



encapsulated MSCs with and without PFOB co-encapsulation over 10 days. (D)

AlamarBlue metabolic assay of hASC co-cultured with PFOB microcapsules and free PFOB emulsions at various concentrations.

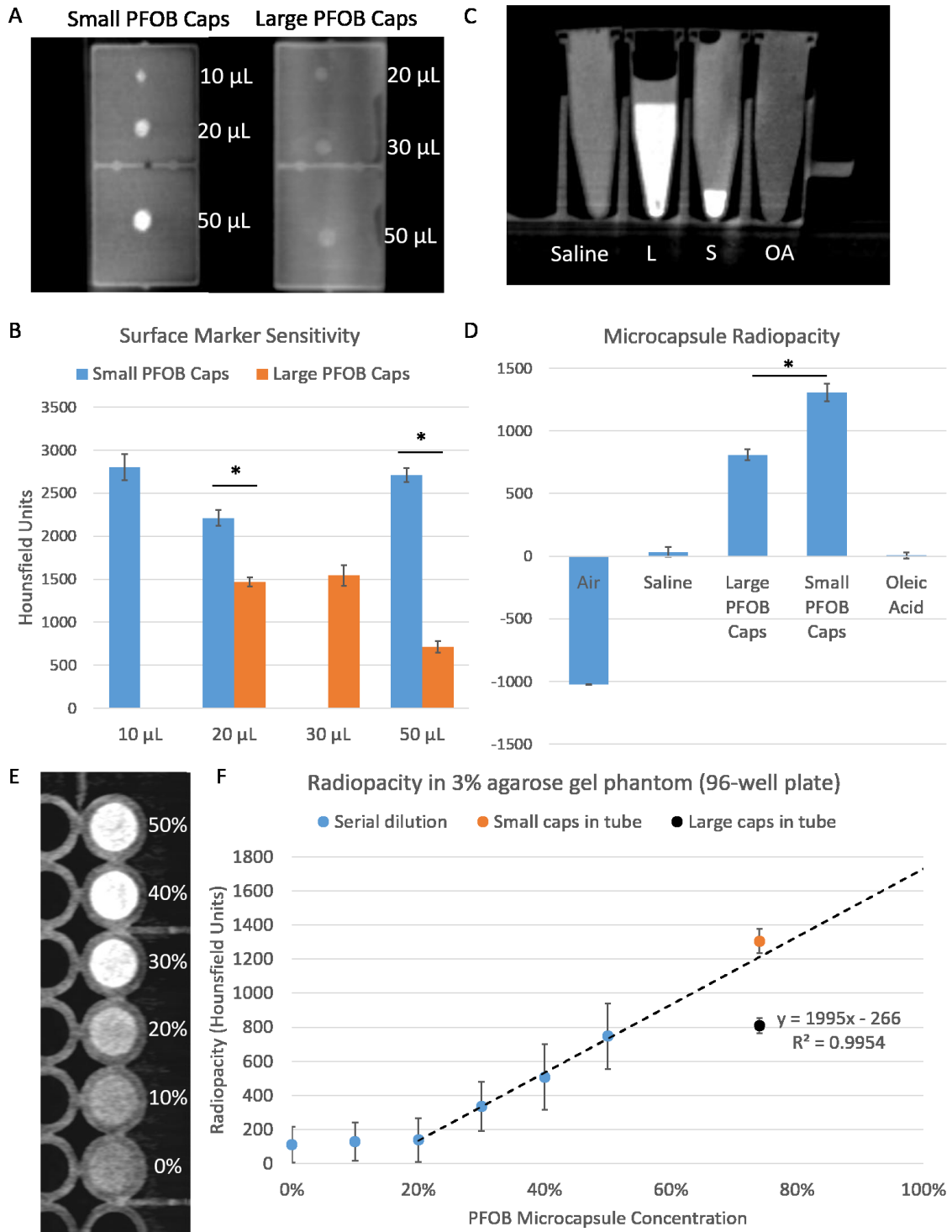


Figure 3-4: Radiopacity of PFOB microcapsules by cone beam computed tomography. (A,B) Sensitivity of electrospray-made (large) PFOB microcapsules and microfluidics-made (small) PFOB microcapsules as 10- $\mu$ L, 20- $\mu$ L, 50- $\mu$ L markers embedded in 3%

agarose. (C,D) Radiopacity of natural saline, large PFOB microcapsules, small PFOB microcapsules, and oleic acid. (E,F) Serial dilution of small PFOB microcapsules embedded in 3% agarose phantom, extrapolated to show linear relationship with the small and large PFOB microcapsules measured in (D).

### 3.7 References

1. P.R. Baraniak, T.C. McDevitt, Stem cell paracrine actions and tissue regeneration. *Regenerative Medicine* **5**(1): 121-143 (2010).
2. G. Orive, R.M. Hernandez, A.R. Gascon, R. Calafiore, T.M.S. Chang, P. De Vos, G. hortelano, D. Hunkeler, I. Lacik, A.M.J. Shapiro, J.L. Pedraz, Cell encapsulation: Promise and progress. *Nature Medicine* **9**: 104-107 (2013).
3. T.M.S. Chang, Semipermeable microcapsules. *Science*. **146**:524-525 (1964).
4. A. Laurent, M. Wassef, J. Namur, H. Ghegediban, J.P. Pelage. Arterial Distribution of Calibrated Tris-Acryl Gelatin and Polyvinyl Alcohol Embolization Microspheres in Sheep Uterus. *CardioVascular and Interventional Radiology* **33**, 995-1000 (2010).
5. K.T. Brown, Fatal Pulmonary Complications after Arterial Embolization with 40–120- $\mu\text{m}$  Tris-acryl Gelatin Microspheres. *J Vasc Interv Radiol* **15**, 197-200 (2004).
6. J.D. Villalta, M.D. Sorensen, J.C. Durack, R.K. Kerlan, M.L. Stoller, Selective Arterial Embolization of Angiomyolipomas: A Comparison of Smaller and Larger Embolic Agents. *The Journal of Urology* **186**, 921-927 (2011).
7. X. Li, F. Li, J. Yang, H. Kinoshita, M. Oishi, M. Oshima, Study on the mechanism of droplet formation in T-junction microchannel. *Chemical Engineering Science* **69**, 340-351 (2012).
8. J.D. Tice, H. Song, A.D. Lyon, R.F. Ismagilov, Formation of droplets and mixing in multiphase microfluidics at low values of the reynolds and the capillary numbers. *Langmuir* **19**, 9127-9133 (2003).

9. J. Wegrzyn, A. Samborski, L. Reissig, P.M. Korczyk, S. Blonski, P. Garstecki, Microfluidic architectures for efficient generation of chemistry gradations in droplets. *Microfluidics and Nanofluidics* **14**, 235-245 (2012).
10. E. Livak-Dahl, I. Sinn, M. Burns, Microfluidic Chemical Analysis Systems. *Annual Review of Chemical and Biomolecular Engineering* **2**, 325-353 (2011).
11. B.E. Paxton, C.Y. Kim, C.L. Alley, J.H.Crow, B. Balmadrid, C.G. Keith, R.J. Kankotia, S. Stinnett, A. Arepally, Bariatric embolization for suppression of the hunger hormone ghrelin in a porcine model. *Radiology* **266**, 471-479 (2013).
12. S. Teh, R. Lin, L. Hung, A.P. Lee, Droplet microfluidics. *Lab on a Chip* **8**, 198-220 (2008).
13. K. Huang, T. Lai, Y. Lin, Manipulating the generation of Ca-alginate microspheres using microfluidic channels as a carrier of gold nanoparticles. *Lab on a Chip* **6**, 954-957 (2006).
14. L. Capretto, S. Mazzitelli, C. Balestra, A. Tosi, C. Nastruzzi, Effect of the gelation process on the production of alginate microcapsules by microfluidic chip technology. *Lab on a Chip* **8**, 617-621 (2008).
15. A. Laurent, Microspheres and Nonspherical Particles for Embolization. *Techniques in Vascular and Interventional Radiology* **10**, 248-256 (2007).
16. C.K. Kuo, P.X. Ma, Ionically crosslinked alginate hydrogels as scaffolds for tissue engineering: Part 1. Structure, gelation rate and mechanical properties. *Biomaterials* **22**, 511-521 (2001).

17. L.B. Zhao, L. Pan, K. Zhang, S.S. Guo, W. Liu, Y. Wang, Y. Chen, X.Z. Zhao, H.L.W. Chan, Generation of Janus alginate hydrogel particles with magnetic anisotropy for cell encapsulation. *Lab on a Chip* **9**, 2981-2986 (2009).
18. C. Choi, J. Jung, Y.W. Rhee, D. Kim, S. Shim, C. Lee, Generation of monodisperse alginate microcapsules and in situ encapsulation of cell in microfluidic device. *Biomedical Microdevices* **9**, 855-862 (2007).
19. W.H. Tan, S. Takeuchi, Monodisperse Alginate Hydrogel Microbeads for Cell Encapsulation. *Advanced Materials* **19**, 2696-2701 (2007).
20. C. Kim, K.S. Lee, Y.E. Kim, K. Lee, S.H. Lee, T.S. Kim, J.Y. Kang, Rapid exchange of oil-phase in microencapsulation chip to enhance cell viability. *Lab on a Chip* **9**, 1294-1297 (2009).
21. G.F. Christopher, S.L. Anna, Microfluidic methods for generating continuous droplet streams. *Journal of Physics D: Applied Physics* **40**, R319 (2007).
22. R. Lin, S. Teh, A.P. Lee, *Methods in Bioengineering: Biomicrofabrication and Biomicrofluidics* (ed J.D. Zahn) Ch. 10, (Artech House, Incorporated, 2009).
23. Y. Tan, V. Cristini, A.P. Lee, Monodispersed microfluidic droplet generation by shear focusing microfluidic device. *Sensors and Actuators B: Chemical* **114**, 350-356 (2006).
24. E. Amici, G. Tetradis-Meris, C.P. de Torres, F. Jousse, Alginate gelation in microfluidic channels. *Food Hydrocolloids* **22**, 97-104 (2008).
25. V. Barbier, H. Willaime, P. Tabeling, F. Jousse, Producing droplets in parallel microfluidic systems. *Physical Review E* **74**, 046306 (2006).

26. D. Carugo, L. Capretto, S. Willis, A.L. Lewis, D. Grey, M. Hill, X. Zhang, A microfluidic device for the characterisation of embolisation with polyvinyl alcohol beads through biomimetic bifurcations. *Biomedical Microdevices* **14**, 153-163 (2012).
27. A. Laurent, E. Velzenberger, M. Wassef, J.P. Pelage, A.L. Lewis, Do Microspheres with Narrow or Standard Size Distributions Localize Differently in Vasculature? An Experimental Study in Sheep Kidney and Uterus. *J Vasc Interv Radiol* **19**, 1733-1739 (2008).
28. I. Repa, G.P. Moradian, L.P. Dehner, S.M. Tadavarthi, D.W. Hunter, W.R. Castaneda-Zuniga, G.B. Wright, H. Katkov, P. Johnson, B. Chrenka, Mortalities associated with use of a commercial suspension of polyvinyl alcohol. *Radiology* **170**, 395-399 (1989).
29. V. Verret, S.H. Ghegediban, M. Wassef, J.P. Pelage, J. Golzarian, A. Laurent, The Arterial Distribution of Embozene and Embosphere Microspheres in Sheep Kidney and Uterus Embolization Models. *J Vasc Interv Radiol* **22**, 220-228 (2011).
30. A. Arepally, B.P. Barnett, T.T. Patel, V. Howland, R.C. Boston, D.L. Kraitchman, A.A. Malayeri, Catheter-directed gastric artery chemical embolization suppresses systemic ghrelin levels in porcine model. *Radiology* **249**, 127-133 (2008).
31. D. Bawudun, Y. Xing, W. Liu, Y. Huang, W. Ren, M. Ma, X. Xu, G. Teng, Ghrelin suppression and fat loss after left gastric artery embolization in canine model. *Cardiovasc Intervent Radiol* **35**, 1460-1466 (2012).

32. B.E. Paxton, C.L. Alley, J.H. Crow, J. Burchette, C.R. Weiss, D.L. Kraitchman, A. Arepally, C.Y. Kim, Histopathologic and Immunohistochemical Sequelae of Bariatric Embolization in a Porcine Model. *J Vasc Interv Radiol* **25**, 455-461 (2014).
33. M.R. Dreher, K.V. Sharma, D.L. Woods, G. Reddy, Y. Tang, W.F. Pritchard, O.A. Chiesa, J.W. Karanian, J.A. Esparza, D. Donahue, E.B. Levy, S.L. Willis, A.L. Lewis, B.J. Wood, Radiopaque drug-eluting beads for transcatheter embolotherapy: experimental study of drug penetration and coverage in swine. *J Vasc Interv Radiol* **23**, 257-264.e4 (2012).
34. K.V. Sharma, M.R. Drehner, Y. Tand, W. Pritchard, O.A. Chiesa, J. Karanian, J. Peregoy, B. Orandi, D. Woods, D. Donahue, J. Esparza, G. Jones, S.L. Willis, A.L. Lewis, B.J. Wood, Development of "imageable" beads for transcatheter embolotherapy. *J Vasc Interv Radiol* **21**, 865-876 (2010).
35. S.C. Rose, S.G. Kikolski, J.E. Chomas, Downstream Hepatic Arterial Blood Pressure Changes Caused by Deployment of the Suire AntiReflux Expandable Tip. *Cardiovasc Intervent Radiol* **36**, 1262-1269 (2012).
36. A. Arepally, J. Chomas, D. Kraitchman, K. Hong, Quantification and reduction of lux during embolotherapy using an antilux catheter and tantalum microspheres: ex vivo analysis. *J Vasc Interv Radiol* **24**, 575-580 (2013).
37. B.P. Barnett, A. Arepally, P.V. Karmarkar, D. Qian, W.D. Gilson, P. Walczak, V. Howland, L. Lawler, C. Lauzon, M. Stuber, D.L. Kraitchman, J.W.M. Bulte, Magnetic resonance-guided, real-time targeted delivery and imaging of



- magnetocapsules immunoprotecting pancreatic islet cells. *Nat Med* **13**, 986-991 (2007).
38. M.A. Unger, H. Chou, T. Thorsen, A. Scherer, S.R. Quake, Monolithic Microfabricated Valves and Pumps by Multilayer Soft Lithography. *Science* **288**, 113-116 (2000).
39. C.A. Steginsky, J.M. Beale, H.G. Floss, R.M. Mayer, Structural determination of alginic acid and the effects of calcium binding as determined by high-field n.m.r. *Carbohydrate Research* **225**, 11-26 (1992).
40. H. Gu, M.H.G. Duits, F. Mugele, Droplets formation and merging in two-phase flow microfluidics. *International Journal of Molecular Sciences* **12**, 2572-2597 (2011).
41. J.D. Tice, A.D. Lyon, R.F. Ismagilov, Effects of viscosity on droplet formation and mixing in microfluidic channels. *Analytica Chimica Acta* **507**, 73-77 (2004).
42. J.D. Tice, H. Song, A.D. Lyon, R.F. Ismagilov, Formation of droplets and mixing in multiphase microfluidics at low values of the reynolds and the capillary numbers. *Langmuir* **19**, 9127-9133 (2003).
43. P. Garstecki, M.J. Fuerstman, H.A. Stone, G.M. Whitesides, Formation of droplets and bubbles in a microfluidic T-junction-scaling and mechanism of break-up. *Lab on a Chip* **6**, 437-446 (2006).
44. M. De Menech, P. Garstecki, F. Jousse, H.A. Stone, Transition from squeezing to dripping in a microfluidic T-shaped junction. *Journal of Fluid Mechanics* **595**, 141-161 (2008).

45. H. Liu, Y. Zhang, Droplet formation in a T-shaped microfluidic junction. *Journal of Applied Physics* **106**, 034906-034908 (2009).
46. G.F. Christopher, S.L. Anna, Microfluidic methods for generating continuous droplet streams. *Journal of Physics D: Applied Physics* **40**, R319 (2007).

## **Chapter 4 Piezoelectric Bioprinting of Human Mesenchymal Stem Cells, Induced-Pluripotent Stem Cells, and Ethiodized Oil in Alginate Microcapsules**

### 4.1 Introduction

In Chapter 3 we demonstrated the ability to encapsulate stem cells and imaging agents in highly uniform hydrogel microspheres using a droplet microfluidics-based platform.

However, there are limitations to the platform. Among them is its sensitivity to the aqueous solution's wetting properties. At the device nozzle where alginate is extruded and side-sheared into droplets, if the surface tension of the aqueous solution containing the hydrogel precursor changes drastically, droplets would not form. This became evident when the device nozzles became easily clogged as we introduced various biopolymers, such as fibrinogen and gelatin, to the mixture. Thus, the device is not very amenable to microcapsule production using different solutions.

Another drawback to the microfluidic platform is scalability. As discussed earlier, it is possible to increase the throughput of microcapsules production by increasing the flow rate, and also by increasing the number of nozzles on the device. The former can be achieved by increasing the applied pressure to the system to a certain degree before the excessive pressure causes the device to fail. However, the latter method isn't readily achievable. The number of nozzles on a given device is determined by the design features during the microfabrication process. As such, in order to increase the number of

nozzles, we must construct a new mold, which is time consuming. In this chapter, we explore a piezoelectric bioprinting platform that combines the high throughput of the conventional electrospraying techniques, with controllability on the scale of the microfluidics platform, with the added bonus of spatial control in three dimensions.

#### 4.1.1 Piezoelectric inkjet bioprinting

Freeform fabrication techniques such as stereolithography, fused deposition modelling and 3-dimensional inkjet printing are capable of manufacturing scaffolds for use in tissue engineering with complex internal architecture [1–3]. The incorporation of cells into these scaffolds however, still poses a significant problem. Current cell-seeding techniques, whether static or dynamic, can result in non-uniform distribution, limited penetration depth and utilize a limited variety of cell types [4,5]. Klebe [6] was the first to propose the use of micropositioning techniques to precisely locate individual cells in structures. Mironov and Boland explored this concept further and demonstrated its feasibility [7,8]. A number of research groups have now used inkjet printing as a method for the deposition of biochemical factors to make microarrays and to promote cell adhesion or direct cell growth [9–12]. Inkjet printing has also been used to selectively deposit and position living cells, with the earliest work using bacteria [13].

Inkjet printers generate and position droplets using one of two different mechanisms. In continuous inkjet printing (CIJ), a stream of fluid is passed through a small orifice and breaks up into small droplets by Rayleigh instability. If an electric charge is imparted to

the drops, they can subsequently be steered by applying an electrostatic or magnetic field. In drop-on-demand inkjet printing (DOD), the drops are only formed when required and spatial control is achieved by mechanically positioning the print-head before drop ejection. DOD can be further subdivided through distinguishing the mechanism by which a drop is ejected. With thermal DOD a heater is used to vaporize a small volume of the fluid to be printed in a chamber immediately behind the printing orifice. The resulting bubble expands rapidly and imparts the energy required to eject a drop. In piezoelectric and electrostatic DOD, the mechanical impulse is applied directly, by either a rapid change in shape of a piezoelectric crystal or by an electrostatically driven mechanical displacement adjacent to the fluid-filled chamber. CIJ operates at much faster droplet generation rates than DOD printers, however, the need to use an electrically conducting fluid and the possibility of contamination during the recirculation process are limitations for biological applications. In this study we use a piezoelectrically actuated DOD printer to dispense stem cell microcapsules with high uniformity and high throughput.

## 4.2 Materials and Methods

### 4.2.1 Cells and culture conditions

Human mesenchymal stem cells were cultured in Mesenchymal Stem Cell Growth Medium (MSCGM, Lonza). Human induced pluripotent stem cells were cultured using E8 media (Essential 8 medium, ThermoFisher Scientific). Cells were cultured using standard procedures in T75 culture flasks and incubated at 37 °C at 5% CO<sub>2</sub>. Once the cells are ready for use, they are rinsed with PBS and trypsinized (Trypsin-EDTA 0.05%, ThermoFisher Scientific) and incubated for 2-3 minutes or until at least 90% of cells have

detached from the flask and are in single cell suspension. The trypsin is then neutralized by the addition of media and transferred to a conical tube to be centrifuged at 1000 rpm for 5 mins. The supernatants are removed and the cell pellet is resuspended in a sodium alginate solution (0.75%, ProNova LVG UP, Novamatrix) at a concentration of  $\sim 3 \times 10^6$  cells/mL. The resulting solution is then loaded to a tubing as “ink” to the piezoelectric inkjet printer.

#### 4.2.2 Microcapsule printing mechanism

Printing experiments were carried out using a single-jet stationary piezoelectric printhead (Microjet MJ-AB-01, Microfab Inc.), which consists of a glass capillary bonded to an annular piezoelectric actuator (Fig. 4-2A-B). The capillary tapers to a fine orifice with a specific diameter through which droplets are ejected upon application of a suitable electrical pulse to the actuator. The printhead driving waveform is controlled through the drive electronics, Jet Drive II (Microfab Inc.), and defined using an interfaced PC. The precise shape of the electrical signal used to drive the piezoelectric actuator will influence the fluid mechanical forces during printing, and the optimal waveform will vary depending on the surface tension and acoustic properties of the fluid.

An example of an electrical pulse is shown in Figure 4-1, marked with regions of interest. During the rise time, the tubular PZT expands its circumference while becoming thinner and shorter. The fast deformation is transmitted through the epoxy bond to the glass tube and results in an outwards motion of the inner glass surface, which produces a negative pressure (with respect to the equilibrium). The negative pressure travels in the fluid at the speed of sound along the glass tube in the form of an expansion acoustic wave to both the

orifice and the supply end. The expansion wave is reflected as a compression wave (higher pressure than the equilibrium pressure in the glass tube) at the supply end and travels back towards the orifice. If the dwell time is selected to start when the positive pressure wave matches the piezoelectric actuator, the inwards motion of the inner glass surface reinforces it resulting in a faster and larger droplet.

Figure 4-2D shows the sequence of events at the orifice leading to droplet formation starting with the equilibrium condition. Fluid is flush at the orifice (first image). The fluid interface is then withdrawn from the equilibrium position at the arrival of the expansion wave at the orifice. The second image is after the compression wave reaches the orifice causing the fluid to emerge. Another expansion wave reaching the orifice causes the fluid to pull back (images three) and to break off and leave the orifice. The ejected fluid is pulled into a spherical drop by surface tension forces (image four). The images are obtained by a short pulse of light from an LED that is synchronized with the pulse generating the drop. By adjusting the delay between the actuation pulse and the pulse applied to the LED, the droplets are captured at different locations during the flight path.

#### 4.2.3 Cell viability

Cell viability is determined by Live/Dead staining or by trypan blue. Microcapsules are incubated with 2  $\mu\text{M}$  Calcein AM (Sigma Aldrich) for 20 minutes and with 5  $\mu\text{M}$  propidium iodide (Sigma Aldrich) for 5 minutes and imaged immediately.

#### 4.2.4 Imaging agent preparation

Lipiodol emulsions were made ultrasonically a mixture of equal parts lecithin (Sigma Aldrich) and lipiodol (ethiodized oil, Guerbet) while sitting on ice, as described previously. The resulting lipiodol emulsion is added to ProNova ultrapure LVG alginate (Novamatrix) to a final composition of 12% lipiodol emulsions and 1.5% alginate.

### 4.3 Results

#### 4.3.1 Physical characterization of bioprinted alginate microcapsules

Alginate microcapsules were bioprinted (Figure 4-3A and Figure 4-3B) using an 80- $\mu\text{m}$  inner diameter piezoelectric printhead ( $53.46 \pm 5.83 \mu\text{m}$ ) and a 40- $\mu\text{m}$  inner diameter piezoelectric printhead ( $32.77 \pm 4.08 \mu\text{m}$ ) with the following printing parameters: 38–40 V,  $t_{\text{rise}} = t_{\text{fall}} = 5 \mu\text{s}$ ,  $t_{\text{dwell}} = 15\text{--}20 \mu\text{s}$ ,  $t_{\text{echo}} = 30\text{--}40 \mu\text{s}$ , with an operating frequency between 100-240 Hz. This shows that print-head nozzle size is one factor that can control microcapsule morphology, and is important when considering the targeted delivery size. One worth noting is that while switching print-head sizes on the piezoelectric printer is as easy as switching a light bulb, in order to change the desired size for the microfluidic platform, a new mold would have to be made. Thus the piezoelectric printing platform offers better versatility in this regard.

To parallel the characterization performed on the microfluidics-generated microcapsules, we assessed the bioprinted microcapsule stability in normal saline, cell culture media, 10% fetal bovine serum, and 100% fetal bovine serum for 2 weeks (Figure 4-3C). No



significant change in microcapsule size and morphology was observed in any of the conditions. Likewise, bioprinted microcapsules were also incubated with fluorescently labeled lectins (36, 70, 120 and 150 kDa) to assess their permeability to molecules of corresponding sizes. Figure 4-4 shows that after a 72-hour incubation period, the microcapsules are relatively permeable to molecules  $\leq 75$  kDa, while molecules  $\geq 120$  kDa are mostly excluded. Representative images (Figure 4-4) show that 36 kDa and 70 kDa lectins are uniformly distributed inside the capsules after 72 hours, whereas 120 kDa and 150 kDa lectins are only visible on the surface of the microcapsules and have no effective penetration. These results are comparable to those of the properties of microfluidics-generated microcapsules.

#### 4.3.2 Bioprinted stem cell microcapsules

The piezoelectric bioprinter can also print microcapsules with cells. hMSCs (Figure 4-5A) and hiPSCs (Figure 4-5B) were bioprinted with a viability of about 98%. iPSCs were able to be encapsulated at a higher efficiency likely due to its smaller average size compared the hMSCs. Nozzle clogging occurred on occasion when printing hMSCs, possibly due to cell aggregate build up. Bioprinted rMSCs were encapsulated for 2 days under culture conditions, then released by capsule dissolution via 50mM sodium citrate. The extracted cells were replated for 12 hours to allow for focal adhesion and stained with calcein AM and propidium iodide. Figure 4-5D shows replated rMSCs with healthy morphology, as well as a cell with two nuclei, indicating a cell undergoing mitotic division. The replated rMSCs continued to grow at a normal rate. These findings are comparable to other research groups who are active in the field [7,8,11,14-18].

#### 4.3.3 Co-encapsulation with imaging agents

Several attempts at printing microcapsules containing PFOB were unsuccessful, thus we selected a different clinical imaging agent, lipiodol. Since lipiodol is not an aqueous solution, it was first emulsified with surfactant before mixing with the alginate for printing. Microcapsules containing 0.75% lipiodol were printed as tear-drop shaped microcapsules with a mean diameter of  $57.91 \pm 3.83 \mu\text{m}$  (Figure 4-6A). The tear-drop morphology indicates that the solution likely has a very low surface tension and could not form a stable droplet before gelation. This may be amended by altering the shape of the electrical pulse applied to the piezoelectric actuator to better balance the droplet ejection forces. Though some optimization and imaging characterization will be required, the microcapsules containing lipiodol are potentially traceable using conventional clinical scanners, and may be co-delivered in conjunction with encapsulated stem cells.

#### 4.3.4 Co-encapsulation with biopolymer

To assess the potential of incorporating biopolymers to the microcapsule matrix to enhance cellular survival and therapeutic activity, microcapsules containing 0.5% fibrinogen were successfully printed (Figure 4-6B,  $62.48 \pm 3.91 \mu\text{m}$ ). Another potential advantage to biopolymer incorporation is the ability to form secondary crosslinks. For example, in the presence of thrombin, fibrinogen is converted to fibrin, which plays important roles in cell adhesion as well as tissue repair. Incorporation of biopolymers into the capsule matrix not only provides a potential second layer of reinforcement to the encapsulation matrix, but can also be selectively and controllably degraded to modulate

the pore size of the microcapsule *in situ*. Furthermore, the alginate can be removed by subsequent citrate dissolution to obtain pure fibrin microcapsules. In this example, 1 units/mL Thrombin was added to fibrinogen-containing microcapsules and incubated to facilitate secondary crosslinking. After 24 hours, 50mM sodium citrate was added to the fibrinogen-containing microcapsules to dissolve the alginate. However, after centrifugation, we were not able to recover any fibrin microcapsules. This may be due to the fibrin concentration being too low to sustain its own rigid structure. Using a similar procedure, alginate-fibrin microfibers were made (data not shown), and the alginate component was successfully removed, leaving behind intact fibrin fibers. Nevertheless, further experimentation will be required to test the extent of these hypotheses.

#### 4.4 Conclusion

The piezoelectric bioprinter introduces a few degrees of freedom compared to the microfluidics platform. Whereas in the microfluidics setup, once the device starts flowing, it is rather difficult to change operating solutions due to the fact that crosslinking will occur at the nozzles if the solutions does not flow continuously, causing the device to fail. With the piezoelectric platform, changing “bioink” or the printhead is simple and quick. We also demonstrated the ability to control microcapsule size by changing the size of the printheads. The resulting microcapsules had similar size distribution, stability in therapeutically relevant conditions, as well as permeability properties as the microfluidics-produced microcapsules. Moreover, the piezoelectric printer platform has the ability to deposit cells at predefined positions with high spatial resolution, and thus its versatility is amenable to automated biofabrication of 2D and 3D structures for a wide

range of applications. Lastly, we demonstrated that composite microcapsules can be printed together with biopolymers, potentially enhancing cell viability and introducing a degradable parameter that may pave way to timed release of cargo by dynamically changing the microcapsule pore size.

4.5 Figures

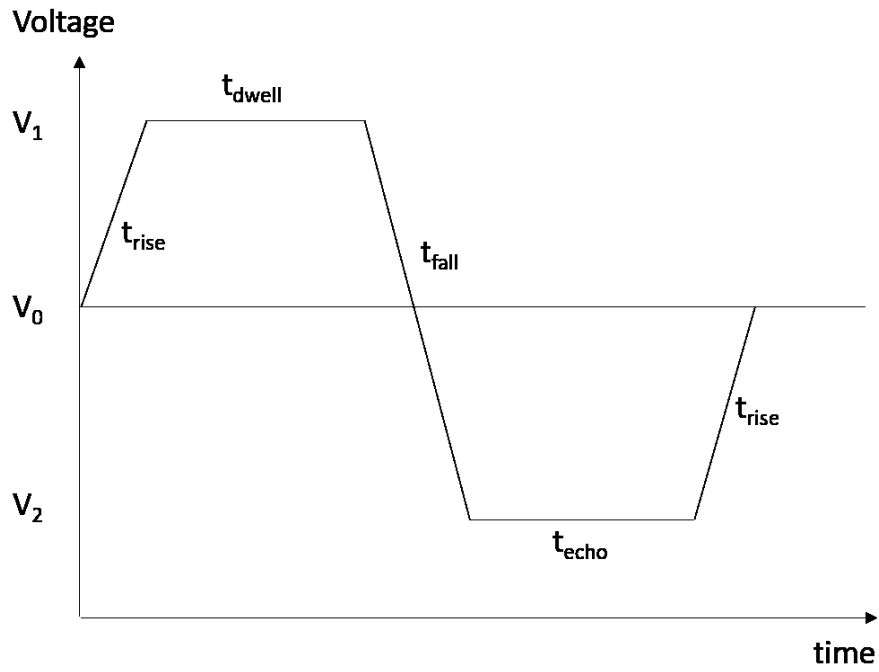


Figure 4-1: Example of an actuating voltage signal to generate a droplet.

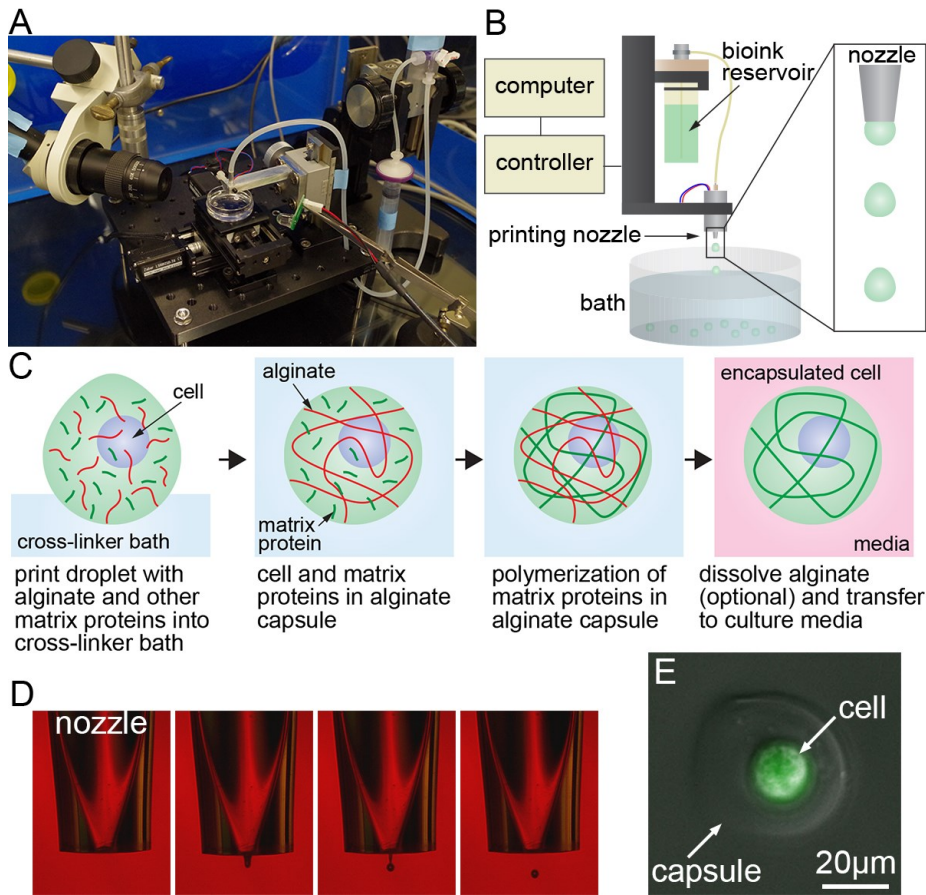


Figure 4-2: Piezoelectric bioprinter setup and schematic.

(A) Photograph of bio-printer for cell encapsulation. (B) Schematic illustration of hardware. (C) Schematic illustration of the alginate-based template method for cell encapsulation. Alginate gels rapidly on printing into a  $\text{CaCl}_2$  bath. Other matrix proteins (e.g. fibrinogen, matrigel) gel more slowly. The alginate can be dissolved in citrate solution and the capsules re-suspended in media for storage. (D) Photographs of droplet dispensing from an  $80\ \mu\text{m}$  nozzle. (E) Single hiPS cell embedded in a  $50\ \mu\text{m}$  diameter alginate/fibrin capsule.

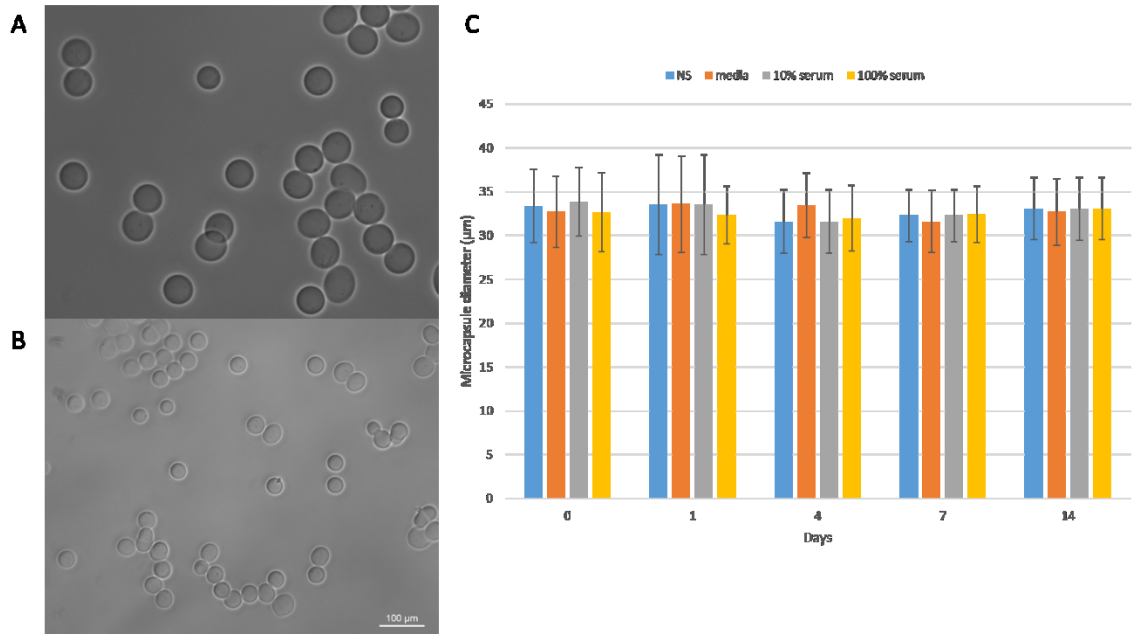


Figure 4-3: Bioprinted microcapsule size and stability.

Alginate microcapsules bioprinted using (A) 80-μm ad (B) 40-μm inner diameter piezoelectric printhead. (C) Microcapsule size stability in normal saline, media, 10% fetal bovine serum (FBS), and 100% FBS over 14 days. Scale bar = 100 μm.

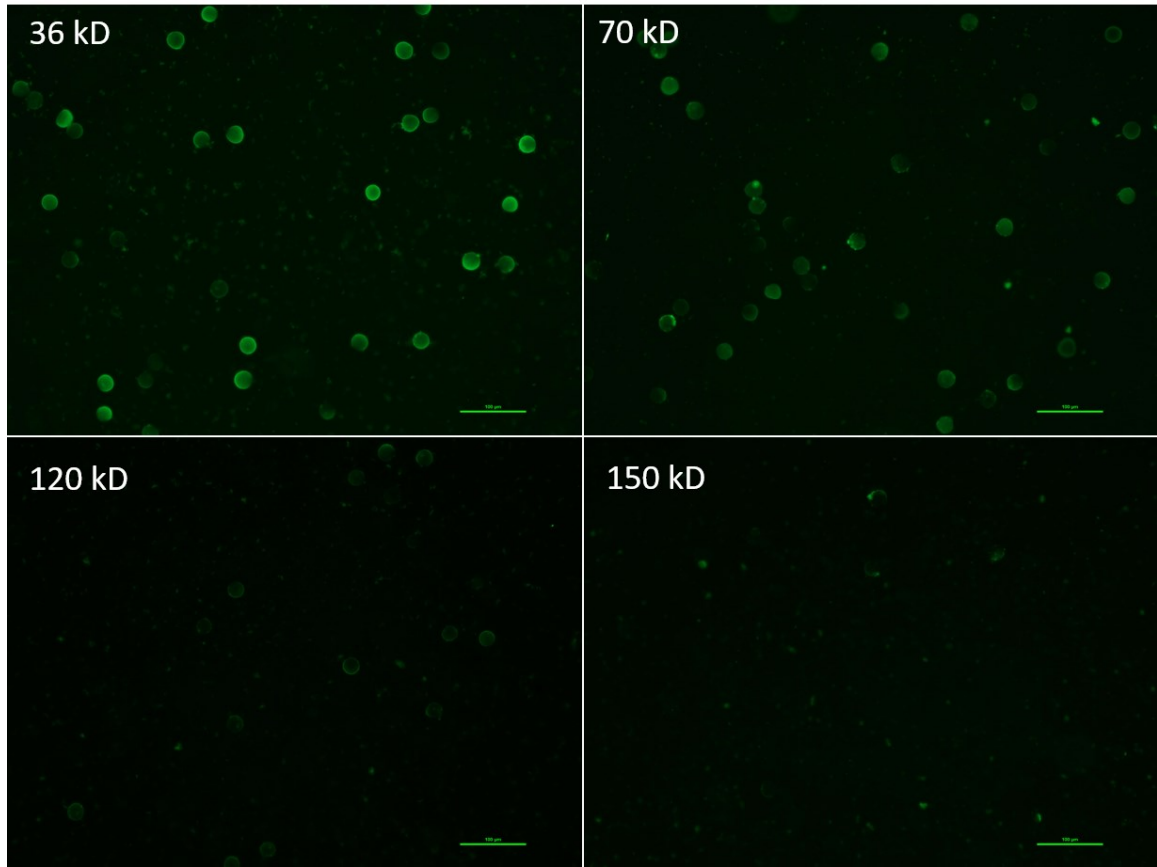


Figure 4-4: Permeability of bioprinted alginate microcapsules.

Microcapsules were incubated with fluorescent lectin of various sizes (36 kD, 70 kD, 120 kD, 150 kD) for 72 hours and imaged. Scale bar = 100  $\mu\text{m}$ .



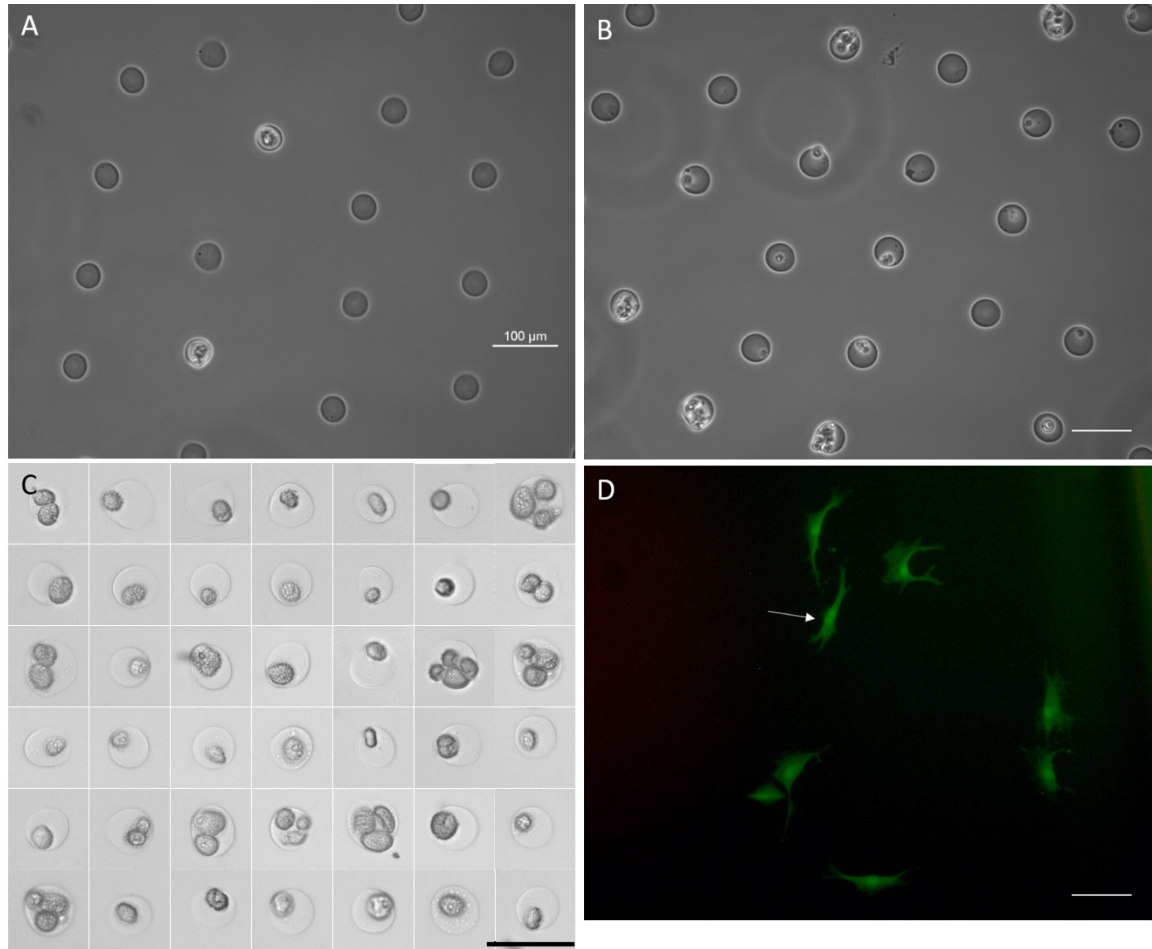


Figure 4-5: Bioprinting of MSC and iPSC.

(A) Bioprinted microcapsules containing hMSC. (B) Bioprinted microcapsules containing iPSC. (C) Representative image showing bioprinted microcapsules containing hMSCs. (D) rMSCs were encapsulated for 2 days and released by capsule dissolution and recultured for 12 hours. Green: calcein AM, Red: propidium iodine. White arrow: rMSC undergoing cell division. Scale bar = 100  $\mu\text{m}$ .

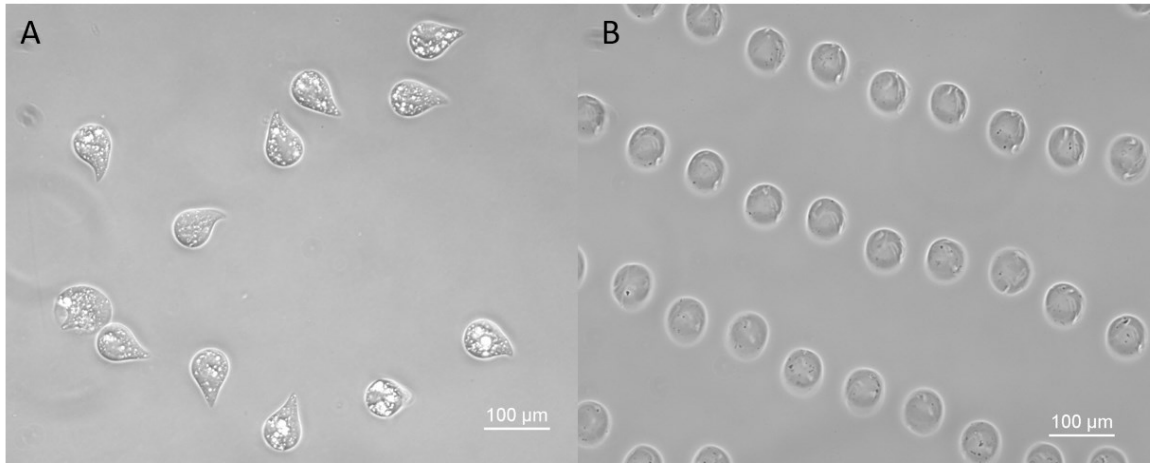


Figure 4-6: Co-encapsulation with imaging agents and fibrinogen.

Microcapsules containing (A) lipiodol emulsions and (B) fibrinogen. Scale bar = 100 µm.

#### 4.6 References

1. Leong KF, Cheah CM, Chua CK. Solid freeform fabrication of three-dimensional scaffolds for engineering replacement tissues and organs. *Biomaterials* 2003;24(13):2363–78.
2. Hutmacher DW, Sittinger M, Risbud MV. Scaffold-based tissue engineering: rationale for computer aided design and solid free-form fabrication systems. *Trends Biotech* 2004;22:354–62.
3. Sachlos E, Czernuszka JT. Making tissue engineering scaffolds work. Review on the application of solid freeform fabrication technology to the production of tissue engineering scaffolds. *Eur Cells Mater* 2003; 5(1):29–40.
4. Freed LE, Vunjak-Novakovic G. Culture of organised cell communities. *Adv Drug Delivery Rev* 1998;33:15–39.
5. Wendt D, Marsano A, Jakob M, Heberer M, Martin I. Oscillating perfusion of cell suspensions through three-dimensional scaffolds enhances cell seeding efficiency and uniformity. *Biotech Bioeng* 2003; 84:205–14.
6. Klebe RJ. A method for micropositioning cells and the construction of 3-dimensional and 3-dimensional synthetic tissues. *Exp Cell Res* 1988;179:362–73.
7. Mironov V, Boland T, Trusk T, Forgacs G, Markwald RR. Organ printing: computer-aided jet-based 3D tissue engineering. *Trends Biotech* 2003;21:157–61.
8. Wilson Jr WC, Boland T. Cell and organ printing 1: protein and cell printers. *Anat Rec A* 2003;272A:491–6.
9. Okamoto T, Suzuki T, Yamamoto N. Microarray fabrication with covalent attachment of DNA using Bubble Jet technology. *Nat Biotech* 2000;18:438–41.

10. Zaugg FG, Wagner P. Drop-on-demand printing of protein biochip arrays. *MRS Bull* 2003;28:837–42.
11. Roth EA, Xu T, Das M, Gregory C, Hickman JJ, Boland T. Inkjet printing for high throughput cell patterning. *Biomaterials* 2004;25: 3703–15.
12. Campbell PG, Miller ED, Fisher GW, Walker LM, Weiss LE. Engineered spatial patterns of FGF-2 immobilized on fibrin direct cell organization. *Biomaterials* 2005;26(33):6762–70.
13. Bruns A, Hoffelnerand H, Overmann J. A novel approach for high throughput cultivation assays and the isolation of planktonic bacteria. *FEMS Microbiol Ecol* 2003;45:161–71.
14. Xu T, Jin J, Gregory C, Hickman JJ, Boland T. Inkjet printing of viable mammalian cells. *Biomaterials* 2005;26:93–9.
15. Saunders RE, Gough JE, Derby B. Inkjet printing of mammalian primary cells for tissue engineering applications. In: Laurencin CT, Botchwey EA, editors. *Nanoscale materials science in biology and medicine*. Boston: MRS; 2005. p. 57–62.
16. Saunders RE, Bosworth L, Gough JE, Derby B, Reis N. Selective cell delivery for 3D tissue culture and engineering. *Eur Cells Mater* 2004;7(S1):84–5.
17. Nakamura M, Kobayashi A, Takagi F, Watanabe A, Hiruma Y, Ohuchi K, et al. Biocompatible inkjet printing for designed seeding of individual living cells. *Tissue Eng* 2005;11: 1658–66.

18. Boland T, Miranov V, Gutowska A, Roth EA, Markwald RR. Cell and organ printing 2: fusion of cell aggregates in three-dimensional gels. *Anatom Rec A* 2003;272A(2):497–502.

## Chapter 5 Summary and Outlook

Current development in stem cell delivery for cardiac regeneration suffers from many shortcomings. Among them are the difficulty in delivering the stem cells to the desired locations, the lack of visual information regarding the transplanted cells, and the inability to ensure that the transplanted cells are viable and can undertake the intended therapeutic mechanisms effectively. In this thesis we have proposed two innovative approaches to provide site-specific delivery of microencapsulated, immunoprotected, stem cells with imaging visible microcapsules.

First, we developed a microfluidic platform capable of producing high uniform and very small hydrogel microcapsules embedded with high sensitivity imaging agents. The reduced size of the microcapsules provides two significant advantages over conventional cell encapsulation techniques. Firstly, unlike the reduced microcapsules, conventional cell capsules are too large for the smaller sized commercially available microcatheters. Secondly, smaller microcapsules are able to penetrate smaller capillary beds, achieving cell delivery in a more controlled, site-specific manner. We have demonstrated that microcapsules embedded with barium sulfate imaging agent can be serially monitored in large animal studies and does not elicit host immune responses.

Next, we modified the microfluidics platform to allow for cellular encapsulation. We demonstrated that hMSCs can be effectively encapsulated in the reduced microcapsules

with high long term viability. Co-encapsulation with imaging agents were less viable than expected. However, co-delivery of separately encapsulated imaging agents were viable with high CT sensitivity. We also showed that encapsulated hMSCs were not functionally stunted by the encapsulation process.

Lastly, we explored a platform of encapsulating stem cells and other materials using a piezoelectric inkjet bioprinter. We demonstrated that the bioprinter platform is also capable of achieving very small and highly uniform stem cell microcapsules and imaging agent microcapsules for controlled site-specific stem cell delivery. At the same time, it offers more versatility over the microfluidics platform including higher throughput, ease of changing printheads and operating parameters to control microcapsules size and morphology, as well as being amenable to a wider range of materials as its “bioink”.

It would be interesting to further discover the potentials of the bioprinter platform. In particular, we would like to explore the idea of using sodium alginate as a sacrificial template to produce pure fibrin or collagen microcapsules. Sodium alginate has always been a biomaterial of choice for tissue engineering applications for its bioinertness. On the other hand, selective degradability can be utilized to achieve controlled or timed release of selective cargo. For example, encapsulated cells intended for direct intervention can be released after a timed delay after the hostile microenvironment has subsided, improving cell survival and retention.

Clearly, the work detailed in this thesis represent merely the tip of the iceberg of potential developments in the field of site-specific stem cell delivery for tissue regenerative applications. Further innovation and discovery in this area will revolutionize the vast field of tissue engineering in ways that will greatly benefit the scientific community and society at large.



## **Curriculum Vitae**

Tsang Chung Charles Hu  
Born February 18<sup>th</sup>, 1986 in Hong Kong SAR

### **EDUCATION**

Ph.D., Materials Science & Engineering  
Johns Hopkins University, Baltimore MD  
January, 2017

Bachelor of Science, Bioengineering  
University of California, Berkeley CA  
December 2008

### **PUBLISHED WORK**

- All AH, Bazley FA, Gupta S, Pashai N, Hu C, Pourmorteza A, Walczak P, Kerr CL. Human embryonic stem cell-derived oligodendrocyte progenitors aid in functional recovery of sensory pathways following contusive spinal cord injury. PLoS ONE 7(10): e47645, October 2012.
- Bazley FA, Hu C, Maybhate A, Pourmorteza A, Pashai N, Thakor NV, Kerr CL, All AH. Electrophysiological evaluation of sensory and motor pathways after incomplete unilateral spinal cord contusion. Journal of Neurosurgery: Spine 16(4):414-423, April 2012.
- Maybhate A, Hu C, Bazley FA, Yu Q, Thakor NV, Kerr C, All AH. Potential Long Term Benefits of Acute Hypothermia after Spinal Cord Injury: Assessments with Somatosensory Evoked Potentials. Critical Care Medicine 40(2):573-579, February 2012.
- Greenwald E, Mollazadeh M, Hu C, Tang W, Culurciello E, Thakor NV. A VLSI Neural Monitoring System with Ultra-Wideband Telemetry for Awake Behaving Subjects. IEEE Transactions on Biomedical Circuits and Systems 5(2):112-119, April 2011.

### **CONFERENCES**

- Fu Y, Hu C, Weiss C, Mao HQ, Georgiades C, Kraitchman DL. Hydrogel-based X-ray-visible Microspheres Development for Bariatric Arterial Embolization to Treat Obesity. American Heart Association Scientific Session 2016. New Orleans, LO.

- Akinwande O, Hu C, et al. Recanalization/collateralization after bariatric embolization in a swine model: Comparison between 40 $\mu$ m, 100-300 $\mu$ m and 300-500 $\mu$ m Embolic Microspheres. Society for Interventional Radiology Annual Scientific Meeting 2016. Vancouver, BC.
- Hu C, Beh C, Wang J, Mao HQ, Kraitchman DL. Microfluidic Synthesis of Small, Uniform Microcapsules Containing Human Mesenchymal Stem Cells And Perfluorocarbon Imaging Agent for Therapeutic Intracardiac Delivery. Tech Council of Maryland's Annual Bio-Tech Conference 2016. Bethesda, MD.
- Kraitchman DL, Hu C, Anders R, Moran T, Singh J, DiCamillo P, Shin E, Mao HQ, Wang TH, Aravind A, Weiss C. Bariatric Arterial Embolization as Treatment for Obesity: Mechanisms Using Highly Calibrated 50 Micron Embolic Beads. American College of Cardiology 2015. San Diego, CA.
- Weiss CR, Holly B, Arepally A, Singh J, Paudel K, Hu C, Mao HQ, Wang TH, Kraitchman DL. Recanalization after Bariatric Embolization in a Swine Model: Potential Implications for Future Bariatric Surgery. Society of Interventional Radiology Annual Scientific Meeting 2015. Atlanta, GA.
- Weiss CR, Paudel K, Hu C, Arepally A, Singh J, Beh CW, Wang Th, Mao HQ, Shin EJ, Anders R, Moran T, Kraitchman DL. Effects of Bariatric Embolization on Weight Gain, Selected Appetite-Driving Hormones of Obesity and Gastric Histology. Obesity Week 2014. Boston, MA.
- Weiss CR, Arepally A, Moran T, Hu C, Singh J, Mao HQ, Wang TH, Kraitchman DL. CIRSE 2014. Glasgow, UK. Effect of Bariatric Embolization on Various Appetite-Driving Hormones of Obesity. Cardiovascular and Interventional Radiological Society Annual Meeting 2014. Glasgow, UK.
- Weiss CR, Hu C, Arepally A, Singh J, Beh CW, Wang JT, Mao HQ, Shin EJ, Moran TH, Kraitchman DL. Bariatric Embolization Using Imaging Visible Embolic Beads, An Anti-Reflux Microcatheter, and Cone-Beam CT: Short-Term Outcomes in a Swine Model. Society of Interventional Radiology Annual Scientific Meeting 2014. San Diego, CA.
- Hu C, Beh CW, Karmarkar P, Johnston PV, Wang TH, Mao HQ, Kraitchman DL. X-Ray-Visible Transmyocardial Catheter-Based Microencapsulated Mesenchymal Stem Cell Delivery for Cardiac Regenerative Therapy. Hopkins Imaging Conference 2013. Baltimore, MD.
- Hu C, Beh CW, Karmarkar P, Johnston PV, Wang TH, Mao HQ, Kraitchman DL. X-Ray-Visible Transmyocardial Catheter-Based Microencapsulated Mesenchymal Stem Cell Delivery for Cardiac Regenerative Therapy. American Heart Association Scientific Session 2013. Dallas, TX.

- Hu C, Beh CW, Park J, Weiss CR, Kraitchman DL, Wang TH, Mao HQ. Imaging-Visible Microencapsulation of Human Mesenchymal Stem Cells using Droplet Microfluidics for Microcatheter-Based Site-Specific Cell Delivery. Biomedical Engineering Society Annual Meeting 2013. Seattle, WA.
- Hu C, Beh CW, Hegde SS, Park J, Weiss CR, Johnston PV, Wang TH, Mao HQ, Kraitchman DL. Microencapsulation of Single Stem Cells for Ischemic Heart Treatment. American College of Cardiology Scientific Session 2013. San Francisco, CA.
- DiCamillo PA, Kraitchman DL, Hu C, Beh W, Mao H, Wang T, et al. Bariatric Arterial Embolization: Histopathological Confirmation of Precise Gastric Fundus Targeting. Radiological Society of North America Annual Meeting 2012.
- Kraitchman D, Weiss CR, Beh CW, Hu C, DiCamillo P, Cook J, Gabrielson KL, Wang T, Mao H. In vivo Biocompatibility and Efficacy of an X-ray-visible, Uniform, Alginate Microsphere for Embolic Therapy. World Molecular Imaging Congress 2012.
- Hu C, Maybhate A, Bazley F, Gupta S, Han Y, Pashai N, Pourmorteza A, Zhou L, Kerr CL, All AH. Neurophysiological Monitoring and In Vivo Imaging for Studying Stem Cell-Mediated Therapeutic Strategies for Spinal Cord Injury. Stem Cell World Congress 2011.
- Kerr CL, Maybhate A, Hu C, Letzen B, Zheng J, Gearhart J, Thakor N, All AH. MicroRNA Profiling of Oligodendrocyte Differentiation from Human ESCs and Validation in a Rat Model of Spinal Contusion. Maryland Stem Cell Research Symposium 2010.
- Bu J, Hu C, Mohan U, All AH. Spinal Cord Injury Models and Assessments. Johns Hopkins Summer Research Symposium 2010.

## **SKILLS AND TRAINING**

Drug & gene delivery, stem cell therapy, tissue engineering and regenerative medicine, nanoparticle synthesis, materials characterization (T/SEM/Instron/AFM/spectroscopy), 3D bioprinting, microfabrication and photolithography, droplet microfluidics, microencapsulation, angiogenesis, rodent survival surgery, electrophysiology of the central nervous system, spinal cord injury, *in vivo* imaging (BLI, DTI/MRI, CT), interventional radiology, fluorescence microscopy, immunochemistry, histopathology, human stem cell and iPSC culture, transfection, flow cytometry, PCR and gene sequencing, biomechanics.

## PRIOR RESEARCH EXPERIENCES

Department of Materials Science & Engineering, Johns Hopkins University, Baltimore, MD

Rotational Graduate Student, August 2011 – January 2012

Co-advised by Dr. Hai-Quan Mao & Dr. Margarita Herrera-Alonso

- Developed novel gold nanoparticle-templated nanoparticles for siRNA delivery.
- Developed protocol for the self-assembly of polycation/DNA nanoparticles via flash nanoprecipitation for drug and gene delivery applications.
- Conducted GFP gene silencing experiments on multiple cell types and analyzed by flow cytometry.

Department of Chemical and Biomolecular Engineering, Hong Kong University of Science and Technology, Hong Kong

Dr. Ying Chau Lab, Research Assistant, May – August 2011

- Formulated and characterized Hyaluronic Acid-based hydrogels for *in vivo* imaging of the rabbit eye.

Department of Biomedical Engineering, Johns Hopkins University, Baltimore, MD

Dr. Angelo H. All Lab, Research Technologist, September 2009 – April 2011

- Managed and conducted multidisciplinary research projects involving the functional and electrical recovery of the spinal cord after contusive spinal cord injury with various therapeutic strategies including stem cell-assisted recovery and acute hypothermia treatment.
- Rodent spinal cord laminectomy and contusion, cranial electrode implantation.
- Electrophysiology of the central nervous system: Somatosensory and motor evoked potentials.
- Stem cell culture: differentiation of human embryonic stem cells (hESCs) and induced pluripotent stem cells (iPSCs) along the oligodendrocyte lineage, and the transplantation into the rat spinal cord.
- *In vivo* imaging, including Diffusion-Tensor MRI (DTI), bioluminescence imaging (BLI).
- *Ex vivo* imaging, including intracardiac perfusion and immunohistology.

- Behavioral testing.
- Developed surgical methods for novel wireless neural monitoring system for active animals.

Department of Orthopedics and Traumatology, City University of Hong Kong, Hong Kong

Dr. Kai-Ming Chan Lab, Research Assistant, February – April 2009

- Conducted experiments evaluating the efficiency of stem cell-assisted ACL reconstruction in rabbits, ultrasound-enhanced bone fracture healing and angiogenesis after tendinopathy in rats.

Department of Integrative Biology, University of California, Berkeley, Berkeley, CA

Dr. Robert J. Full Lab, Undergraduate Research Assistant, January – December 2008

- Designed and engineered novel experiments analyzing iguana kinematics and gecko gliding mechanics using force platforms, vertical wind tunnels, and high speed cameras.
- Produced results presented at SICB conference in 2009.
- Developed experimental setups still used extensively today.